NIST Technical Note 2083
Revision 1

The Thermal Character of a 1 m Methanol Pool Fire

Kunhyuk Sung
Jian Chen
Matthew Bundy
Marco Fernandez
Anthony Hamins

This publication is available free of charge from:
https://doi.org/10.6028/NIST.TN.2083r1

National Institute of Standards and Technology
U.S. Department of Commerce

NIST Technical Note 2083
Revision 1

The Thermal Character of a 1 m Methanol Pool Fire

Kunhyuk Sung
Jian Chen
Matthew Bundy
Marco Fernandez
Anthony Hamins
Fire Research Division
Engineering Laboratory

This publication is available free of charge from:
https://doi.org/10.6028/NIST.TN.2083r1

June 2021

U.S. Department of Commerce
Gina M. Raimondo, Secretary

National Institute of Standards and Technology
James K. Olthoff, Performing the Non-Exclusive Functions and Duties of the Under Secretary of Commerce for Standards and Technology & Director, National Institute of Standards and Technology

Certain commercial entities, equipment, or materials may be identified in this document in order to describe an experimental procedure or concept adequately. Such identification is not intended to imply recommendation or endorsement by the National Institute of Standards and Technology, nor is it intended to imply that the entities, materials, or equipment are necessarily the best available for the purpose.

National Institute of Standards and Technology Technical Note 2083 Revision 1
Natl. Inst. Stand. Technol. Tech. Note 2083 Rev. 1, 109 pages (June 2021)
CODEN: NTNOEF

This publication is available free of charge from:
https://doi.org/10.6028/NIST.TN.2083r1

Abstract

A series of measurements was conducted to characterize the structure of a 1 m diameter methanol pool fire steadily burning with a constant lip height in a well-ventilated quiescent environment. Time-averaged local measurements of gas-phase temperature were conducted using 50 μm diameter, Type S, bare wire, thermocouples with a bead that was approximately spherical with a diameter of about 150 μm. The thermocouple bead temperature was corrected for radiative loss and thermal inertia effects. The contribution of the radiative loss correction and thermal inertia correction terms to uncertainty of the gas velocity was analyzed. A simulation of the 1 m methanol pool fire was conducted using the Fire Dynamics Simulator (FDS) to obtain the gas velocity distribution above the burner which helped correct the thermocouple temperature measurement to obtain the gas temperature. The gas temperature distribution profile above the burner centerline was compared to previous studies of a 30 cm methanol fire. The maximum mean gas temperature was 1371 K, which occurred 30 cm above the burner on the centerline. Careful analysis determined that the average combined uncertainty of the mean and the standard deviation of the measured gas temperature was 5 % and 26 %, respectively. The actual heat release rate was measured using oxygen consumption calorimetry and compared favorably with the ideal heat release rate calculated from the measured mass burning rate. The heat flux distribution about the pool fire was measured using fourteen wide-angle view, water-cooled, Gardon-type, total heat flux gauges. The radiative emission from the fire was estimated by considering the radiative heat flux through a virtual cylinder about the fire and by a single point estimate. The radiative emission measurements coupled with the mass loss measurement allowed determination of the radiative fraction, which was equal to 0.22 ± 16 % and 0.20 ± 34 % for the multi-location and single-location measurements, respectively. Flame characteristics, such as, the mean flame height, pulsation frequency and the flame instability near the fuel surface, were analyzed using the 30 Hz video record of the fire. The mean flame height was measured as 1.10 m ± 0.22 m above the burner rim and the puffing frequency was about 1.37 Hz, which was consistent with a Fourier analysis of the transient thermocouple measurements (=1.39 Hz ± 0.013 Hz). The pool surface temperature was measured to be nearly the fuel boiling point.

KEYWORDS: heat release rate; temperature distribution; burning rate; heat flux distribution; pool fires

Preface to the Second Edition

The first edition of this report (NIST Technical Note 2083), was published in February 2020. The objective of the second edition is to improve documentation of the temperature measurement uncertainty analysis, including a focus on the analysis of the uncertainties of the 1) local instantaneous gas temperature, 2) the local mean gas temperature, and 3) the standard deviation of the local gas temperature measurements. Section 3.7 and Appendices C, D, E.1, and H have been added to the report to improve the accuracy and reporting of the gas temperature measurements and its uncertainty.

Section 3.7 analyzes the contributions of the radiative loss and thermal inertia correction terms to the mean and standard deviation of the gas temperature. The results show that the thermal inertia correction term has a negligible influence on the mean gas temperature, but does amplify the value of the instantaneous temperature extremes.

Appendix E.1.1 analyzes the contributions of the radiative loss and thermal inertia correction terms to the uncertainties of the both the mean and standard deviation of the gas temperature measurements. Appendix E.1.2 presents the uncertainties of both the mean and standard deviation of the gas temperature measurements.

A simulation of the 1 m methanol pool fire was conducted using the Fire Dynamics Simulator (FDS) Version 6.7.5 to obtain the gas velocity distribution above the burner and to validate an in-house MATLAB code, which was developed to solve the energy balance at the thermocouple bead. The corrected gas temperature was recalculated using the simulated gas velocity distribution above the burner (the gas velocity is assumed to equal 2 m/s everywhere in the first edition of this report). Appendix C provides numerical details and results of the simulated gas velocity, the simulated gas temperature and the simulated radiative fraction.

Appendix D presents verification and validation of the in-house MATLAB code. The code is verified using a sinusoidal function as input, and validated using the FDS simulation results. Appendix D.2 describes a parametric study conducted to optimize the fitting method to calculate the time derivative of the bead temperature (used to analyze the energy balance at the thermocouple bead). In *Appendix D.3*, the FDS simulated bead temperature is corrected using the MATLAB code. Compared with the FDS simulated gas temperature, the mean deviation of the corrected gas temperature is considered as the uncertainty in the determination of the time derivative of the bead temperature contributed to the uncertainty of the thermal inertia correction term described in *Appendix E.1*. Appendix H reproduces the input file used in the FDS simulation.

Table of Contents

This publication is available free of charge from: https://doi.org/10.6028/NIST.TN.2083r1

List of Tables

This publication is available free of charge from: https://doi.org/10.6028/NIST.TN.2083r1

This publication is available free of charge from: https://doi.org/10.6028/NIST.TN.2083r1

List of Figures

This publication is available free of charge from: https://doi.org/10.6028/NIST.TN.2083r1

1 Introduction

The focus of this study is to characterize the burning of a 1 m diameter pool fire steadily burning in a well-ventilated quiescent environment. Pool fires are a fundamental type of combustion phenomena in which the fuel surface is flat and horizontal, which provides a simple and well-defined configuration to test models and further the understanding of fire phenomena. In this study, methanol is selected as the fuel. Fires established using methanol are unusual as no carbonaceous soot is present or emitted. This creates a particularly useful tested for fire models and their radiation sub-models that consider emission by gaseous species — without the confounding effects of blackbody radiation from soot.

Many studies have reported on the structure and characteristics of 30 cm diameter methanol pool fires, including the total mass loss rate [1-3], mean velocity [4], pulsation frequency [4] and gas-phase temperature field [4, 5]. With so many measurements characterizing the 30 cm methanol pool fire, it is a suitable candidate for fire modeling validation studies [3, 6-8].

On the other hand, research on the detailed structure and dynamics of larger pool fires is limited. Tieszen, et. al. [9, 10] used particle imaging velocimetry to measure the mean velocity field in a series of 1 MW to 3 MW methane and hydrogen pool fires burning in a 1 m diameter burner. Klassen and Gore [11] reported on flame height and the heat flux distribution near 1.0 m diameter pool fires burning a number of fuels including methanol. They used the same burner as this study, but with a 5 mm (rather than 10 mm as used here) lip height.

This study complements Ref. [11] by also measuring the local flame temperature throughout the flow field, the heat release rate using oxygen consumption calorimetry, and the radiative fraction determined by a single location measurement.

Use of fire modeling in fire protection engineering has increased dramatically during the last decade due to the development of practical computational fluid dynamics fire models and the decreased cost of computational power. Today, fire protection engineers use models like the Consolidated Fire and Smoke Transport Model (CFAST) and the Fire Dynamics Simulator (FDS) to design safer buildings, power plants, aircraft, trains, and marine vessels to name just a few types of applications [6, 12].

To be reliable, the models require validation, which involves a large collection of experimental measurements. An objective of this report is to provide data for use in fire model evaluation by the fire research community. This report is broken into several parts. In Section 2, the experimental method and apparatus are described. The results are summarized in Section 3, including local measurements of the gas temperature distribution, the heat flux distribution to the surroundings, the fuel temperature distribution, and global measurements of the heat release rate, burning rate and radiative fraction. A series of appendices provides additional information. Appendix A provides information on the thermophysical properties of methanol as well as the temperature-dependent thermal properties of air and platinum used in the temperature measurement thermal inertia and radiative loss correction. Appendix B lists the heat flux gauge calibration factors. Appendix C provides the details of the FDS simulation conducted to obtain the gas velocity distribution as well as to validate an in-house MATLAB code for the temperature correction. Appendix D describes the verification of the MATLAB code. Appendix E describes details of the uncertainty analysis for the gas temperature, heat flux, and radiative fraction determination. Appendix F presents the uncertainty in the liquid fuel temperature measurements.

2 Experimental Method

Steady-state burning conditions were established before measurements were initiated. A warm-up period of 10 min was required for the mass burning rate to be steady. Since back diffusion of water slowly accumulates in the fuel pool in methanol fires, fresh fuel was used between experiments. The purity of the methanol was 99.99 % by mass and the density was 792.7 kg/m^3 at 20 °C, according to a report of analysis provided by the supplier. Figure 1 shows the schematic of the experimental set-up. Experiments were conducted below a 6 m by 6 m canopy hood located 4 m above the burner. The effect of ambient convective currents on the fire was minimized by closing all inlet vents in the lab. The exhaust consisted of a large round duct (1.5 m diameter) located 6.0 m above the floor [13]. The smallest exhaust flow possible (about 1 kg/s) was used, helping to avoid perturbations (such as flame lean) and minimizing the influence of the exhaust on fire behavior. This led to the establishment of an unusually symmetric and recurring fire. The experiments were repeated three times.

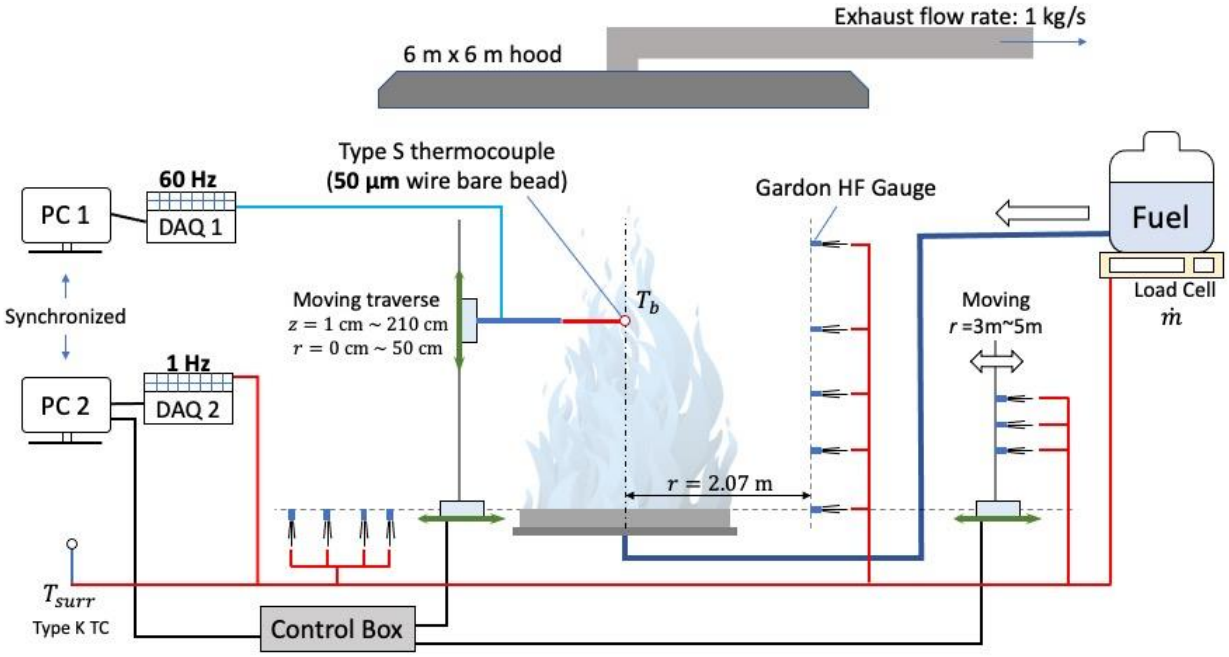

Figure 1. Schematic of the experimental set-up.

A circular pan with an inner diameter (D) of 100.6 cm ± 0.2 cm, a depth of 15 cm, and a wall thickness of 0.16 cm held the liquid methanol. An image of the burner is seen in Figure 2. The bottom of the burner was water-cooled. The burner was mounted on cinder blocks such that the burner was about 0.3 m above the floor. A fuel overflow basin included for safety extended 3 cm beyond the burner wall at its base. The fuel inlet was insulated and covered with a reflective foil to prevent preheating the fuel.

This publication is available free of charge from: https://doi.org/10.6028/NIST.TN.2083r1

Figure 2. The round, 1 m diameter, water-cooled, steel burner with fuel level indicator and fuel overflow.

Fuel to the burner was gravity fed from a reservoir on a mass load cell raised 2 m above the floor. The mass burning rate was measured by monitoring the mass loss in the 20 L methanol reservoir feeding the liquid pool, using a calibrated load cell. During the experiments, the level of the fuel was maintained 1 cm below the burner rim by regulating the fuel supply from the reservoir to the burner. The level was verified throughout the experiment by visually observing a video feed of the tiny tip of a sharpened (2 mm diameter) pointer that formed a barely discernable dimple on the fuel surface. The fuel level indicator is seen towards the left of the burner in Figure 2. A camera with optical zoom focused on the fuel level at the pointer, allowing observation of the fuel level. The standard uncertainty in the level was typically 3 mm.

2.1 Thermocouple Temperature Measurements

The local temperature was measured using a Type S (Pt 10 % Rh/Pt), bare-wire, 50 µm fine diameter thermocouple. The selection of the diameter of a fine wire thermocouple must consider trade-offs between the durability of the instrument and measurement needs. The finer the wire, the smaller the radiative exchange with the environment and the faster the measurement time response, but the more fragile the thermocouple. The thermocouple bead was approximately spherical as determined using an optical microscope. Figure 3 shows an image of the thermocouple bead, which was approximately spherical with an eccentricity of about 0.97. The bead diameter was approximately three times the wire diameter, or about 153.3 µm.

A translation device was used to adjust the position of the thermocouple along a vertical axis aligned with the pool centerline. The vertical rail was aligned with the centerline of the burner and the S-type thermocouple was attached to the tip of a horizontal rod connected to the moving rail. The connection between the thermocouple and the rod was insulated and covered with aluminum foil to prevent heat-up. The vertical rail was mounted on the horizontal translation devise to adjust the position of the thermocouple in the radial direction. Thermocouples were located every 10 cm from -10 cm to 50 cm in the radial direction and every 5 cm to 10 cm in the axial direction from 5 cm to 210 cm above the burner.

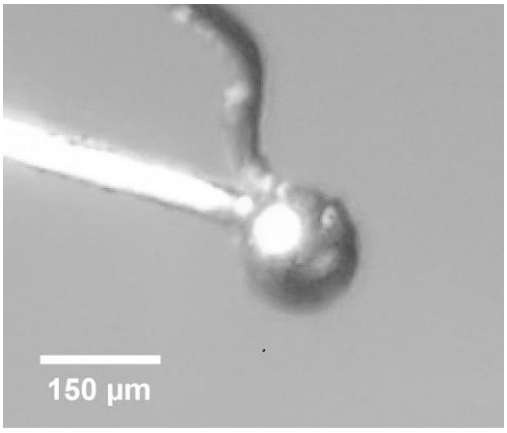

Figure 3. Image of thermocouple bead; units [µm].

The total number of measurement positions was 46. The measured signal was acquired at a rate of 60 Hz for 120 s at each position, which represents 720 measurements and about 170 flame puffing cycles. The temperature was typically measured three times at each location and always at least two times at each location.

2.1.1 Gas Temperature Determination

Table 1 summarizes the organization of the temperature measurement analysis in this report. The Table includes a full list of relevant parameters, results, and corresponding report sections. In this study, several datasets of the measured thermocouple temperature time series were acquired for 120 s at 60 Hz at each location. The mean and standard deviation of each of the temperature datasets at a particular fire position are represented by $\overline{T}_i$ and σ_{T_i}, respectively, where i is the value of the i^{th} repeated measurement. Considering each of the repeat measurements, the mean and pooled standard deviation values of the temperature are represented by $\overline{T}$ and σ_T, respectively, written as:

$$\begin{aligned} \overline{T} &= \text{Mean}\left(\overline{T}_1, \cdots, \overline{T}_i, \cdots, \overline{T}_N\right) \\ \sigma_T &= \text{RMS}\left(\sigma_{T_1}, \cdots, \sigma_{T_i}, \cdots, \sigma_{T_N}\right) \end{aligned} \tag{1}$$

where i is the i^{th} repeated measurement at a particular measurement position and N is the total number of repeat measurements. The bar above the symbol and σ represent the mean and standard deviation values, respectively. The pooled standard deviation for measurements in each dataset (which were equal in number) is equal to the Root-Mean-Square (RMS) value of the parameter (x) defined below:

$$\text{RMS}(x) = \sqrt{\frac{1}{N}\sum_{i=1}^{N} x_i^2} \tag{2}$$

The energy balance at the thermocouple bead is estimated considering the convective and radiative heat transfer. The conductive heat transfer between the thermocouple bead and the lead wire is negligible

This publication is available free of charge from: https://doi.org/10.6028/NIST.TN.2083r1

based on a heat transfer analysis of the lead wire presented in *Appendix G*. Finally, the corrected gas temperature consists of the measured bead temperature and two corrections terms including the radiative loss correction (T_{rad}) and the thermal inertia correction (T_{the}). The details of the analysis of the energy balance on the thermocouple bead and the relevant equations are described in *Section 2.1.2*.

An in-house MATLAB code was developed to calculate the corrected gas temperature considering the radiative loss and thermal inertia (T_{the}) correction terms based on an energy balance at the thermocouple bead. For the term T_{the}, the time derivative of the bead temperature ($dT_b(t)/dt$) is calculated using a second order polynomial fit of three consecutive data points in the temperature time series. The temperature-dependent thermophysical properties of air and the thermocouple material are considered and the equations describing the energy balance are solved as described in *Appendix A*. The Fire Dynamics Simulator (FDS) [6] is used to simulate the gas velocity (V_g) for each measurement position, allowing estimation of the average local Reynolds number, which plays a role in the convective term used in the energy balance at the thermocouple bead.

The MATLAB code is verified using a sinusoidal function and then validated using FDS simulation results as described in *Appendix D*. Appendix C provides the numerical details and the FDS simulation results, including the local gas temperature and velocity, which are compared with the experimental measurements. An optimized fitting method for $dT_b(t)/dt$ is determined through a parameter study presented in *Appendix D.2*. Here, the effect of the fitting method on the calculation accuracy is estimated by a dimension less parameter (γ_t) involving the data sampling frequency and the window fit size. Uncertainty associated with the fitting method is estimated in *Appendix D.3*, considering uncertainty of the corrected gas temperature (which is discussed in *Appendix E.1*).

Appendix E.1 presents the uncertainty of the instantaneous gas temperature as well as its mean and standard deviation based on a propagation of error analysis following Ref. [14]. The temperature-dependent thermophysical physical properties of air and the thermocouple material (assumed to be purely platinum) are considered, and the uncertainties of the thermophysical properties are estimated based on the uncertainties of the instantaneous temperatures. The uncertainty of dT_b/dt is discussed in *Appendix D.3* and the uncertainty of the gas velocity is estimated based on the results in Ref. [6].

In *Section 3.7*, the relative contributions of the radiative loss and thermal inertia corrections to the corrected instantaneous gas temperature are compared at a representative location as an example. The mean and standard deviation of the corrected gas temperature above the burner are estimated and compared with analogous measurement results in a 30 cm methanol pool fire. In *Appendix E.1.1*, the uncertainty results at a representative measurement location are presented for every temperature data point in the time series at a representative measurement location. The contributions of the uncertainty of the bead temperature ($u_c(T_b)$), radiative loss correction term ($u_c(T_{rad})$) and thermal inertia correction term ($u_c(T_{the})$) to the uncertainty in the instantaneous gas temperature ($u_c(T_g)$) are presented.

Section 3.7 and Appendix E.1.1 discuss the thermal inertia correction term, which is found to be of negligible importance in the determination of the mean gas temperature, but is important in the determination of its standard deviation. For this reason, the uncertainties of the mean and the standard deviation of the gas temperature are separately discussed in *Appendix E.1.2*.

Table 1. Summary of the organization of the temperature measurement analysis.

Parameter	Section Discussed	Data
T_g	Sections 2.1 & 3.7, Appendix E.1.1	Figs. 16 & E1
T_b	Sections 2.1 & 3.7, Appendix E.1.1	Figs. 16 & E1
T_r	Section 3.7	Figure 16
T_{rad}	Sections 2.1 & 3.7	-
T_{the}	Sections 2.1 & 3.7	-
$\overline{T}_g$	Sections 2.1.1 & 3.7	Figs. 19 & 21, Tables E6 & E1
$\overline{T}_b$	Sections 2.1.1 & 3.7, Appendices E.1.2 & E.1.2.3	Table E6
$\overline{T}_{rad}$	Appendix E.1	Table E1
$\overline{T}_{the}$	Appendix E.1	Table E1
σ_{T_g}	Appendix E.1.2.2	Table E6
σ_{T_b}	Sections 2.1.1 & 3.7, Appendix E.1.2.3	Table E6
$\sigma_{T_{rad}}$	Appendix E.1	Table E1
$\sigma_{T_{the}}$	Appendix E.1	Table E1
$u_c(T_g)$	Appendix E.1.1	-
$u_c(T_b)$	Appendix E.1.1	-
$u_c(T_{rad})$	Appendix E.1.1	-
$u_c(T_{the})$	Appendix E.1.1	-
$u_c(\overline{T}_g)$ & $U_c(\overline{T}_g)$	Appendix E.1.2.1	Table E6
$u_c(\sigma_{T_g})$ & $U_c(\sigma_{T_g})$	Appendix E.1.2.2	Table E6
$u_c(dT_b/dt)$	Appendix E.1.1	Table E2
$\overline{V}_g$	Appendix C.2	Figs. C2 & C3, Table C1
σ_{V_g}	Appendix E.1.1	Table E2
$u_c(V_g)$	Appendix E.1.1	Table E2
$u_c(d_b)$	Appendix E.1.1	Table E2

Variables

T_b Thermocouple bead temperature [K]
T_g Corrected gas temperature [K]
T_r Temperature corrected for radiative loss (but not the thermal inertia) [K]
T_{rad} Radiative loss correction term [K]
T_{the} Thermal inertia correction term [K]
V_g Gas velocity [m/s]
d_b Diameter of the thermocouple bead [μm]

The bar above the symbol and σ represent the mean and standard deviation values of that parameter, respectively. $u_c(x)$ is the combined uncertainty of the parameter (x) and $U_c(x)$ is the expanded combined uncertainty of the parameter, representing a 95 % confidence interval.

2.1.2 Gas Temperature Determination: Energy Balance at the Thermocouple Bead

The energy balance on the thermocouple bead consists of convective, radiative and conductive heat transfer. Here, the conductive heat transfer between the spherical bead and the lead wire is assumed to be negligible as described in *Appendix G*. The energy balance on the bead considering convective and radiative heat transfer can be expressed as:

$$\dot{Q}_{conv}(t) + \dot{Q}_{rad}(t) = \rho_b c_{p,b} V_b \frac{T_b(t)}{dt} \tag{3}$$

where ρ_b, $c_{p,b}$ and V_b are the density, specific heat and volume of the bead, respectively. $\dot{Q}$ is the net rate of heat transfer, and $\dot{Q}_{conv}$ and $\dot{Q}_{rad}$ are defined as:

$$\begin{aligned} \dot{Q}_{conv}(t) &= h\left(T_g(t) - T_b(t)\right) \\ \dot{Q}_{rad}(t) &= \epsilon\sigma\left(T_b^4(t) - T_{surr}^4\right) \end{aligned} \tag{4}$$

where $T_b(t)$ and $T_g(t)$ are the instantaneous bead temperature and gas temperature, respectively. h is the convective heat transfer coefficient of the gas flow near the bead, σ is the Stefan-Boltzmann constant ($5.67 \cdot 10^{-8}$ W/m^2/K^4), ϵ is the thermocouple emissivity, and T_{surr} is the effective temperature of the surroundings. Substituting Eq. 4 to Eq. 3, the gas temperature can be rewritten as:

$$T_g(t) = T_b(t) + \tau \frac{dT_b(t)}{dt} + \frac{\epsilon\sigma}{h}\left(T_b^4(t) - T_{surr}^4\right) \tag{5}$$

In Eq. 5, the second and third terms on the right side represent the thermal inertia and radiative loss corrections, respectively. Here, the flame is taken as essentially optically thin based on estimates using the updated RADCAL software [15], which is radiation subroutine in Ref. [6]. The average ambient temperature during the experiment was 298 K ± 5 K, which is taken as the surrounding temperature, T_{surr}, in Eq. 5. The time derivative of the bead temperature $(dT_b(t)/dt)$ was calculated using a second order polynomial fit of three consecutive data points of the temperature time series. In *Appendix D.2*, a parameter study is conducted to determine the best fitting method to calculate $T_g(t)$ using Eq. 5. When measuring high-frequency temperature fluctuations, thermal inertia of the thermocouple causes a delay between the measured bead temperature and the actual gas temperature. As the response time of the thermocouple is larger than the fire fluctuation frequency, then the thermocouple's thermal inertia can impact the variance, although there is little influence on the mean [4]. This temporal lag is characterized by the thermocouple time constant, τ, defined as:

$$\tau = \frac{m_b c_{p,b}}{h A_b} \tag{6}$$

where A_b is the surface area of the thermocouple bead. The time constant of the thermocouple means the time the probe takes to respond to changes in its surrounding temperature. Assuming the bead shape is sphere, the time constant can be rewritten as:

$$\tau = \frac{\rho_b c_{p,b} d_b^2}{6\mathrm{Nu}\lambda_g} \tag{7}$$

In Eqs. 5 - 7, the convective heat transfer coefficient is defined as $h = \mathrm{Nu} \cdot \lambda_g / d_b$, where λ_g is the thermal conductivity of gas, d_b is the thermocouple bead diameter. The Nusselt number (Nu) is empirically associated with the Reynolds and Prandtl numbers. The Ranz-Marshall model [16] was used to calculate the convective heat transfer:

$$\mathrm{Nu} = 2.0 + 0.6\mathrm{Re}^{1/2}\mathrm{Pr}^{1/3}; \qquad 0 < \mathrm{Re} < 200 \tag{8}$$

where Re is the Reynolds number and Pr is the Prandtl number. The temperature-dependent gas properties for Re and Pr, are taken as those of air [17]; the temperature-dependent emissivity and thermophysical properties of platinum are taken from [18, 19] and are listed in *Appendix A*.

A FDS simulation of the fire yields the gas velocity distribution above the burner and evaluates the uncertainty in an in-house MATLAB code used to calculate the correction terms to determine the gas temperature as defined by Eqs. 5 - 8. The MATLAB code is verified using a sinusoidal function and validated using FDS simulation results in *Appendix D*. The FDS input code is based on the input file for the 1 m methanol fire case from the FDS Validation Manual which considers this 1 m methanol pool fire [20]. The numerical details and results of the MATLAB code are presented in *Appendix C*. The average gas velocity obtained using the calculated FDS results for 138 positions in the axial and radial directions (see Table C1), is used to calculate the Reynolds number in Eq. 8.

2.2 Heat Flux Measurements

The radiative heat flux emitted to the surroundings was measured using a wide-view angle, water-cooled, Gardon-type total heat flux gauges with 1.3 cm diameter faces. Fourteen gauges were used to measure the heat flux distribution about the pool fire as shown in Figure 4. Radial heat flux gauges were aligned along the plane of the burner rim to measure the heat flux in the downward direction. Vertical heat flux gauges were aligned to measure the heat flux in the radial direction away from the fire. In addition, Gauges 12 to 14 were moved horizontally in the radial direction, using a computer-controlled mechanical traverse. The heat flux measurement positions and the gauge information are listed in *Appendix B*. The gauges were calibrated using a standard in a well-characterized radiometer facility [21]. Voltage signals from the gauges were acquired at 1 Hz and time-averaged in a steady burning. The measured heat flux was corrected considering the background heat flux from surroundings, which method is described in *Appendix E.3.1*.

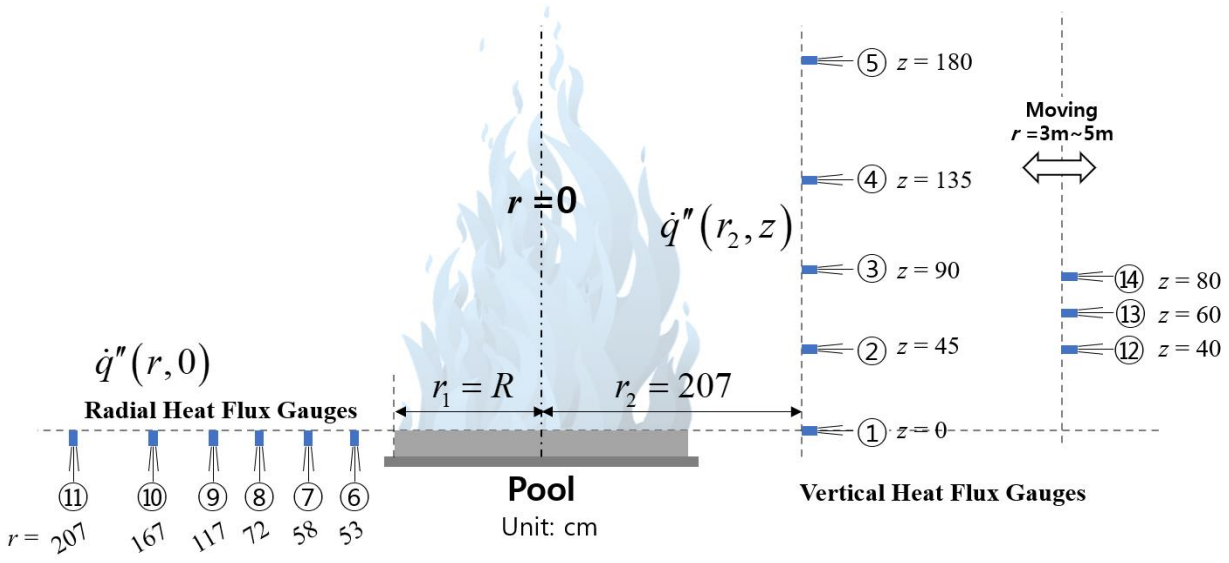

Figure 4. A schematic diagram of the heat flux gauge set-up.

2.3 Flame Height and Pulsation Frequency Measurements

A 30 Hz video record of the fires was used to determine the flame height and the dominant pulsation frequency. About 3600 frames, representing roughly 170 puffing cycles, in the video record were analyzed by MATLAB to determine the flame height. The video record of flame appearance was decompressed into RGB images. In these images, the flame region could be distinguished from the background by the value of Blue. Based on the threshold of Blue values as suggested by Otsu [22], the images were transformed into binary images. The RGB and binary images of the flame at the same frame are shown in Figure 5. The instantaneous flame height was defined as the distance between the burner and flame tip and the mean flame height (Z_f) was defined as the distance between the burner and the flame surface when the intermittency is 0.5 [23]. A fast Fourier transform was applied to the transient flame height to determine the dominant puffing frequency.

The experimental measurements were compared to the empirical model for the flame height suggested by Heskestad [23].

$$\frac{Z_f}{D} = 15.6\mathrm{N}^{1/5} - 1.02 \tag{9}$$

where N is the non-dimensional parameter defined by:

$$\mathrm{N} = \left[\frac{c_p T_\infty}{g\rho_\infty^2 \left(\frac{H_c}{\gamma}\right)^3}\right]\frac{\dot{Q}^2}{D^5} \tag{10}$$

where c_p is the specific heat of air at constant pressure, H_c is the actual lower heat of combustion and γ is the actual mass stoichiometric ratio of air to volatiles, ρ_∞ and T_∞ are the ambient density and

temperature, respectively, g is the acceleration of gravity, $\dot{Q}$ is the total heat release rate (given in terms of the production of the mass burning rate and the heat of combustion), and D is the diameter of the pool.

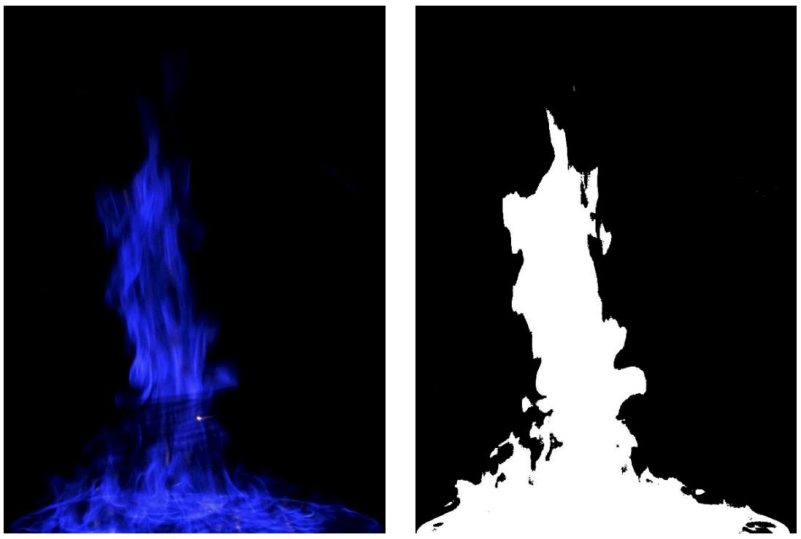

Figure 5. The RGB and binary images of flame at the same frame recorded with a video.

2.4 Liquid Fuel Temperature Measurements

A manually adjustable vertical mount was used to measure the vertical temperature distribution in the liquid fuel. A ½ mm diameter bare-bead K-type thermocouple was attached to the tip of the vertical mount and the vertical position was monitored with a strain gauge shielded with aluminum foils to prevent heat transfers from the fire. The radial position of the thermocouple was fixed at r = 35 cm, and the thermocouple was moved vertically in the range from -5 cm to 1 cm below the fuel surface. Temperature data were acquired for 30 s at each position at 1 Hz sampling rate. The measurement was repeated twice at 10 min and 45 min after the fire ignition in the steady fire conditions.

3 Results and Discussion

3.1 Flame Appearance

The shape of the fire dramatically changed during its pulsing cycle. The fire was blue with no indication of the presence of soot. This is a low Froude number fire with a narrow necking region, almost quasi-laminar in appearance. The fire is three dimensional by its nature and very complex, characterized by at least two obvious instability phenomena. The first is associated with the well-recognized large-scale puffing phenomena with a physical scale on the order of the pool radius. The second occurs near the fuel surface, where flames form a series of channels and nodes that flow from the burner rim across and very near to the fuel surface Three flames merge near the center of the fire, with air entraining, the plume begins to form and the fire turns upward, a structure that leads to the creating of a fuel rich fuel core above the center of the pool. The observed dynamics are consistent with the careful description given by Weckman and Sobiesiak [24] for a medium-scale acetone pool fire and with the analysis given by Baum

and McCaffrey [25]. The difference is that the low Froude number methanol fire has an even narrower necking region as seen in Figure 6, which shows four sequential images of the pulsing methanol pool fire. A series of repeated cycles in which orderly curved flame sheets anchored at the burner rim were connected to the central fire plume and rolled towards the fire centerline, necked-in to form a narrow and long visible fire plume. Figure 7 shows a blow-up of the second image from the left in Figure 5. The channel/node pairs are seen to extend from the burner rim towards the fire center where they merge. Similar "saw-toothed" flames have been observed repeatedly in laboratory and field-scale wildland fires, which were identified as similar to counter-rotating Taylor-Görtler vortex pairs oriented in the streamwise direction with alternating upward and downward flows [26]. The basic difference here is that the perimeter is a circle rather than a line. Radiative and convective heat transfer to the fuel surface and the fuel mass burning rate is impacted by these three-dimensional structures, which occur so close to the pool surface. About 48 ± 4 of these channel/node pairs are observed in the 1 m methanol pool. This is much larger than the 8 channels/node pairs seen in the 30 cm methanol pool fire [27]. The number of nodes/channel pairs per unit pool surface perimeter for the methanol fires are 15.3 m^{-1} ± 1.3 m^{-1} and 8.5 m^{-1} for the 1 m and 0.30 m diameter pools, respectively. Further investigation of these structures would provide a more complete understanding of this phenomena would inform the understanding of the methanol pool fire's burning rate and dynamics.

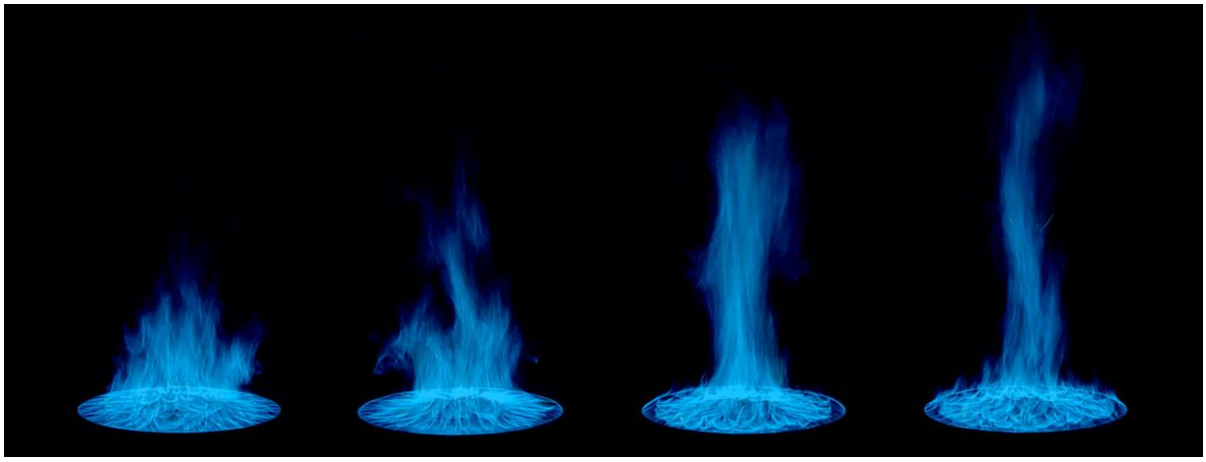

Figure 6. Instantaneous sequential digital images of the pulsing 1 m diameter methanol pool fire.

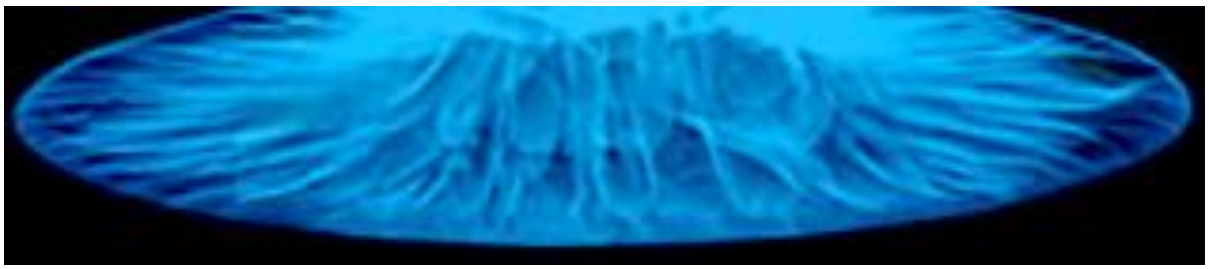

Figure 7. Blow-up of the second image from the left in Figure 6, showing channel/node pairs extending from the burner rim towards the fire center where they turn upwards and merge with the central fire plume.

This publication is available free of charge from: https://doi.org/10.6028/NIST.TN.2083r1

3.2 Mass Burning Rate

With a steady liquid level in the fuel pool, the mass burning rate was measured by monitoring the mass loss in the 20 L methanol reservoir feeding the liquid pool, using a calibrated load cell. Figure 8 shows the time-varying fuel mass in the reservoir during Test 3. When the fuel was low in the reservoir, it needed to be replenished. The periods when the reservoir was refilled are indicated by the white (unshaded) regions. During these periods, the fuel was still fed to the burning pool and the fuel level in the pool was maintained constant as verified by a video camera focused on the relative level of the fuel compared to the fuel level indicator (see Figure 2). The burning rate is estimated during the gray regions in the figure, that is, after an initial warm-up and avoiding periods when fuel was added to the reservoir. The total mass loss rate for each period is noted (by the numbers in the gray regions in the figure) by considering the ratio of the mass loss to the duration of the period. The time-weighted mean mass burning rate during the three tests was 12.8 g/s ± 0.9 g/s, representing a 95 % confidence interval (a coverage factor of two). This represents a mass flux of 16.3 g/m^2-s ± 1.1 g/m^2-s.

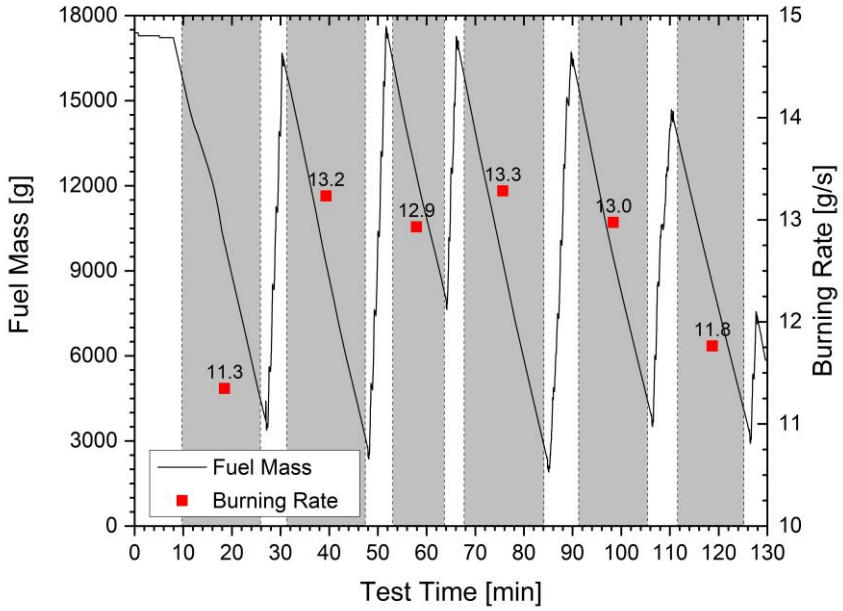

Figure 8. Mass of fuel reservoir and average fuel burning rate during Test 3. The unshaded regions after 10 min represent times when the reservoir was being refilled with methanol.

3.3 Heat Release Rate

The heat release rate was measured using oxygen consumption calorimetry and compared with the ideal heat release rate ($\dot{Q}$), i.e., $\dot{m}\Delta H_c$ where ΔH_c is the net heat of combustion of methanol equal to 19.9 kJ/g [17]. The actual heat release rate from calorimetry was averaged for the three tests once the fire reached steady-state burning. The measured mass burning rate, the ideal heat release rate, and the actual heat release rate measured via the oxygen consumption calorimetry are presented in Table 1. As expected, the ideal heat release rate agrees well with the measured calorimetric heat release rate since the combustion efficiency is expected to be nearly 1.0. The actual heat release rate was 256 kW ± 45 kW.

This publication is available free of charge from: https://doi.org/10.6028/NIST.TN.2083r1

Table 2. Measured mass burning rate in the 1 m methanol pool fire, the ideal heat release rate determined from the measured mass burning rate, and the actual heat release rate obtained from calorimetry; The uncertainty is expressed as the expanded uncertainty representing a 95 % confidence interval.

Mass Burning Rate $\dot{m}$ **[g/s]**	**Ideal Heat Release Rate** $\dot{Q}$ **[kW]**	**Actual Heat Release Rate from Calorimetry** $\dot{Q}_a$ **[kW]**
12.8 ± 0.9	254 ± 19	256 ± 45

3.4 Flame Height and Pulsation

The mean flame height was measured as 1.10 m ± 0.22 m from the burner rim. Using Eqs. 9 - 10, with γ = 6.47, D = 1 m, and $\dot{Q}$ = 254 kW, the flame height was calculated as 1.16 m, in agreement with the measured value. Calculating the fast Fourier power spectrum of the time-varying flame height, the relationship between frequency and amplitude is shown in Figure 9. The dominant frequency of the pool fire was about 1.37 Hz consistent with previous studies [28]. The first harmonic of the dominant frequency is also evident, exemplifying the repetitive and coherent nature of this pulsing fire.

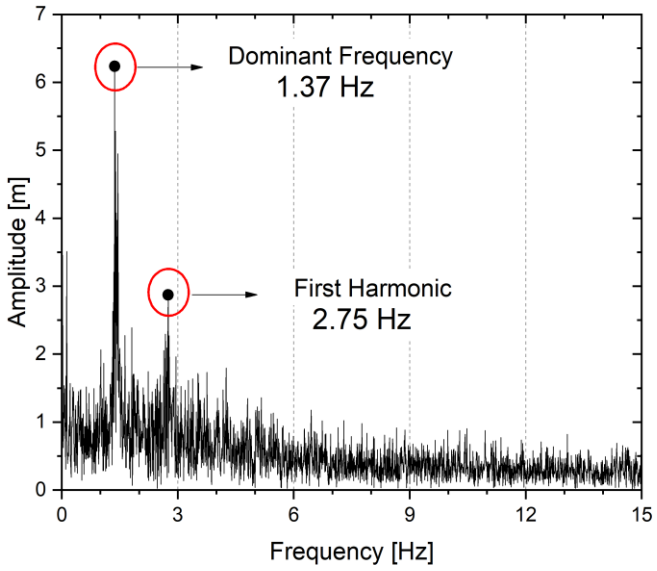

Figure 9. Fast Fourier power spectrum of the time-varying flame height.

3.5 Heat Flux Distribution

Figure 10 shows the mean and standard deviation of the radiative heat flux as a function of the radial and axial distances from the burner center. As expected, the radiative heat flux rapidly decreases with distance from the centerline. The maximum radial heat flux was 5.1 kW/m^2 ± 1.0 kW/m^2. The heat flux decreased consistently proportional to $1/r^2$ as seen in the figure. There was little change in the radiative heat flux in the axial direction. The heat flux has a maximum value of 1.0 kW/m^2 ± 0.1 kW/m^2 at 0.9 m height above the burner.

This publication is available free of charge from: https://doi.org/10.6028/NIST.TN.2083r1

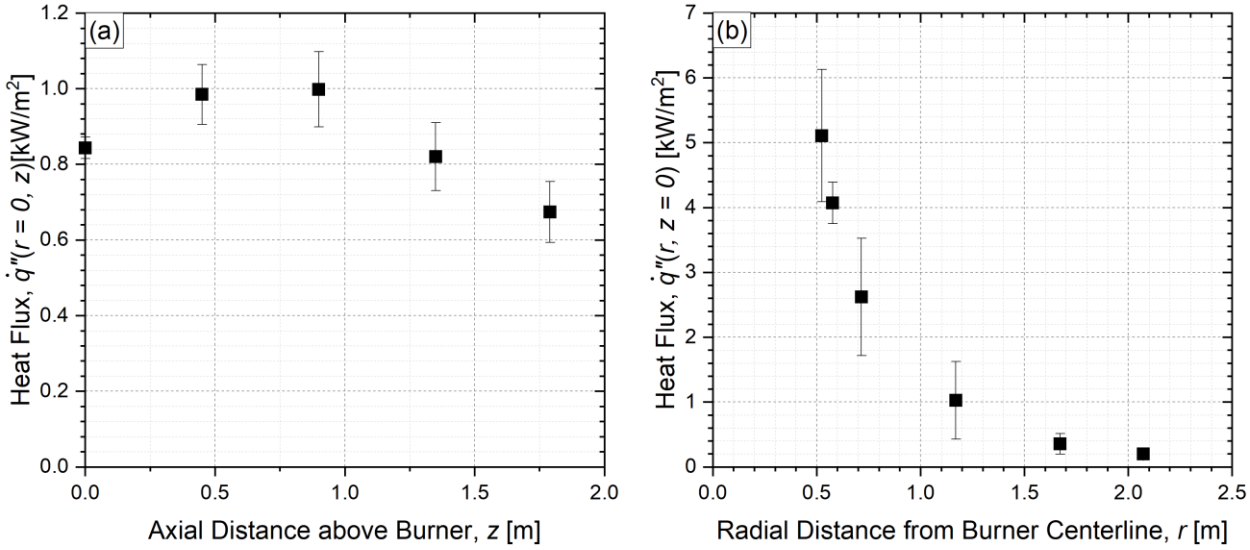

Figure 10. Mean and standard deviation of the corrected heat flux as a function of; (a) the radial distance from the burner centerline at z = 0, (b) the axial distance above the burner at r = 2.07 m.

The measured results in Figure 10 were compared with the heat flux distribution in 1 m methanol pool fire experiment conducted by Klassen and Gore [11] shown in Figure 11. The vertical heat fluxes were larger than those measured in Ref. [11] due to the position of the gauges, which were located at r = 2.07 m, rather than 3.3 m from the pool centerline. To compare the results in Figure 11a, heat flux values in Ref. [11] were scaled by the factor of $(3.3/2.07)^2$ based on the correlation of $\dot{q}'' \sim 1/r^2$. The scaled heat fluxes agree with the results of the present study within experimental uncertainty as seen in Figure 11a. Radial heat flux values were in good agreement with the results of the previous study.

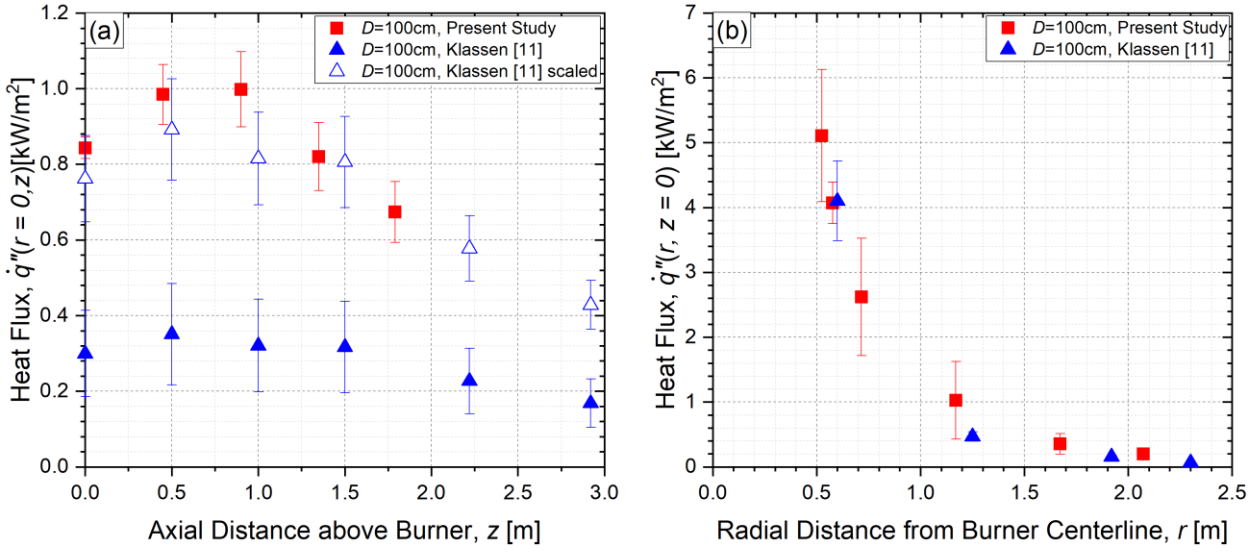

Figure 11. Mean and standard deviation of the corrected heat flux as a function of; (a) the radial distance from the burner centerline at z = 0, (b) the axial distance above the burner at r = 2.07 m.

This publication is available free of charge from: https://doi.org/10.6028/NIST.TN.2083r1

Figure 12a shows the mean and variance of normalized heat flux as a function of axial distance normalized by the pool diameter. Figure 12b shows the mean and variance of the heat flux incident on the floor as a function of radial distance normalized by the pool diameter, comparing 7.1 cm, 30 cm and 100 cm methanol pool fires. The radial heat flux values were in good agreement with the results of the previous study.

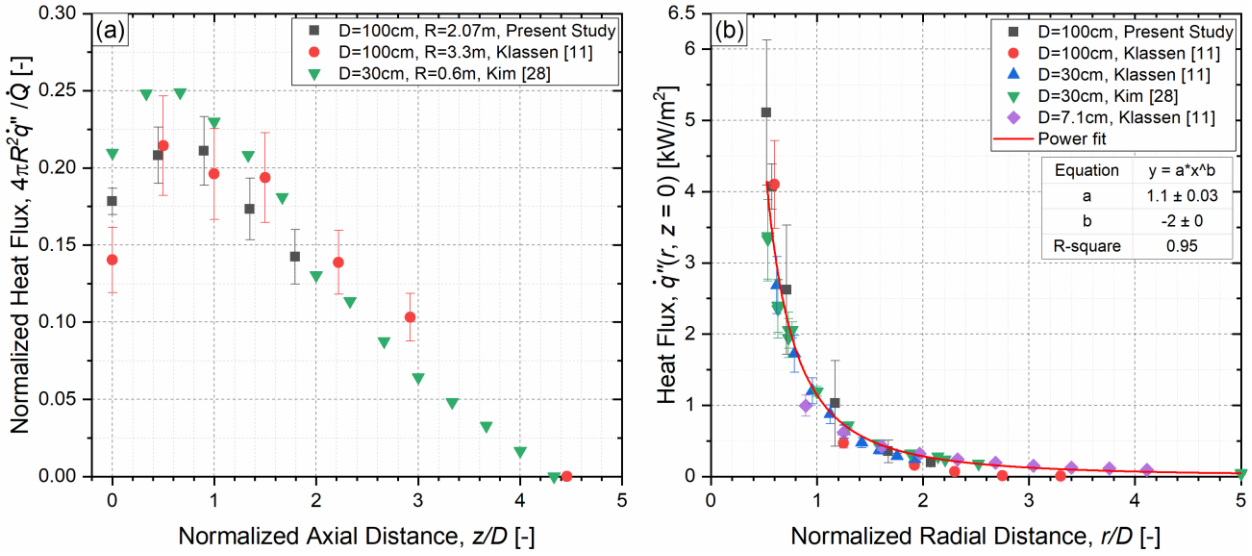

Figure 12. (a) Mean and standard deviation of the heat flux normalized by the total heat release rate as a function of the axial distance normalized by the pool diameter, (b) Mean and standard deviation of the heat flux as a function of the radial distance normalized by the pool diameter. The measurements are compared to previous results for 7.1 cm and 30 cm, and 100 cm methanol pool fires.

3.6 Radiative Fraction

The fraction of energy radiated from the fire, χ_{rad}, was calculated using Eqs. 11 - 12, considering the overall enthalpy balance explained in Ref. [29], where its value is equal to the ratio of the total radiative emission from the fire ($\dot{Q}_{rad}$) normalized by the ideal heat release rate ($\dot{Q}$). The radiative fraction (χ_{rad}) can be broken into the sum of the radiative heat transfer to the surroundings (χ_r) and onto the fuel surface (χ_{sr}) normalized by the heat release rate, such that:

$$\chi_{rad} = \chi_r + \chi_{sr} = \dot{Q}_{rad}/\dot{Q} \tag{11}$$

$$\chi_r = \dot{Q}_r/\dot{Q} \quad \text{and} \quad \chi_{sr} = \dot{Q}_{sr}/\dot{Q} \tag{12}$$

where $\dot{Q}_r$ is the radiative energy emitted by the fire to the surroundings except to the fuel surface and $\dot{Q}_{sr}$ is the radiative heat feedback to the fuel surface. Assuming symmetry, integrating the measured local radiative heat flux in the r and z directions (see Figure 4) yields the total energy radiated by the fire, ($\dot{Q}_{rad}$), considering the flux through a cylindrical control surface about the pool fire as seen in Figure 13. This method assumes that the radiation emitted through the top of the cylinder is very small relative to the total flux emitted when the wall of the control volume is sufficiently tall. The control volume method was

This publication is available free of charge from: https://doi.org/10.6028/NIST.TN.2083r1

verified by comparing the results with the radiative fraction estimated using a single location heat flux measurement applying the conditions as suggested by Ref. [30], (see *Section 3.6.2*). The results agree within experimental error, demonstrating the viability of the control surface methodology.

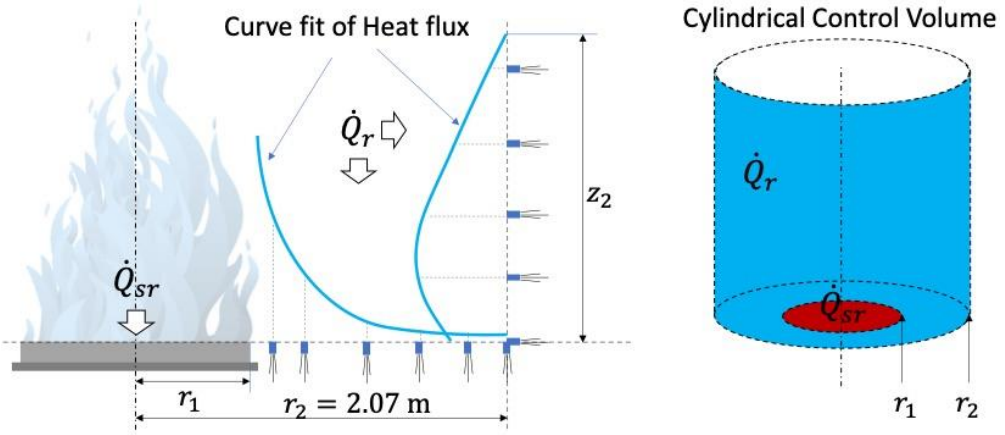

Figure 13. A schematic diagram of the radiative fraction estimate considering the heat flux through a cylindrical control volume about the fire.

The total energy radiated by the fire ($\dot{Q}_{rad}$) is estimated as:

$$\dot{Q}_{rad} = \dot{Q}_r + \dot{Q}_{sr} = \left(2\pi \int_{r_1}^{r_2} \dot{q}''(r,0) \cdot r dr + 2\pi r_2 \int_0^{z_2} \dot{q}''(r_2,z) dz\right) + \pi r_1^2 \overline{\dot{q}''_{sr}} \qquad (13)$$

where r_1 and r_2 are 0.5 m and 2.07 m, z_2 is 3.62 m, and $\overline{\dot{q}''_{sr}}$ is the average radiative heat flux incident on the fuel surface. In the energy balance for a steadily burning pool fire following Ref. [29], the total heat feedback ($\dot{Q}_s$) to the fuel surface is broken into radiative and convective components, that is, $\dot{Q}_s = \dot{Q}_{sr} + \dot{Q}_{sc}$. Normalizing by $\dot{Q}$, then $\chi_s = \chi_{sr} + \chi_{sc}$. Kim et al. [29] measured the distribution of local heat flux incident on the fuel surface in a 30 cm methanol pool fire. The fractional total heat feedback (χ_s) was 0.082 ± 24 % with 67 % of the feedback attributed to radiation, that is, χ_{sr} = 0.055 ± 21 %. Here, the fractional heat feedback to the fuel surface (χ_s) in the 1 m pool fire is assumed to be about the same as in the 30 cm pool fire [29]. Using thin film theory, it is possible to estimate the convective heat transfer to the fuel surface following [31]:

$$\dot{Q}_{sc} = A\left(\frac{h}{C_p}\right)\left[\Delta H_c(\chi_a - \chi_{rad})r_o/\chi_a - C_p(T_s - T_o)\right]y/(\exp(y) - 1) \qquad (14)$$

where A is the pool surface area, $y(= \dot{m}'' C_p/h)$ is a blowing factor, $\dot{m}''$ is the fuel mass flux, r_o is the stoichiometric fuel/air mass ratio, T_s is the burner surface temperature, T_o is the ambient temperature, and C_p is the heat capacity of air taken here at 750 K, which is representative of a temperature intermediate between the flame temperature and the burner surface temperature. The heat transfer coefficient (h) is taken as 8.5 W/(m^2·K) for a pool with "lips" [31]. Applying Eq. 14 yields χ_{sr} = 0.065 ± 31 % and χ_{sr}/χ_s = 0.80, which is about 20 % larger than its value in the 0.3 m methanol pool [29].

This publication is available free of charge from: https://doi.org/10.6028/NIST.TN.2083r1

3.6.1 Total Radiative Emission

The fitting functions seen in Figure 14 were used to integrate the heat flux in the radial and vertical directions. The zero-heat flux position (z_2 = 3.62 m) was extrapolated from the values of the last two locations in Figure 14a. In previous studies [11, 29], the heat flux peaked at a vertical position equal to approximately one half of the characteristic flame height and decreased almost linearly above the visible flame tip regardless of pool diameter and fuel type, until it reached zero. The vertical radiative heat flux (the second term in Eq. 13) was integrated using the cubic function from 0 to z_1 (1.6 m) and either the cubic function or a line in the region from z_1 to z_2, as seen in Figure 14a. The energy difference associated with the fitting functions was treated as an uncertainty contribution to the measurement.

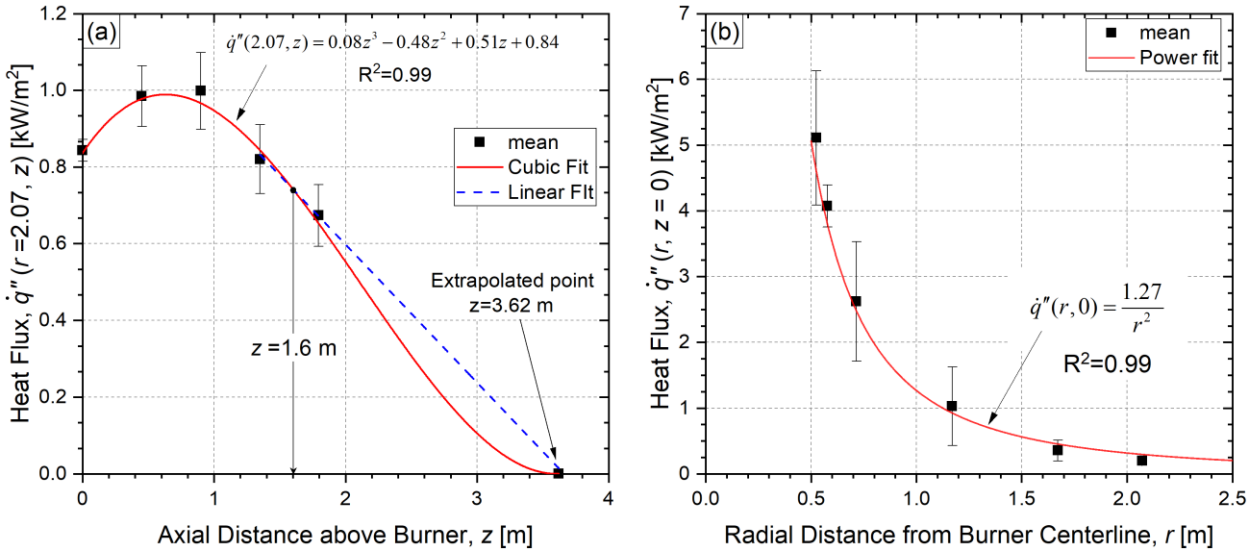

Figure 14. Mean and standard deviation of the radiative heat flux as a function of; (a) axial distance above the burner, (b) radial distance from the burner centerline.

3.6.2 Comparison of Radiative Emission and Radiative Fraction to Previous Work

The results showed that $\dot{Q}_{rad}$ = 56 kW ± 11 % and χ_{rad} = 0.22 ± 16 %. The radiative fraction of the total heat release rate emitted to the surroundings in previous studies for methanol pool fires is listed Table 3. The radiative fraction reported here for the 1 m methanol pool fire agrees with the value in Ref. [11] within the expanded uncertainty (see Table 3). The radiative fraction for the 1 m pool fire was similar to its value in the 30 cm fire, and agreed with the result in Ref. [29] which showed that the radiative fraction was fairly constant for pool diameters less than 2 m.

This publication is available free of charge from: https://doi.org/10.6028/NIST.TN.2083r1

Table 3. Comparison of the radiative fraction in steadily burning 30 cm and 100 cm methanol pool fires. The expanded uncertainty is also shown, repenting a 95 % confidence interval.

Research	Pool diameter [cm]	χ_{rad}
Present study	100 cm	0.22 ± 16 %
Klassen and Gore [11]	100 cm	0.19[a,b]
Kim et al. [29]	30 cm	0.24 ± 25 %
Hamins et al. [32]	30 cm	0.22 ± 10 %
Klassen and Gore [11]	30 cm	0.22[a,b]

[a] $\overline{\dot{q}_{sr}}''$ in Eq. 13 was assumed equal to the heat flux measured next to the burner ($\dot{q}''(51cm, 0)$ = 4.1 kW/m^2), which yields χ_{sr} = 0.01, which is smaller than expected in Ref. [29]. χ_{rad}, therefore, was recalculated with χ_{sr} = 0.055, yielding $\chi_{rad} = 0.19$.

[b] Recalculated χ_{rad}, using ΔH_c = 19.918 kJ/g [17], not 22.37 kJ/g assuming gaseous water as a product of combustion.

The radiative heat flux to an external element becomes more isotropic as the flame becomes optically thin or as the distance to the gauge increases [30]. Assuming isotropy, the radiative energy from the fire $\dot{Q}_{rad}$ can be expressed as:

$$\dot{Q}_{rad} = 4\pi r^2 \dot{q}''(r, z) \tag{15}$$

Modak [30] suggested that a distance five times the diameter of the fire is adequate to use a single point location estimate of the total radiative flux, which is known as a single point estimate. The results show the flame radiative power output underestimates the total radiative energy emitted by the flame with a bias of about 2 % at r/D = 5. Figure 15 shows the mean and standard deviation of the radiative heat flux as a function of the radial distance normalized by the pool diameter. The mean heat flux obtained from Gauge 12 - 14 was averaged in each radial position, the error bar indicates the standard deviation of the transient heat flux. The maximum deviation for the mean heat flux was 3 % at r/D = 4.5. The result shows the radiative heat flux at r/D = 5 was isotropic. Applying the single point estimate with the radiative heat flux at r = 500 cm, the radiative fraction according to the axial distance was presented in Table 4. The mean radiative fraction was 0.20 ± 34 %, which agrees with the radiative fraction using the radiative energy integrated in a cylindrical volume, χ_{rad} = 0.22 ± 16 %, presented in Table 3.

This publication is available free of charge from: https://doi.org/10.6028/NIST.TN.2083r1

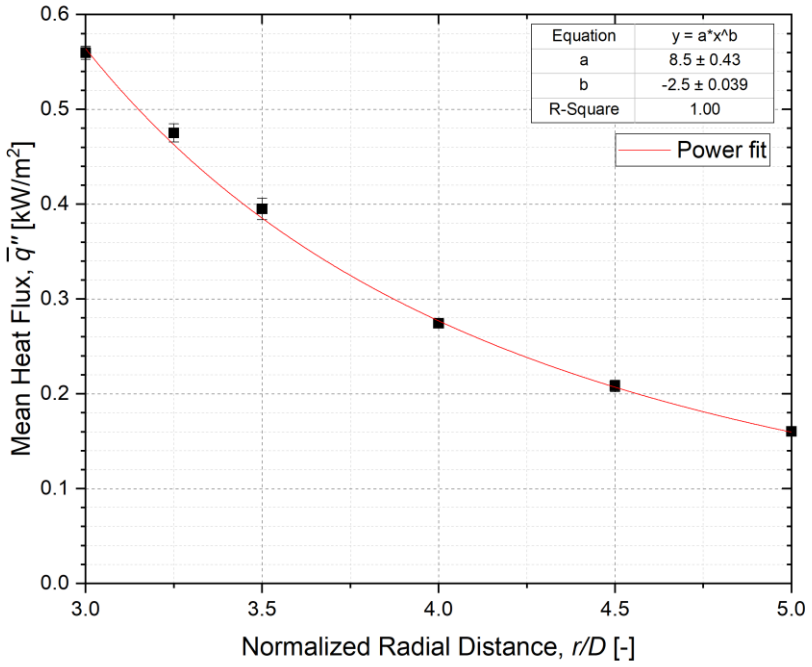

Figure 15. Mean and standard deviation of the radiative heat flux as a function of the radial distance normalized by the pool diameter from the burner centerline with the gauges faced to the fire. The error bar indicates the standard deviation of the heat flux obtained from Gauge 12 - 14 located at z = 40 cm, 60 cm and 80 cm, respectively.

Table 4. Radiative fraction based on a single point estimate at r = 500 cm with the expanded uncertainty, representing a 95 % confidence interval.

z [cm]	r [cm]	χ_{rad} [-]
40	500	0.19 ± 33 %
60	500	0.20 ± 37 %
80	500	0.19 ± 33 %

3.7 Gas-Phase Temperature Distribution

Figure 16 shows the measured time series of the bead temperature ($T_b(t)$), the temperature ($T_r(t)$) corrected for radiative loss (but not for thermal inertia), and the gas temperature ($T_g(t)$) corrected for both radiative loss and thermal inertia effects. There is no time delay between the bead temperature and the radiation corrected temperature as seen in Figure 16a. The radiative correction term in Eq. 5 becomes larger as the bead temperature increases with the maximum correction equal to 55 K, when $T_b(t)$ =1694 K. On the other hand, the extremes of the corrected gas temperature shift earlier in time as compared with the bead temperature due to the thermal inertia of the thermocouple as seen in Figure 16b.

The magnitudes of the time shift and the temperature correction due to thermal inertia is related to the thermocouple time constant and the rate at which the gas temperature changes in time, represented by the terms: τ and dT_b/dt in Eq. 5. The time derivative of the bead temperature (dT_b/dt) at the extremums is

This publication is available free of charge from: https://doi.org/10.6028/NIST.TN.2083r1

zero mathematically, such that the thermal inertia correction is zero at that instant. The larger the temperature gradient immediately before an extreme, the larger the thermal inertial caused time shift and temperature correction. As expected, the extremes of the gas temperature, including the peak, are shifted forward in time, compared with the thermocouple bead temperature as seen in Figure 16b. The minimum correction is 7 K, when $T_b(t)$ =1070 K in the figure. The mean time constant (Eq. 7) is nearly constant, calculated as 57 ms ± 3 ms as seen in Figure 16c.

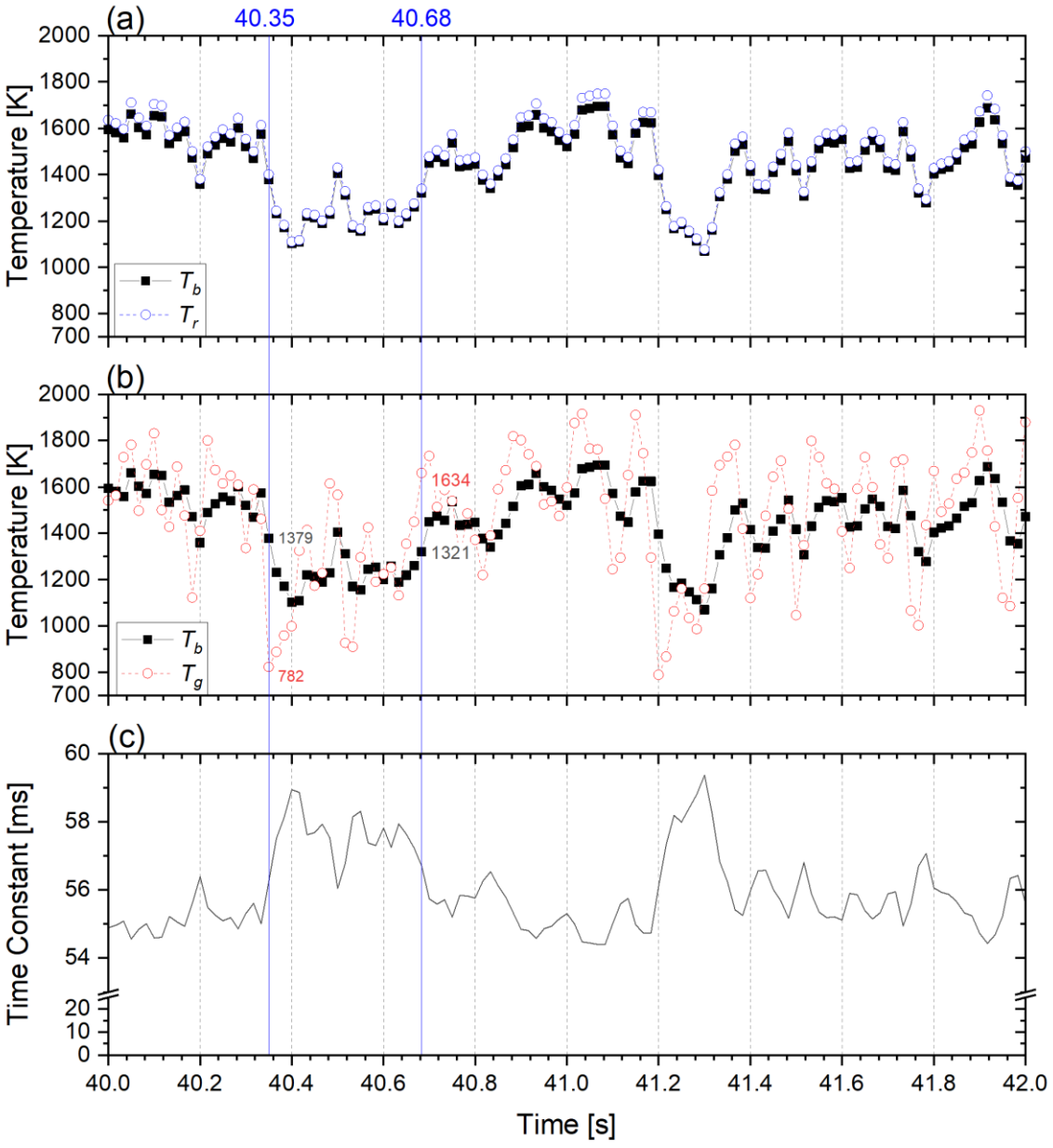

Figure 16. Instantaneous temperature at (z, r) = (30 cm, 0 cm) in Test 3; T_b is the bead temperature, T_r is the corrected temperature considering only radiative loss, and T_g is the gas temperature corrected for radiative loss and thermal inertia. The bottom plot shows the time constant as a function of time.

This publication is available free of charge from: https://doi.org/10.6028/NIST.TN.2083r1

The mean and standard deviation of the time series data sets of the corrected gas temperature (T_g), the measured thermocouple bead temperature (T_b), the radiative loss correction term (T_{rad}) and thermal inertia correction term (T_{the}) are listed in Table E5. Here, the mean and standard deviation values are estimated for 120 s at (z, r) = (30 cm, 0 cm). Figure 16 shows the instantaneous thermal inertia correction term continuously changes, taking on values as large as many hundreds of degrees, whereas its mean value is less than 1 K. In other words, the thermal inertia correction term has a negligible influence on the mean gas temperature, but does amplify the value of the instantaneous temperature extremes, consistent with the findings of Weckman and Strong [4]. Table E1 shows the mean and standard deviation of the three temperatures, T_b, T_{rad} and T_{the}, along the burner centerline. Other locations yield similar results (See *Appendix E.1*).

The uncertainty analysis of the instantaneous gas temperature is conducted in *Appendix E.1.1*. In the Appendix, contributions to the uncertainty of the instantaneous gas temperature by uncertainties in the bead temperature, the radiation correction term, and the inertia correction term are described in detail. The results show that $u_c(T_{the})$ is the dominant contributor to the uncertainty is the corrected gas temperature, $u_c(T_g)$, for T_g < 700 K or T_g > 2000 K, whereas for 700 K < T_g < 2000 K, the uncertainty of the bead temperature must also be considered. For these reasons, the uncertainties of the mean and standard deviation of the gas temperature are separately analyzed in *Appendix E.1.2*.

Table 5. Mean and standard deviation of the corrected gas temperature (T_g), the measured thermocouple bead temperature (T_b), the radiative loss correction term (T_{rad}) and the thermal inertia correction term (T_{the}) for one fire location, (z, r) = (30 cm, 0 cm); (Experiment date: 03/11, Repeat no. 3).

Value	T_g	T_b	T_{rad}	T_{the}
Mean [K]	1337	1315	22	0.2
Std. Dev. [K]	385	237	13	293

Figure 17 shows the mean and standard deviation of the bead temperature, corrected gas temperature and time constant as a function of axial distance above the burner along the centerline of the fire in Test 3. As expected, the mean gas temperatures were slightly larger than the mean bead temperature for all positions due to the correction for radiative losses. In Figure 17, the mean time constant is roughly inversely proportional to the mean gas temperature, in agreement with the trend of the instantaneous time constant seen in Figure 16c.

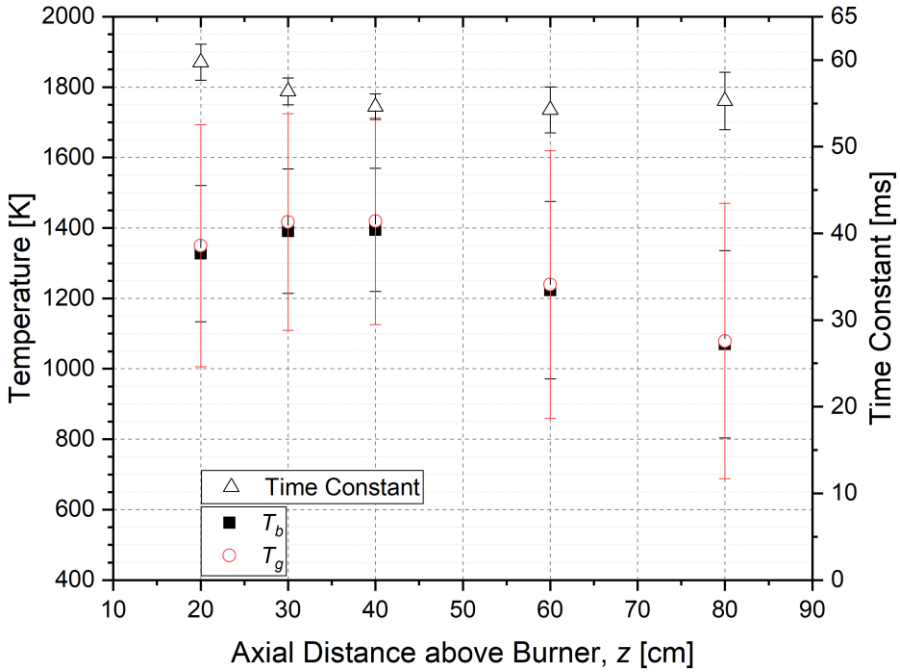

Figure 17. Mean and standard deviation of the measured bead temperature profile and the corrected gas temperature and thermocouple time constant as a function of axial distance above the burner in Test 3.

The mean and standard deviation of the gas temperature as a function of distance above the burner along the centerline are shown in Figure 18. The maximum value of the mean temperature was about 1370 K, which occurred 0.3 m above the burner. The gradient near the fuel surface is steep. At 0.05 m above the burner, the gas temperature was about 1144 K ± 424 K. The temperature at two locations on the fuel surface was measured to be at the boiling point of methanol, 338 K, yielding a temperature gradient near the fuel surface of about 161 K/cm ± 85 K/cm (see *Section 3.8* for a discussion of the liquid temperature at and below the surface).

This publication is available free of charge from: https://doi.org/10.6028/NIST.TN.2083r1

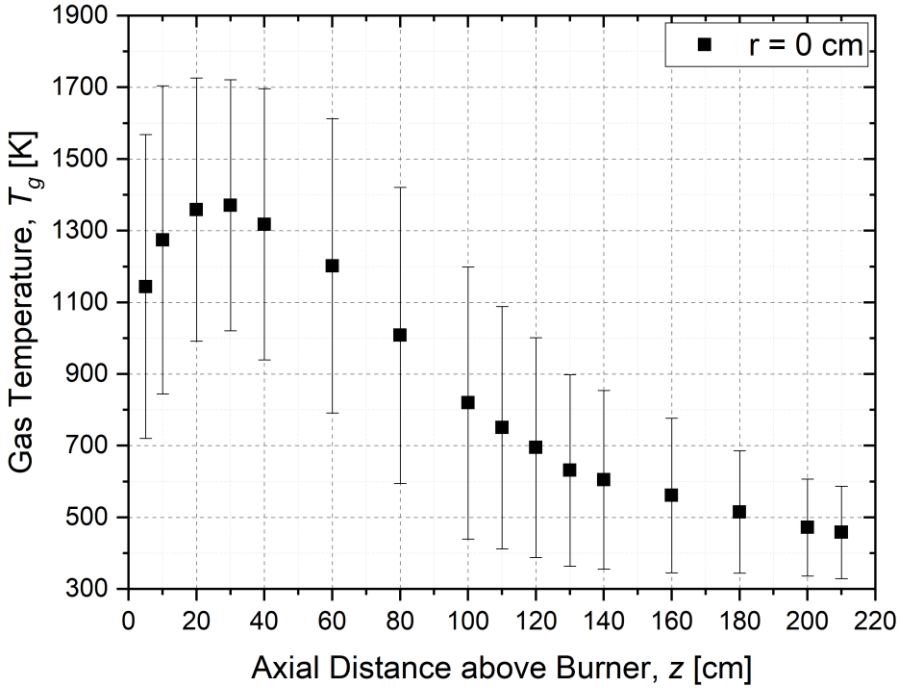

Figure 18. Mean and standard deviation of the gas temperature profile as a function of the axial distance above the burner along the centerline.

Figure 19 shows the mean and standard deviation of the gas temperature profile in the radial direction for various axial distances above the burner (20 cm $\leq z \leq$ 180 cm). The maximum temperature occurs near the centerline for each elevation. The gradient diminished with axial distance above the fuel surface.

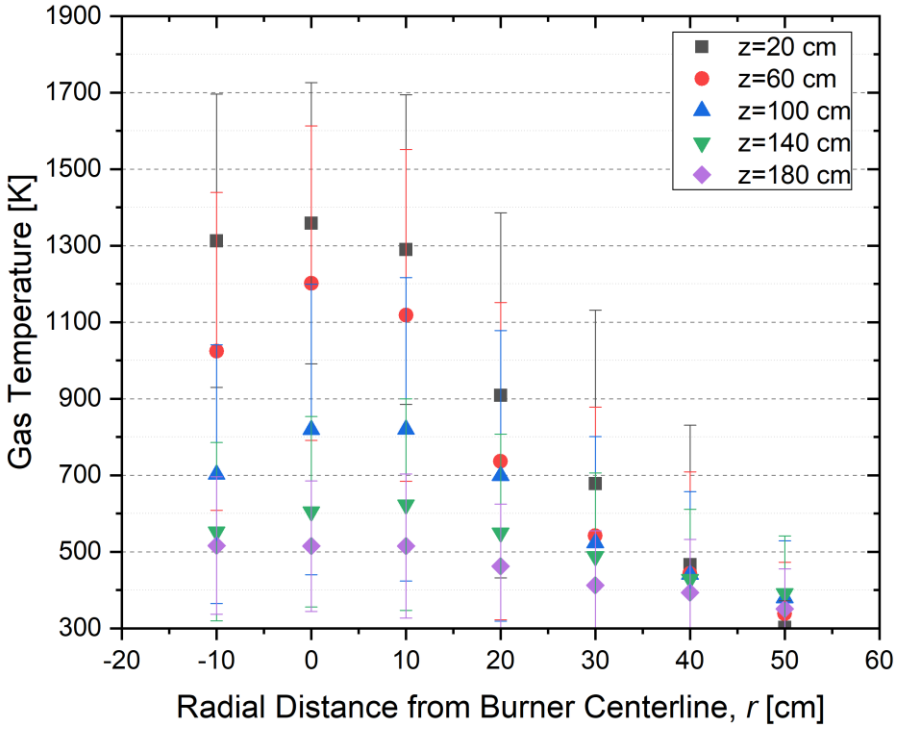

Figure 19. Mean and standard deviation of the gas temperature profile as a function of the radial distance from the burner centerline at various axial distances above the burner.

Figure 20 shows the ratio of the mean to the standard deviation of the gas temperature as a function of the mean temperature. The ratio was smallest for temperatures between about 450 K and 600 K, then increased continuously with the mean temperature. These results are consistent with results previously reported for a 30 cm methanol pool fire. The results suggest that these low Froude number methanol pool fires are highly structured with larger temperature fluctuations in high and low temperature fire regions. This is consistent with the idea of a fire structure with its high temperature flame sheets flapping about a spatial location such as might occur near the base of the fire, among other locations, in Figure 6.

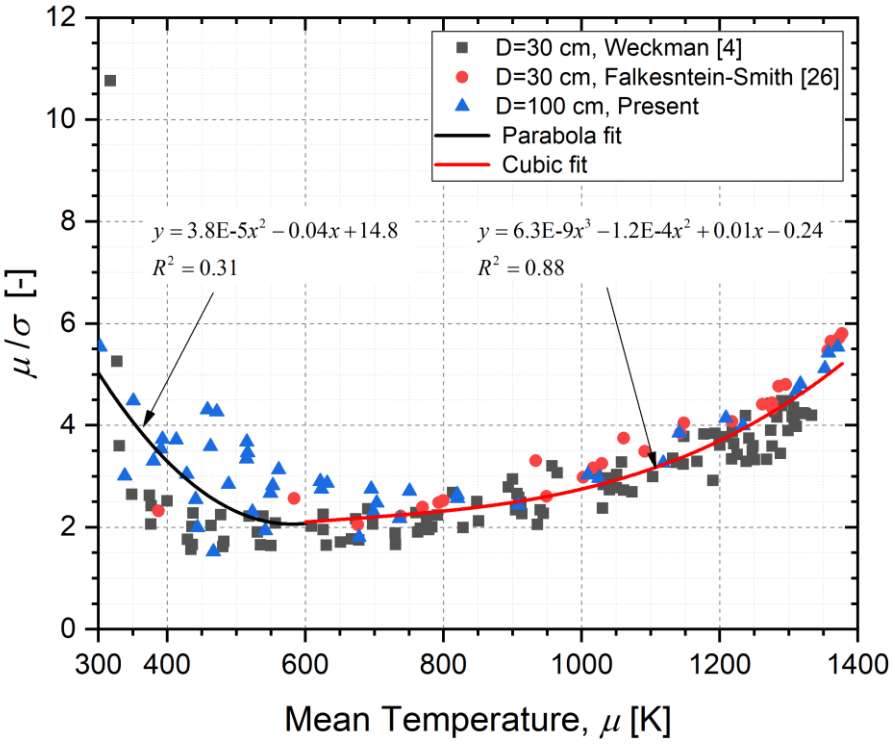

Figure 20. Ratio of the mean temperature (μ) to the standard deviation (σ) as a function of the mean temperature compared to previous results reported in 30 cm methanol pool fires.

Figure 21 shows the mean and standard deviation of the temperature profile as a function of scaled axial distance. The results are compared to previous measurements in 30 cm diameter methanol pool fires from Refs. [4, 33, 34]. Axial distance above the burner is normalized by $\dot{Q}^{2/5}$ following Baum and McCaffrey [25]. Weckman and Strong [4] measured temperature in a 30.1 cm inner diameter methanol pool fire with a lip height of 1 cm using a 50 µm wire diameter, bare bead, Type S (Pt, 10 % Rh/Pt), thermocouple similar to the thermocouples used in this study. The measurements from Ref. [33] are also shown, where temperature was measured using a 75 µm wire diameter, bare bead, Type S thermocouple in a steadily burning 30.1 cm diameter methanol pool fire with a 0.5 cm lip. The radiation corrected thermocouple measurements in Wang et al. [34] are also shown, using a 50 µm wire diameter, bare bead, Type S thermocouple in a steadily burning 30.1 cm diameter methanol pool fire with a 1 cm lip height. A comparison of the results in Figure 21 shows that the 1 m and 30 cm pool temperatures are similar when the axial distance above the burner is normalized by $\dot{Q}^{2/5}$.

This publication is available free of charge from: https://doi.org/10.6028/NIST.TN.2083r1

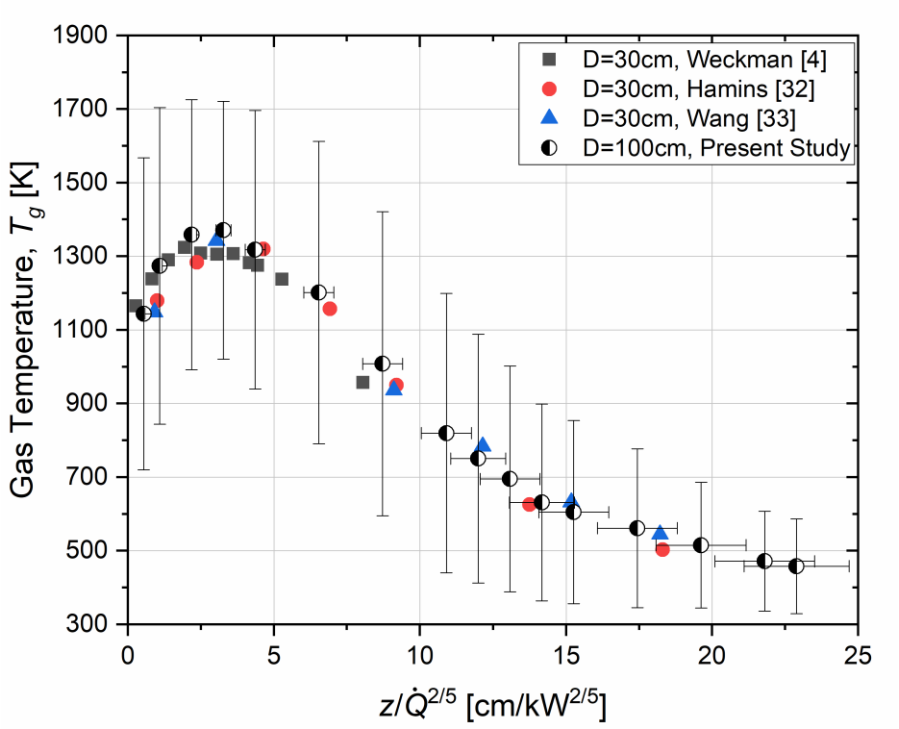

Figure 21. Mean and standard deviation of the axial temperature profiles as a function of distance above the burner normalized by $\dot{Q}^{2/5}$ and compared with the previous results in 30 cm methanol pool fires.

3.8 Liquid Fuel Temperature Profile

Figure 22 shows the mean and standard deviation of the fuel temperature as a function of the axial distance from the fuel surface in Test 1. The time difference between both measurements was 35 min. The temperature of methanol increased from the bottom of the pool to the fuel surface until it approximately reached the boiling point of methanol at the pool surface. As expected, the liquid temperatures during Measurement 2 were higher than the temperatures during Measurement 1, because the liquid fuel had received an additional heat feedback from the fire continuously. The key finding is confirmation that the surface temperature is approximately the boiling point within experimental accuracy as described by Spalding [35]. The mean and standard deviation of the liquid fuel temperature are described in *Appendix F*.

This publication is available free of charge from: https://doi.org/10.6028/NIST.TN.2083r1

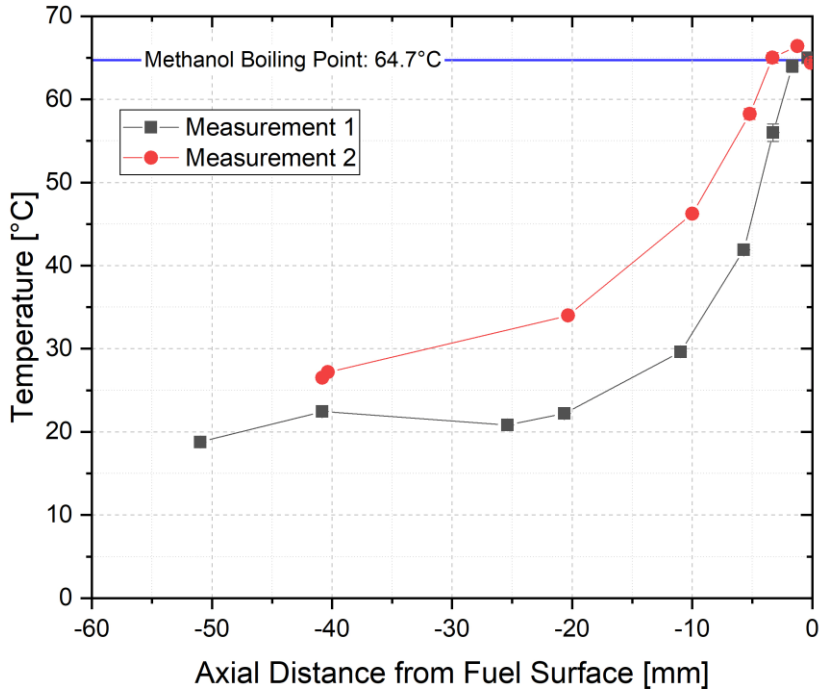

Figure 22. Mean and standard deviation of the fuel temperature as a function of the axial distance from the fuel surface in Test 1. The uncertainty in the temperature measurement is 2 °C.

4 Summary and Conclusions

A series of measurements were conducted to characterize the gas phase temperature, the burning rate, and heat release rate of a 1 m diameter, well-ventilated, methanol pool fire steadily burning in a quiescent environment. The gas-phase thermocouple temperatures were corrected considering radiative loss and thermal inertia effects. The corrected profile of mean axial temperature was shown to be similar to previous results for methanol pool fires when scaled by $\dot{Q}^{2/5}$. The average steady-state mass burning rate was measured as 12.8 g/s ± 0.9 g/s, which yields an idealized heat release rate of 254 kW ± 19 kW. The measured heat release rate using oxygen consumption calorimetry was 256 kW ± 45 kW, which was consistent with the mass burning rate measurement. The maximum corrected mean and standard deviation of temperature measured in the fire was 1371 K ± 247 K, which occurred on the centerline, 30 cm above the burner rim. The radiative fraction was measured as 0.22 ± 16 %, consistent with previous results. Observations were made of the peculiar transient structure of channels and nodes near the fuel surface. These results help characterize the structure of the steadily-burning 1 m diameter methanol pool fire and provide data that may be useful to help guide the development of fire models and to evaluate their accuracy.

References

1. Akita, K. and Yumoto, T., Heat Transfer in Small Pools and Rates of Burning of Liquid Methanol, *Proceedings of the Combustion Institute*, ***10***, 943-948, (1965).
2. Hamins, A., Fischer, S. J., Kashiwagi, T., Klassen, M. E. and Gore, J. P., Heat Feedback to the Fuel Surface in Pool Fires, *Combustion Science and Technology*, ***97***, 37-62, (1994), 10.1080/00102209408935367.
3. Hostikka, S., Mcgrattan, K. B. and Hamins, A., Numerical Modeling of Pool Fires Using Les and Finite Volume Method for Radiation, *Fire Safety Science*, ***7***, 383-394, (2003).
4. Weckman, E. J. and Strong, A. B., Experimental Investigation of the Turbulence Structure of Medium-Scale Methanol Pool Fires, *Combustion and Flame*, ***105***, 245-266, (1996), 10.1016/0010-21809500103-4.
5. Yilmaz, A., *Radiation Transport Measurements in Methanol Pool Fires with Fourier Transform Infrared Spectroscopy*, NIST Grant/Contractor Report GCR 09-922, January 2009.
6. McGrattan, K., Hostikka, S., Floyd, J., McDermott, R. and Vanella, M., *Fire Dynamics Simulator User's Guide*, NIST special publication 1019, Sixth Ed. (Version 6.7.5), National Institute of Standards and Technology, Gaithersburg, MD, August 2020, http://dx.doi.org/10.6028/NIST.SP.1019.
7. Maragkos, G., Beji, T. and Merci, B., Towards Predictive Simulations of Gaseous Pool Fires, *Proceedings of the Combustion Institute*, ***37***, 3927-3934, (2019), https://doi.org/10.1016/j.proci.2018.05.162.
8. Chen, Z., Wen, J., Xu, B. and Dembele, S., Large Eddy Simulation of a Medium-Scale Methanol Pool Fire Using the Extended Eddy Dissipation Concept, *International Journal of Heat and Mass Transfer*, ***70***, 389-408, (2014), https://doi.org/10.1016/j.ijheatmasstransfer.2013.11.010.
9. Tieszen, S. R., O'Hern, T. J., Schefer, R. W., Weckman, E. J. and Blanchat, T. K., Experimental Study of the Flow Field in and around a One Meter Diameter Methane Fire, *Combustion and Flame*, ***129***, 378-391, (2002), 10.1016/s0010-21800200352-8.
10. Tieszen, S. R., O'Hern, T. J., Weckman, E. J. and Schefer, R. W., Experimental Study of the Effect of Fuel Mass Flux on a 1-M-Diameter Methane Fire and Comparison with a Hydrogen Fire, *Combustion and Flame*, ***139***, 126-141, (2004), 10.1016/j.combustflame.2004.08.006.
11. Klassen, M. and Gore, J., *Structure and Radiation Properties of Pool Fires*, NIST-GCR-94-651, National Institute of Standards and Technology, Gaithersburg, MD, June 1994.
12. Peacock, R. D., Reneke, P. and Forney, G., *CFAST–Consolidated Model of Fire Growth and Smoke Transport (Version 7) Volume 2: User's Guide*, NIST Technical Note 1889v2, National Institute of Standards and Technology, Gaithersburg, MD, April 2020, http://dx.doi.org/10.6028/NIST.TN.1889v2.
13. Bryant, R. A. and Bundy, M. F., *The NIST 20 MW Calorimetry Measurement System for Large-Fire Research*, NIST Technical Note 2077, National Institute of Standards and Technology, Gaithersburg, MD, December 2019, https://doi.org/10.6028/NIST.TN.2077.
14. Taylor, B. N. and Kuyatt, C. E., *Guidelines for Evaluating and Expressing the Uncertainty of NIST Measurement Results*, NIST Technical Note 1297, National Institute of Standards and Technology, Gaithersburg, MD, September 1994.
15. Grosshandler, W. L., *RADCAL: A Narrow-Band Model for Radiation Calculations in a Combustion Environment*, NIST Technical Note 1402, National Institute of Standards and Technology, Gaithersburg, MD, April 1993.

16. Ranz, W. and Marshall, W., Evaporation from Drops, *Chem. eng. prog*, ***48***, 141-146, (1952).

17. Design Institute for Physical Properties (DIPPR 801), American Institute of Chemical Engineers, 2017.

18. Shaddix, C. R., Correcting Thermocouple Measurements for Radiation Loss: A Critical Review, American Society of Mechanical Engineers, New York, NY (US); Sandia National Labs., Livermore, CA (US), 1999.

19. Jaeger, F. M. and Rosenbohm, E., The Exact Formulae for the True and Mean Specific Heats of Platinum between 0° and 1600°C, *Physica*, ***6***, 1123-1125, (1939), https://doi.org/10.1016/S0031-89143990111-4.

20. McGrattan, K., Hostikka, S., Floyd, J., McDermott, R. and Vanella, M., *Fire Dynamics Simulator Technical Reference Guide Volume 3: Validation*, NIST special publication 1018-3, Sixth Ed., National Institute of Standards and Technology, Gaithersburg, MD, March 2020, http://dx.doi.org/10.6028/NIST.SP.1018.

21. Pitts, W. M., Lawson, J. R. and Shields, J. R., *NIST/BFRL Calibration System for Heat-Flux Gages*, Report of Test FR 4014, National Institute of Standards and Technology, Gaithersburg, MD, August 6 2001.

22. Otsu, N., A Threshold Selection Method from Gray-Level Histograms, *IEEE transactions on systems, man, and cybernetics*, ***9***, 62-66, (1979).

23. Heskestad, G., Luminous Heights of Turbulent Diffusion Flames, *Fire Safety Journal*, ***5***, 103-108, (1983), https://doi.org/10.1016/0379-71128390002-4.

24. Weckman, E. J. and Sobiesiak, A., The Oscillatory Behaviour of Medium-Scale Pool Fires, in *Proceedings of the Combustion Institute*, ***22***, pp1299-1310, (1989).

25. Baum, H. R. and McCaffrey, B. J., Fire Induced Flow Field-Theory and Experiment, in *Proceedings of the Second International Symposium on Fire Safety Science*, Hemisphere, New York, ***2***, pp129-148, (1989).

26. Finney, M. A., Cohen, J. D., Forthofer, J. M., McAllister, S. S., Gollner, M. J., Gorham, D. J., Saito, K., Akafuah, N. K., Adam, B. A. and English, J. D., Role of Buoyant Flame Dynamics in Wildfire Spread, *Proceedings of the National Academy of Sciences*, ***112***, 9833-9838, (2015), 10.1073/pnas.1504498112.

27. Falkenstein-Smith, R., Sung, K., Chen, J. and Hamins, A., The Chemical Structure of a 30 cm Methanol Pool Fire, *Fire and Materials*, 10.1002/fam.2838.

28. Hamins, A., Yang, J. C. and Kashiwagi, T., An Experimental Investigation of the Pulsation Frequency of Flames, *Proceedings of the Combustion Institute*, ***24***, 1695-1702, (1992), 10.1016/s0082-07840680198-0.

29. Kim, S. C., Lee, K. Y. and Hamins, A., Energy Balance in Medium-Scale Methanol, Ethanol, and Acetone Pool Fires, *Fire Safety Journal*, ***107***, 44-53, (2019), https://doi.org/10.1016/j.firesaf.2019.01.004.

30. Modak, A. T., Thermal Radiation from Pool Fires, *Combustion and Flame*, ***29***, 177-192, (1977), https://doi.org/10.1016/0010-21807790106-7.

31. Orloff, L. and De Ris, J., Froude Modeling of Pool Fires, *Symposium (International) on Combustion*, ***19***, 885-895, (1982), https://doi.org/10.1016/S0082-07848280264-6.

32. Hamins, A., Klassen, M., Gore, J. and Kashiwagi, T., Estimate of Flame Radiance via a Single Location Measurement in Liquid Pool Fires, *Combustion and Flame*, ***86***, 223-228, (1991), https://doi.org/10.1016/0010-21809190102-H.

33. Hamins, A. and Lock, A., *The Structure of a Moderate-Scale Methanol Pool Fire*, NIST Technical Note 1928, National Institute of Standards and Technology, Gaithersburg, MD, November 2016, https://doi.org/10.6028/NIST.TN.1928.

34. Wang, Z., Tam, W. C., Lee, K. Y. and Hamins, A., *Temperature Field Measurements Using Thin Filament Pyrometry in a Medium-Scale Methanol Pool Fire*, NIST Technical Note 2031, National Institute of Standards and Technology, Gaithersburg, MD, November 2018, https://doi.org/10.6028/NIST.TN.2031.

35. Spalding, D. B., The Combustion of Liquid Fuels, *Proceedings of the Combustion Institute*, ***4***, 847-864, (1953), https://doi.org/10.1016/S0082-07845380110-4.

36. Çengel, Y. A. and Ghajar, A. J., Heat and Mass Transfer: Fundamentals and Applications, 7th Ed., McGraw-Hill Education, 2020.

37. McGrattan, K., McDermott, R., Vanella, M., Hostikka, S. and Floyd, J., *Fire Dynamics Simulator Technical Reference Guide Volume 1: Mathematical Model*, NIST special publication 1018-1, Sixth Ed., National Institute of Standards and Technology, Gaithersburg, MD, March 2020, http://dx.doi.org/10.6028/NIST.SP.1018.

38. Tagawa, M. and Ohta, Y., Two-Thermocouple Probe for Fluctuating Temperature Measurement in Combustion—Rational Estimation of Mean and Fluctuating Time Constants, *Combustion and Flame*, ***109***, 549-560, (1997), 10.1016/s0010-21809700044-8.

39. Omega Engineering Inc., *The Temperature Handbook*, pages Z-39-40, Stamford, CT., 2004.

40. National Instruments Inc., *SCXI-1600 User Manual and Specifications*, 2004.

41. Bryant, R., Johnsson, E., Ohlemiller, T. and Womeldorf, C., Estimates of the Uncertainty of Radiative Heat Flux Calculated from Total Heat Flux Measurements, in *Proc. 9th Interflam Conference in Edinburgh, Interscience Communications London*, pp605-616, (2001).

42. Petit, C., Gajan, P., Lecordier, J. C. and Paranthoen, P., Frequency Response of Fine Wire Thermocouple, *Journal of Physics E: Scientific Instruments*, ***15***, 760-770, (1982), 10.1088/0022-3735/15/7/017.

43. Bergman, T. L., Incropera, F. P., DeWitt, D. P. and Lavine, A. S., Fundamentals of Heat and Mass Transfer, John Wiley & Sons, 2011.

44. Slack, G. A., Platinum as a Thermal Conductivity Standard, *Journal of Applied Physics*, ***35***, 339-344, (1964), 10.1063/1.1713313.

Appendices

A Thermophysical Properties

Table A1. Thermochemical properties of methanol at 20 ºC [17].

Fuel	Chemical Formula	Density [kg/m^3]	MW [g/mol]	Boiling Temperature [ºC]	ΔH_c [kJ/g]
Methanol	CH_3OH	794 ± <1 %	32.04	64.70± <1 %	19.9 ± <1 %

Table A2. Thermophysical properties of platinum as a function of temperature.

Temperature [K]	Specific heat [J/g-K] [a]	Emissivity [-] [b]
373	0.14	0.00
473	0.14	0.03
573	0.14	0.05
673	0.14	0.07
773	0.15	0.09
873	0.15	0.10
973	0.15	0.12
1073	0.15	0.13
1173	0.16	0.14
1273	0.16	0.15
1373	0.16	0.17
1473	0.16	0.18
1573	0.17	0.19
1673	0.17	0.19

[a] Ref. [19]

[b] Ref. [18]

Polynomials for the specific heat ($c_{p,b}$) and emissivity (ϵ_b) of platinum:

$$c_{p,b} = 0.13 + 2.56T$$
$$\epsilon_b = -0.1 + 3.24 \cdot 10^{-4}T - 1.25 \cdot 10^{-7}T^2 + 2.18 \cdot 10^{-11}T^3 \quad \text{(A1)}$$

This publication is available free of charge from: https://doi.org/10.6028/NIST.TN.2083r1

Table A3. Thermophysical properties of air as a function of temperature [36].

Temperature [°C]	Density [kg/m^3]	Specific Heat [J/kg/K]	Thermal Conductivity [W/m/K]	Dynamic Viscosity [kg/m/s]	Prandtl Number [-]
300	0.616	1044	0.044	2.93E-05	0.694
350	0.566	1056	0.047	3.10E-05	0.694
400	0.524	1069	0.050	3.26E-05	0.695
450	0.488	1081	0.053	3.42E-05	0.697
500	0.457	1093	0.056	3.56E-05	0.699
600	0.404	1115	0.061	3.85E-05	0.704
700	0.363	1135	0.066	4.11E-05	0.709
800	0.329	1153	0.070	4.36E-05	0.715
900	0.301	1169	0.075	4.60E-05	0.721
1000	0.277	1184	0.079	4.83E-05	0.726
1500	0.199	1234	0.096	5.82E-05	0.748
2000	0.155	1264	0.111	6.63E-05	0.754

Polynomials for the density (ρ), specific heat (c_p), thermal conductivity (λ), and dynamic viscosity (μ) of the air:

$$\rho = 351.90(T + 272.99)^{-0.9996}$$

$$c_p = 948.38 + 0.36T - 1.43\text{E-}4 \cdot T^2 + 2.20\text{E-}8 \cdot T^3$$

$$\lambda = 0.024 + 7.56\text{E-}5 \cdot T - 2.52\text{E-}8 \cdot T^2 + 4.64\text{E-}12 \cdot T^3 \quad \text{(A2)}$$

$$\mu = 1.74\text{E-}5 + 4.463\text{E-}8 \cdot T - 2.40\text{E-}11 \cdot T^3 + 1.05\text{E-}14 \cdot T^3 - 1.99\text{E-}18 \cdot T^4$$

This publication is available free of charge from: https://doi.org/10.6028/NIST.TN.2083r1

B Heat Flux Gauge Information

Table B1. Heat flux gauge measurement position and calibrated responsivity.

Index	Serial no.	Full Scale Heat Flux [kW]	r [cm]	z [cm]	Responsivity [(kW/m^2)/mV]
1	183882	10	207.5	0	$0.98x$
2	183881	10	207.5	45	$0.96x$
3	62772	50	207.5	90	$6.57x$ -0.1
4	74991	20	207.5	135	$1.47x$ -0.12
5	183892	10	207.5	179.5	$1.38x$ +0.0086[†]
6	146132	200	52.5	0	$16.56x$ +0.043
7	177176	200	57.5	0	$17.74x$ +0.084
8	177175	200	71.5	0	$17.92x$ +0.21
9	5256	100	117	0	$10.94x$ -0.090
10	150823	20	167.2	0	$2.28x$ -0.081
11	183891	10	207.2	0	$0.93x$
12	208971	1	300-500[‡]	40	$0.13x$
13	198292	2	300-500[‡]	60	$0.18x$
14	198291	5	300-500[‡]	80	$0.69x$

[†]with ZnSe window.

[‡]The gauges were mounted on a movable traverse moving in the horizontal direction.

The term x in equations of the responsivity represents voltage signal from a heat flux gauge; unit of [mV].

This publication is available free of charge from: https://doi.org/10.6028/NIST.TN.2083r1

C Modeling the Methanol Pool Fire using the Fire Dynamics Simulator (FDS)

A simulation of the 1 m methanol pool fire is conducted using FDS 6.7.5 to (1) estimate the local mean gas velocity used in the Nusselt number correlation for convective heat loss from the thermocouple bead and (2) verify the in-house MATALB algorithm for determination of the thermal inertia correction described in *Section D.3*. FDS has been validated for simulation of local velocity in a fire from a variety of previous experiments [20]. The difference between the FDS velocity calculation and McCaffrey's pool fire plume velocity measurements is on-average about 3.5 % [20].

In this section, numerical details of the FDS simulation are described and numerical results are provided and compared with the experimental measurements. Appendix Section C.1 presents the numerical details, including the mesh size and computational interrogation locations, which are set to match the experimental measurement positions. Appendix Section C.2 presents the FDS simulated gas velocity results, which are used to calculate the Nusselt number as part of the convective term used in the energy balance at the thermocouple bead (see Eq. 3). The calculated gas velocity profile along the centerline is compared to the Baum and MaCaffrey's plume theory. Appendix Section C.3 presents the FDS simulated gas temperature results. The gas temperature profile along the centerline is compared with the experimental results to validate the FDS simulation. Appendix Section C.4 presents the simulated heat release rate and radiative fraction.

C.1 FDS Simulation Set-up

The FDS input file for the 1 m methanol fire is based on the input file for this case in the FDS Validation Manual [20]. The calculation imposes the measured mass burning rate of 12.8 g/s ± 0.9 g/s as an input parameter and the methanol pool burner is modeled with a 1 cm lip height. The radiative fraction is set to its measured value (= 0.22) and the soot yield is set to 0. The ambient air temperature is taken as the average lab temperature during the experiment, which is equal to 298 K. The chemistry is approximated as two steps as described in the FDS Technical Reference Manual [37]. The input file is reproduced in *Appendix H*. The velocity and temperature simulation results are saved at 1.7 kHz, while the heat release rate and radiative fraction are saved at 1 Hz. This very fast sampling rate reduces the uncertainty in evaluating the rapidly changing inertia term in Eq. 5 as part of the MATLAB algorithm used to correct the measured thermocouple temperature to determine the gas temperature.

Figure C1 shows the FDS simulation mesh and thermocouple locations which are set to the experimental measurement positions. The grid spacing was set to 1 cm in the input file. The thermocouples are located every 10 cm, from 0 cm to 50 cm in the radial direction, and every 5 cm to 10 cm in the axial direction from 1 cm to 210 cm above the burner. The total number of measurement points was 138. The bead temperature in the FDS simulation was obtained by applying a thermocouple device object. The thermocouple device parameters specified in the FDS simulation are set to mimic the experiment in terms of thermophysical properties of the Type S thermocouple and the actual bead diameter. Appendix H provides code lines of the FDS input file, including the numerical details such as combustion, radiation, species, initial & boundary conditions, and outputs. Here, OBST lines for the geometry of the pool burner are excluded, which is the same as the input file for this case in the FDS Validation Manual [20].

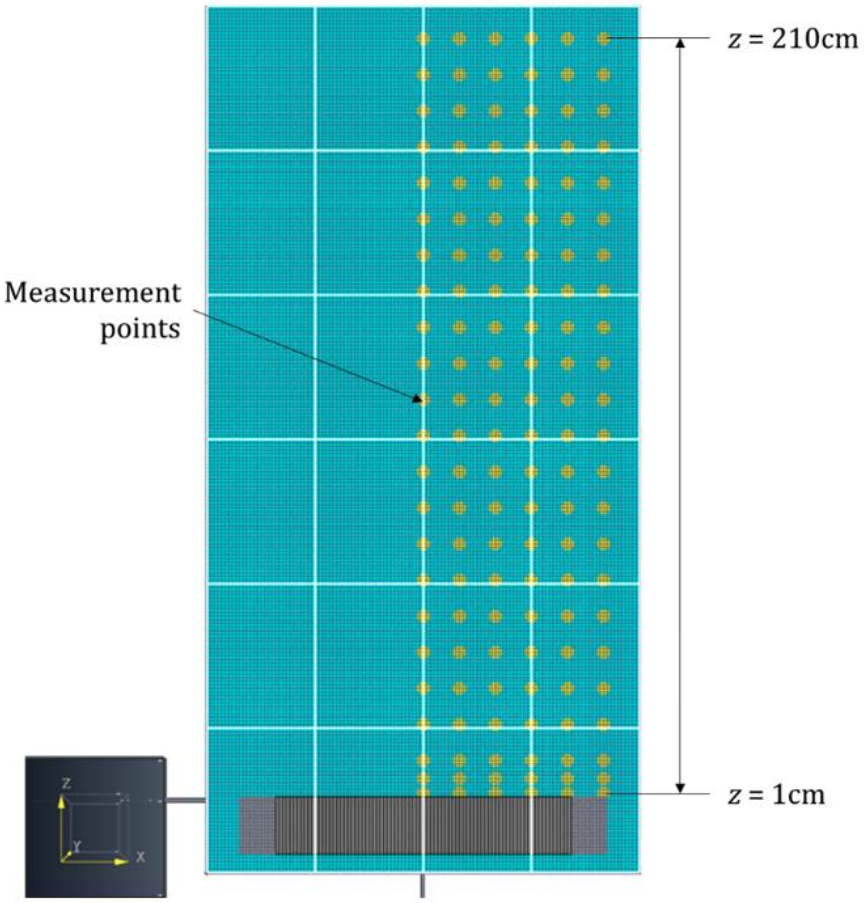

Figure C1. Mesh and thermocouple temperature measurement locations in a plane through the pool centerline, where z is distance above the burner.

C.2 Simulated Gas Velocity

The simulated gas velocity profile along the centerline is compared with the maximum velocity calculated by Baum and McCaffrey's plume theory [25]. The distribution of the gas velocity on the plane across the burner center is plotted and listed in Table C1. The gas velocity results are used to calculate the corrected gas temperature in *Section 2.1*.

Baum and McCaffrey [25] developed a theoretical plume correlation based on kinematic relationships between the velocity, vorticity, and heat release field in an isolated fire plume with length scales non-dimensionalized by D^* and velocity non-dimensionalized by $\sqrt{gD^*}$. Here, D^* is the plume scaling involving the heat release rate, defined by $(\dot{Q}/(\rho_o c_p T_o \sqrt{g}))^{2/5}$, where $\dot{Q}$ is the ideal heat release rate, and ρ_o and c_p are the density and specific heat of air, respectively, at ambient temperature (T_o). The dimensionless upstream gas velocity along the centerline is then defined as:

$$\frac{V_g}{\sqrt{gD^*}} = A\left(\frac{z}{D^*}\right)^n \tag{C1}$$

This publication is available free of charge from: https://doi.org/10.6028/NIST.TN.2083r1

In Eq. C1, the quantities n and A are distinct for the three plume regions (the flame, intermittent and plume regions), which are defined by the range of z/D^*. Details of the plume correlation and the distinct plume regions are described in Ref. [25]. Figure C2 shows the mean gas velocity obtained from the FDS simulation as a function of the axial distance above the burner compared with Baum and McCaffrey's plume theory (solid line). The FDS simulation results underpredict the plume theory by about 18 % on-average. The maximum centerline velocities of the FDS velocity calculation and plume theory are 5.37 m/s and 5.71 m/s, respectively. On the other hand, the velocity profile for each of the distinct plume regions follows the trends of Baum and McCaffery's plume theory.[1]

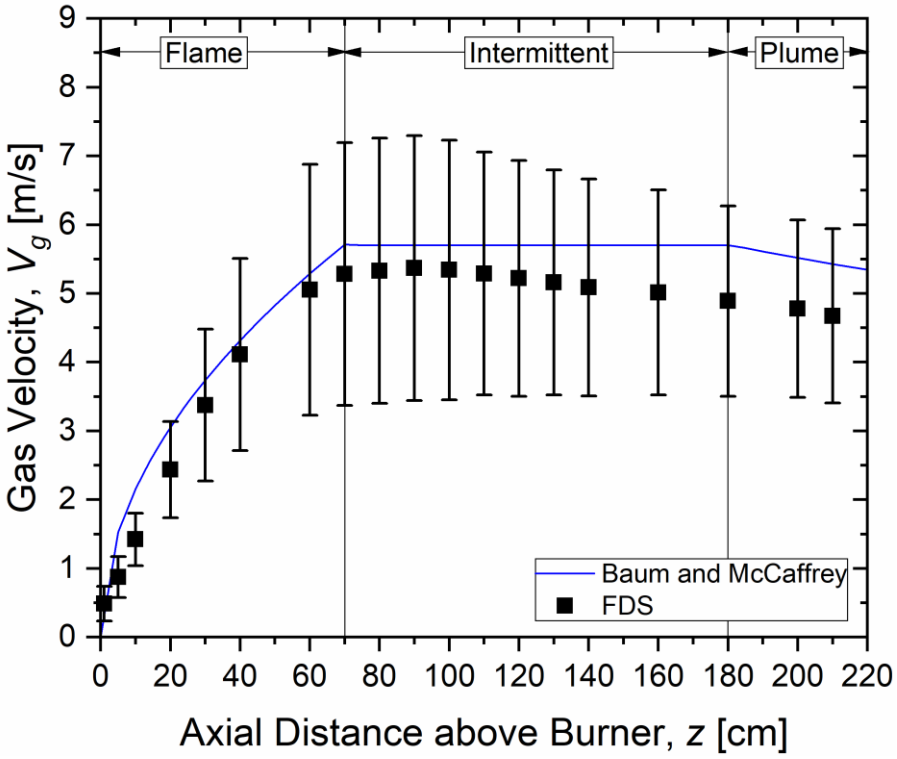

Figure C2. Mean and standard deviation of centerline gas velocity obtained from the FDS simulation as a function of the axial distance above the burner. The blue line represents the mean gas velocity calculated using the plume theory suggested by Baum and McCaffrey [25].

Figure C3 shows the simulated gas velocity distribution in the plane across the centerline above the burner. The mean, standard deviation and expanded combined uncertainty of the simulated gas velocity are presented in Table C1 for all 138 locations where the thermocouple temperature was measured. The gas velocity results were used to calculate the corrected gas temperature in *Section 2.1*.

[1] The velocity was not measured as part of this experimental campaign.

This publication is available free of charge from: https://doi.org/10.6028/NIST.TN.2083r1

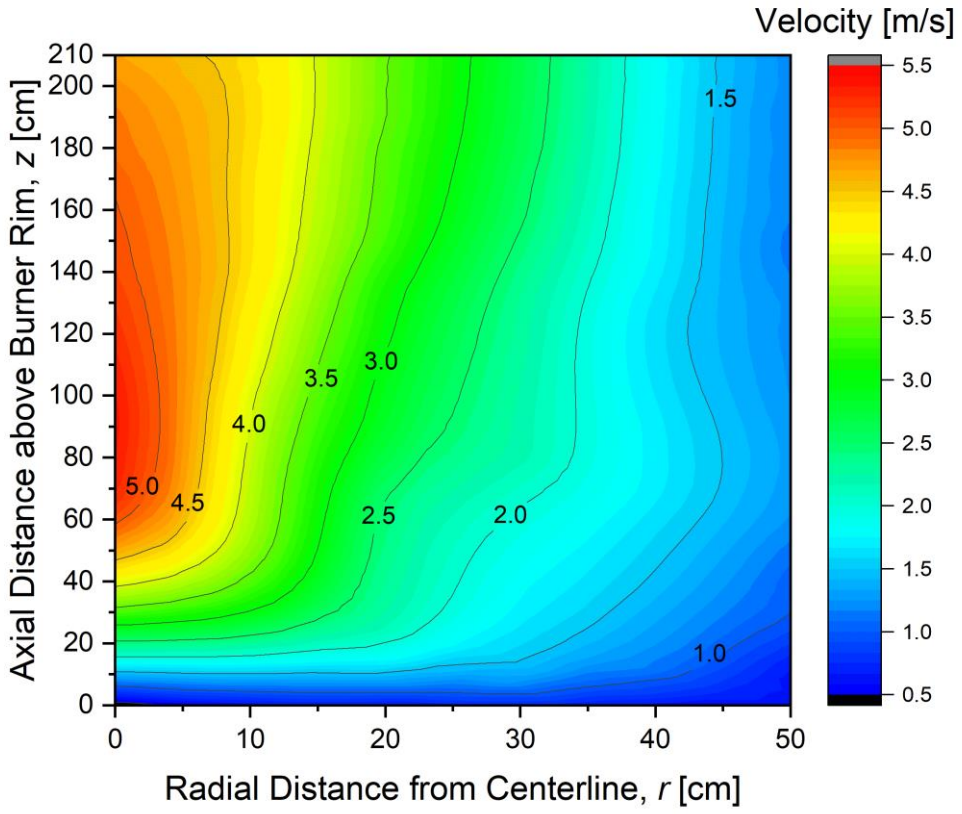

Figure C3. The simulated gas velocity distribution above the burner.

Table C1. The simulated mean ($\overline{V}_g$) and standard deviation (σ_{V_g}) of the gas velocity at all 138 thermocouple temperature measurement locations.

z [cm]	r [cm]	$\overline{V}_g$ [m/s]	σ_{V_g} [m/s]	z [cm]	r [cm]	$\overline{V}_g$ [m/s]	σ_{V_g} [m/s]	z [cm]	r [cm]	$\overline{V}_g$ [m/s]	σ_{V_g} [m/s]
1	0	0.49	0.25	1	20	0.70	0.31	1	40	0.63	0.27
5	0	0.87	0.30	5	20	1.08	0.41	5	40	0.95	0.30
10	0	1.42	0.38	10	20	1.51	0.63	10	40	1.11	0.45
20	0	2.44	0.70	20	20	2.03	0.99	20	40	1.25	0.71
30	0	3.37	1.11	30	20	2.25	1.18	30	40	1.36	0.84
40	0	4.11	1.40	40	20	2.31	1.15	40	40	1.47	0.90
50	0	4.65	1.62	50	20	2.39	1.14	50	40	1.55	0.97
60	0	5.05	1.82	60	20	2.43	1.10	60	40	1.62	0.99
70	0	5.28	1.91	70	20	2.53	1.10	70	40	1.71	0.95
80	0	5.33	1.93	80	20	2.69	1.13	80	40	1.70	0.89
90	0	5.37	1.93	90	20	2.83	1.17	90	40	1.71	0.94
100	0	5.34	1.89	100	20	2.89	1.21	100	40	1.65	0.89
110	0	5.29	1.77	110	20	2.96	1.23	110	40	1.63	0.83

----- Table C1 Continued on Next Page -----

This publication is available free of charge from: https://doi.org/10.6028/NIST.TN.2083r1

z [cm]	r [cm]	$\overline{V}_g$ [m/s]	σ_{V_g} [m/s]	z [cm]	r [cm]	$\overline{V}_g$ [m/s]	σ_{V_g} [m/s]	z [cm]	r [cm]	$\overline{V}_g$ [m/s]	σ_{V_g} [m/s]
120	0	5.22	1.72	120	20	3.05	1.25	120	40	1.61	0.87
130	0	5.16	1.64	130	20	3.09	1.21	130	40	1.63	0.83
140	0	5.09	1.58	140	20	3.20	1.21	140	40	1.71	0.89
150	0	5.06	1.51	150	20	3.34	1.19	150	40	1.74	1.01
160	0	5.02	1.49	160	20	3.39	1.14	160	40	1.73	1.05
170	0	4.97	1.42	170	20	3.42	1.15	170	40	1.77	1.04
180	0	4.89	1.39	180	20	3.44	1.16	180	40	1.79	1.02
190	0	4.86	1.35	190	20	3.51	1.15	190	40	1.79	0.94
200	0	4.78	1.29	200	20	3.50	1.15	200	40	1.81	0.94
210	0	4.67	1.27	210	20	3.52	1.15	210	40	1.81	0.99
1	10	0.69	0.32	1	30	0.78	0.32	1	50	0.65	0.31
5	10	1.04	0.38	5	30	1.15	0.40	5	50	0.65	0.21
10	10	1.49	0.50	10	30	1.41	0.56	10	50	0.62	0.22
20	10	2.33	0.83	20	30	1.59	0.87	20	50	0.84	0.40
30	10	3.01	1.23	30	30	1.71	1.05	30	50	1.01	0.64
40	10	3.42	1.51	40	30	1.78	1.08	40	50	1.03	0.72
50	10	3.71	1.64	50	30	1.87	1.05	50	50	1.13	0.74
60	10	3.82	1.70	60	30	1.96	1.04	60	50	1.24	0.79
70	10	3.87	1.67	70	30	2.07	1.00	70	50	1.29	0.77
80	10	3.91	1.67	80	30	2.21	1.00	80	50	1.30	0.80
90	10	3.99	1.66	90	30	2.21	1.06	90	50	1.28	0.84
100	10	4.03	1.68	100	30	2.24	1.06	100	50	1.24	0.83
110	10	4.17	1.65	110	30	2.27	1.12	110	50	1.23	0.85
120	10	4.21	1.60	120	30	2.30	1.11	120	50	1.21	0.79
130	10	4.28	1.58	130	30	2.32	1.08	130	50	1.23	0.75
140	10	4.36	1.52	140	30	2.39	1.08	140	50	1.16	0.72
150	10	4.37	1.50	150	30	2.47	1.14	150	50	1.12	0.71
160	10	4.36	1.47	160	30	2.55	1.12	160	50	1.19	0.73
170	10	4.37	1.42	170	30	2.58	1.10	170	50	1.16	0.76
180	10	4.39	1.39	180	30	2.64	1.12	180	50	1.19	0.78
190	10	4.41	1.39	190	30	2.67	1.11	190	50	1.16	0.77
200	10	4.40	1.37	200	30	2.69	1.12	200	50	1.21	0.78
210	10	4.37	1.31	210	30	2.70	1.10	210	50	1.19	0.78

C.3 Simulated Gas Temperature

Figure C4 shows the mean and standard deviation of the simulated gas temperature along the centerline is compared with the experimental results (see Figure 18 and Figure 19) as a function of axial distance above the burner. The average difference between the FDS and experimentally determined in the mean and standard deviation of the gas temperature are 4 % and 17 % on average, respectively, where the

difference is defined as $100\left(|T_{g,FDS} - T_{g,EXP}|\right)/T_{g,EXP}$. In general, the simulated results agree with the experimental results within measurement uncertainty.

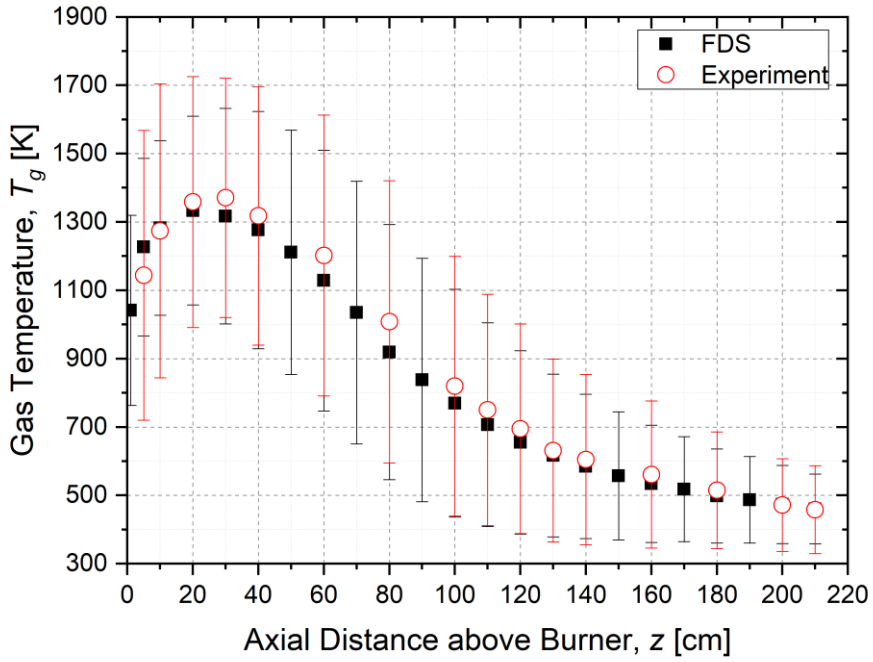

Figure C4. The simulated mean and standard deviation of the gas temperature compared with the experimental results as a function of axial distance above the burner.

Figure C5 shows the simulated gas temperature distribution in the plane across the centerline above the burner. The mean, standard deviation and expanded combined uncertainty of the gas temperature are presented in Table C2.

This publication is available free of charge from: https://doi.org/10.6028/NIST.TN.2083r1

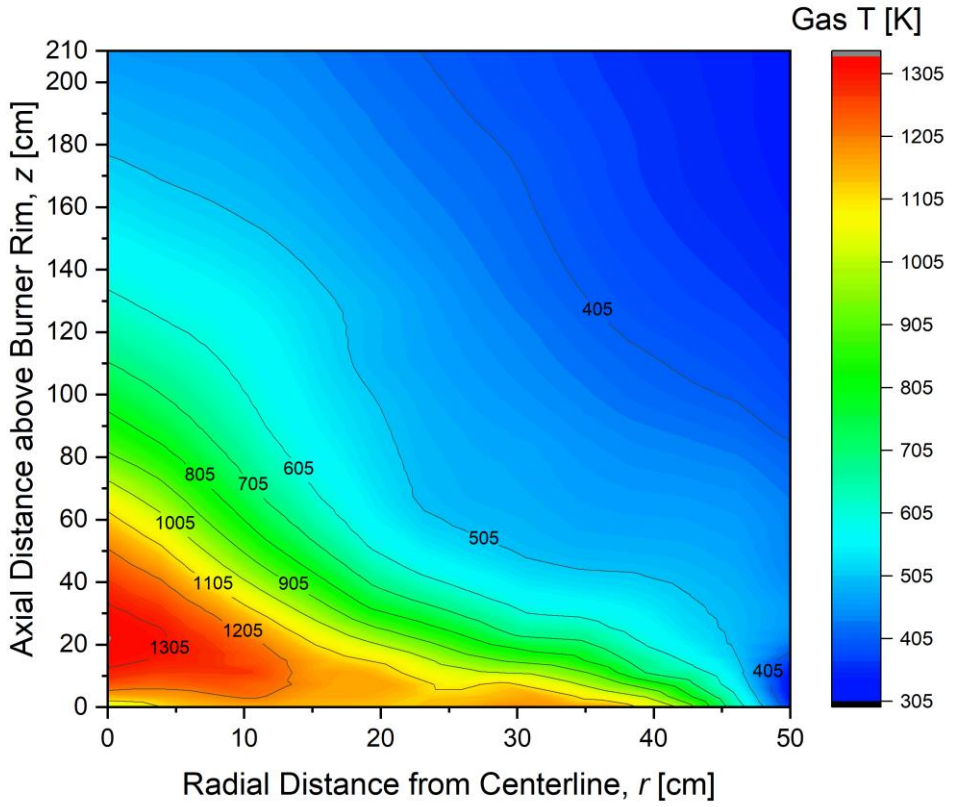

Figure C5. The simulated gas temperature distribution above the burner.

Table C2. The simulated mean ($\overline{T}_g$) and standard deviation (σ_g) of the gas temperature at all 138 thermocouple temperature measurement locations.

z [cm]	r [cm]	$\overline{T}_g$ [K]	σ_{T_g} [K]	z [cm]	r [cm]	$\overline{T}_g$ [K]	σ_{T_g} [K]	z [cm]	r [cm]	$\overline{T}_g$ [K]	σ_{T_g} [K]
1	0	1041	278	1	20	1115	327	1	40	1117	300
5	0	1226	260	5	20	1196	338	5	40	899	466
10	0	1282	255	10	20	1168	402	10	40	689	472
20	0	1333	276	20	20	1010	478	20	40	585	446
30	0	1317	316	30	20	803	461	30	40	544	409
40	0	1276	347	40	20	678	408	40	40	513	372
50	0	1211	357	50	20	593	356	50	40	483	328
60	0	1129	381	60	20	544	307	60	40	471	286
70	0	1035	384	70	20	527	284	70	40	458	235
80	0	919	373	80	20	516	257	80	40	444	198
90	0	838	356	90	20	508	240	90	40	433	182
100	0	770	333	100	20	502	223	100	40	414	147
110	0	707	298	110	20	486	204	110	40	409	135

----- Table C2 Continued on Next Page -----

This publication is available free of charge from: https://doi.org/10.6028/NIST.TN.2083r1

z [cm]	r [cm]	$\overline{T}_g$ [K]	σ_{T_g} [K]	z [cm]	r [cm]	$\overline{T}_g$ [K]	σ_{T_g} [K]	z [cm]	r [cm]	$\overline{T}_g$ [K]	σ_{T_g} [K]
120	0	655	268	120	20	487	191	120	40	395	119
130	0	617	238	130	20	487	181	130	40	385	109
140	0	585	211	140	20	473	168	140	40	381	105
150	0	557	188	150	20	462	151	150	40	374	100
160	0	534	172	160	20	451	135	160	40	369	90
170	0	518	154	170	20	443	122	170	40	365	86
180	0	498	138	180	20	434	109	180	40	365	86
190	0	487	127	190	20	428	102	190	40	363	80
200	0	473	114	200	20	420	95	200	40	359	74
210	0	460	102	210	20	414	89	210	40	356	64
1	10	1145	311	1	30	1159	316	1	50	353	89
5	10	1271	312	5	30	1232	402	5	50	310	47
10	10	1279	317	10	30	1024	468	10	50	322	113
20	10	1236	340	20	30	744	492	20	50	434	340
30	10	1143	387	30	30	612	437	30	50	464	359
40	10	1010	400	40	30	542	380	40	50	445	337
50	10	895	386	50	30	501	322	50	50	438	302
60	10	798	375	60	30	490	290	60	50	439	294
70	10	725	355	70	30	478	245	70	50	427	250
80	10	672	336	80	30	478	227	80	50	414	198
90	10	634	308	90	30	465	212	90	50	395	155
100	10	606	286	100	30	455	196	100	50	382	136
110	10	587	264	110	30	445	180	110	50	372	125
120	10	571	247	120	30	439	164	120	50	366	106
130	10	552	222	130	30	428	155	130	50	355	91
140	10	533	197	140	30	421	141	140	50	349	88
150	10	516	176	150	30	416	129	150	50	345	75
160	10	500	158	160	30	410	120	160	50	339	63
170	10	487	142	170	30	406	113	170	50	336	60
180	10	476	130	180	30	402	105	180	50	334	54
190	10	466	123	190	30	393	93	190	50	331	54
200	10	457	115	200	30	388	84	200	50	333	54
210	10	449	104	210	30	385	77	210	50	335	53

C.4 Simulated Heat Release Rate and Radiative Fraction

Figure C6 shows the heat release rate and mass burning rate results from the FDS simulation as a function of the simulation time. The simulation took several seconds to reach steady burning and the simulated results are averaged in the steady burning period from 5 s to 18 s. The mass burning rate and radiative fraction are prescribed and set to match the measured values of 12.8 g/s and 0.22, respectively, in the experiment. In the simulation, this yields 269 kW for the simulated heat release rate. This is in

approximate agreement with the heat release rate measured by calorimetry, which is 256 kW ± 45 kW, as discussed in *Section 3.3* of this report.

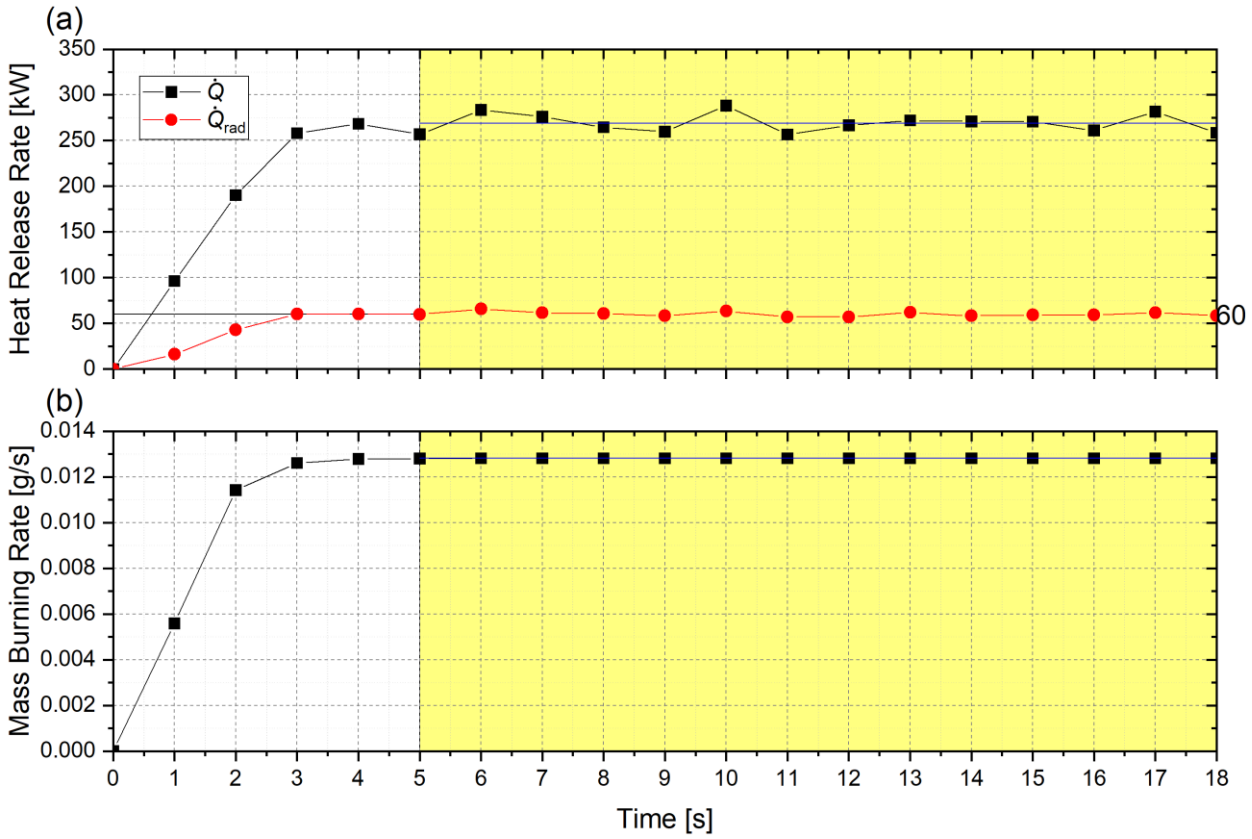

Figure C6. Heat Release rate, mass burning rate and radiative fraction in the FDS simulation as a function of the time. The experimental mass burning rate of 12.8 g/s is prescribed and the radiative fraction is set to 0.22 in the simulation.

This publication is available free of charge from: https://doi.org/10.6028/NIST.TN.2083r1

D Temperature Correction

In *Section 3.7*, an in-house MATLAB code is described, which was developed to solve the energy balance at the thermocouple bead (Eq. 5 in *Section 2.1.2*) in order to determine the gas temperature, $T_g(t)$, from the measured thermocouple bead temperature, $T_b(t)$. The time derivative of the thermocouple bead temperature (dT_b/dt) is calculated using a polynomial fit of several data points in the time series to determine the thermal inertia correction term and the corrected gas temperature, $T_g(t)$.

Appendix D.1 evaluates the calculation of the thermal inertia correction by the MATLAB Code by applying the code to a sinusoidal temperature function and comparing the results to the analytic result. Appendix D.2 presents a parametric study conducted to determine the best fitting method to calculate dT_b/dt. In Appendix D.3, a FDS simulation is used to evaluate the MATLAB code and determine its uncertainty.

D.1 MATLAB Code Verification

Assuming that a measured temperature (T) fluctuates in a sinusoidal wave defined as:

$$T = \overline{T} + A\sin(\omega t) \tag{D1}$$

where A is the amplitude of the temperature fluctuation and ω is the angular frequency defined as $\omega = 2\pi f$; f is the wave frequency. The thermal inertia correction temperature (T_{the}) is defined as:

$$T_{the} = T + \tau\frac{dT}{dt} \tag{D2}$$

Assuming a thermocouple bead shape is spherical, the thermocouple time constant (τ) can be expressed as:

$$\tau = \frac{\rho_b c_{p,b} d_b^2}{6\mathrm{Nu}\lambda_g} \tag{D3}$$

where d_b and V_g are 153.3 µm and 2 m/s, respectively. The temperature-dependent gas properties for Re and Pr, are taken as those of air [17], and the temperature dependent emissivity and the thermophysical properties of platinum were taken from [18, 19]; which are listed in *Appendix A*. Substituting Eq. D2 in Eq. D1,

$$T_{the} = \overline{T} + A\sin(\omega t) + \tau \cdot A\omega\cos(\omega t) \tag{D4}$$

Substituting Eq. D5 in Eq. D4:

$$a\sin x + b\cos x = \sqrt{a^2 + b^2}\,\sin(x + \alpha), \qquad \alpha = \tan^{-1}\left(\frac{b}{a}\right) \tag{D5}$$

Eq. D2 is rearranged as:

$$T_{the} = \overline{T} + A\sqrt{1 + (\omega\tau)^2}\sin(\omega t + \phi) \tag{D6}$$

This publication is available free of charge from: https://doi.org/10.6028/NIST.TN.2083r1

where ϕ denotes the phase angle, $\phi = \tan^{-1}(\omega\tau)$, which converges to π/2 as $\omega\tau$ becomes very large. Thus, the phase difference between the original and corrected temperature increases if either or both the fluctuation frequency and the time constant become very larger.

The thermal inertia temperature correction calculated with the in-house MATLAB code is compared with the exact solution described by Eq. D6. The uncorrected (raw or bead) temperature is assumed to have a sinusoidal form based on Eq. D1 as:

$$T = 300\ \sin(100\pi t) + 1300 \tag{D7}$$

The amplitude of the fluctuating temperature is set to 300 K and the wave frequency to 50 Hz. The mean temperature ($\overline{T}$) is set to 1300 K. The exact solution of the corrected temperature (T_{the}) can be expressed as:

$$T_{the} = 300\sqrt{1 + (100\pi \cdot \tau)^2}\ \sin(100\pi t + \phi) + 1300, \quad \phi = \tan^{-1}(100\pi \cdot \tau) \tag{D8}$$

In the MATLAB code, dT/dt is calculated using a polynomial curve-fitting function. The fit parameters, such as fit order and fit window size, can affect the temperature correction. Tagawa and Ohta [38] conducted a parametric study investigating the sensitivity of the calculated thermal inertia temperature correction on the fitting parameter. The results showed that selection of the fitting parameters has a negligible effect when the polynomial fit order is 2 and the fit window size is determined by 11 data points. The fitting parameters are determined from the dominant frequencies in the temperature fluctuations and the data sampling frequency. The gradient, dT/dt, is calculated using a second order polynomial fit of three consecutive data points in the temperature time series. An extremely high sampling frequency is used (25 kHz) with a fit window of 0.1 ms. Figure D1 shows the thermal inertia corrected temperature calculated by the in-house MATLAB code as a function of time, compared with the exact solution. The calculated results agree with the exact solution to within 0.001 % as seen in Figure D1.

D.2 Optimizing Fit Parameters for Calculation of the Corrected Gas Temperature

In this section, the effect of the fit parameters on the calculation of the corrected gas temperature using the in-house MATLAB code (see *Section 3.7* and *Appendix D.1*) is estimated. The focus of this section is to verify that the polynomial curve fitting method for dT_b/dt is appropriate. The uncorrected thermocouple bead temperature is assumed to be an arbitrary sinusoidal function:

$$T_b = 300\sin(2\pi f t) + 1300 \tag{D9}$$

where f is the assumed frequency of the fluctuating bead temperature (T_b) and t represents time.

A parametric study is conducted varying the frequency (f), sampling frequency (f_s) and fit window size (t_w) over the range of values presented in Table D1. The fit window size is defined as:

$$t_w = 2n_p \times \left(\frac{1}{f_s}\right) \tag{D10}$$

This publication is available free of charge from: https://doi.org/10.6028/NIST.TN.2083r1

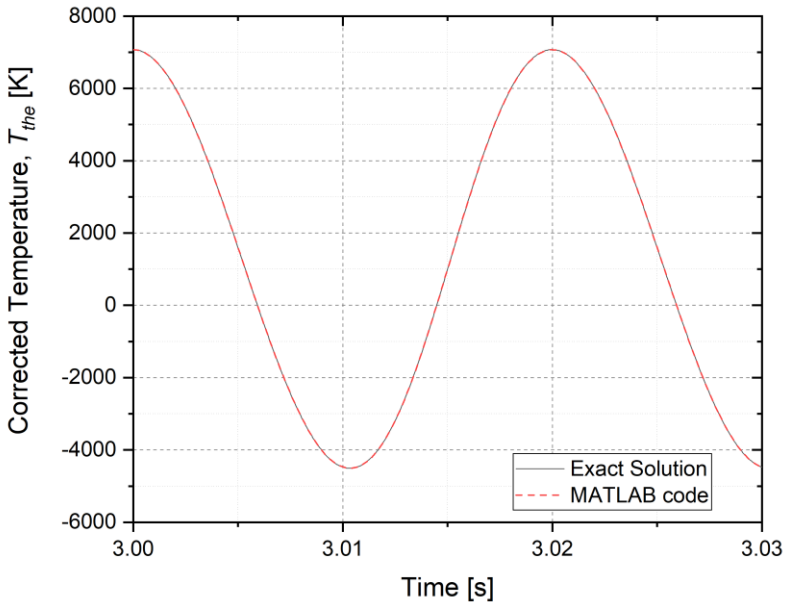

Figure D1. Comparison of the thermal inertia corrected temperature calculated by the in-house MATLAB code with the exact solution.

where n_p is the number of data points in half of the fit window. A second order polynomial curve-fitting function is used to fit the bead temperature (T_b) as a function of time (as seen in Figure D2) for different characteristic bead temperature frequencies, varying from 2 Hz to 50 Hz, sampled at a frequency of 1 kHz, which is fast enough to resolve the function in this verification study.

Table D1. Fit parameters of polynomial curve fit for dT/dt used in the parametric study.

Parameter	Cases
Frequency, f [Hz]	2, 10, 20, 50
Sampling Frequency, f_s [kHz]	1, 2, 5, 10, 25
Number of data points in half of the fit window, n_p [-]	1, 5, 10

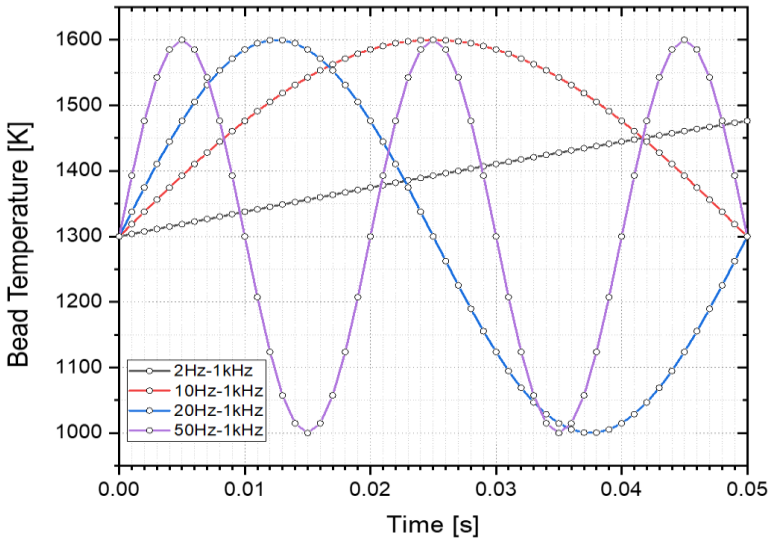

Figure D2. The bead temperature as a function of time for different characteristic bead temperature frequencies (f) at a sampling frequency (f_s) of 1 kHz; the symbols indicate the simulated data points.

The gas temperature corrected for thermal inertia and radiative loss was calculated using the in-house MATLAB code, considering an energy balance at the thermocouple bead. Figure D3 shows the gas temperature as a function of time for a simulated bead temperature frequency, f, equal to 50 Hz for various sampling frequencies (f_s = 1 kHz to 25 kHz) and fit windows (n_p = 1 to 10). The deviation of the corrected gas temperature from the exact solution increases as the fit window (or n_p) increases. The amplitude of the fluctuating gas temperature becomes smaller as the fit window increases. This is because the term dT/dt in Eq. D2 becomes smoother as more data points are used for curve-fitting. The smoothing effect can dominate the results especially near the temperature extremes when the gradient is rapidly changing. The results show that the smoothing effect is related to the window size of the fit and the dominant frequency of the fluctuating temperature. To estimate the magnitude of the smoothing effect, the mean error of the gas temperature is determined as a function of a parameter denoted as γ_t, the ratio of the fit window size (t_w) to the wave period (t_p), which is defined as:

$$\gamma_t = \frac{t_w}{t_p} = \frac{2n_p \times f}{f_s} \tag{D11}$$

Here, t_p is the wave period, which is the inverse of the characteristic frequency ($= 1/f$) of the bead temperature. The results are presented in Table D2, which show that the mean error in the calculated gas temperature, T_g, increases with γ_t. For γ_t less than 0.05, the mean error in T_g is less than 1 % as seen in Table D2. To minimize over-smoothing, the fit window size must be reduced or the instrument sampling frequency must be increased.

This publication is available free of charge from: https://doi.org/10.6028/NIST.TN.2083r1

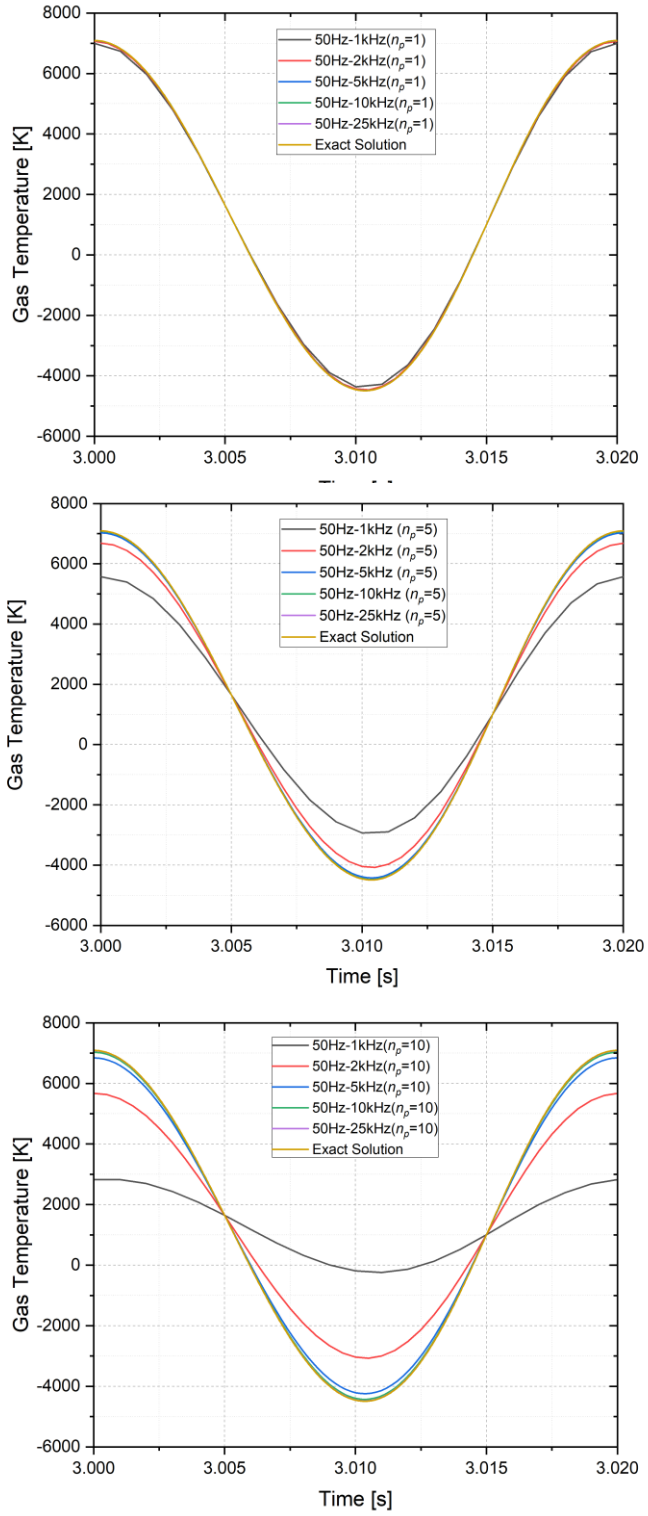

Figure D3. Exact solution compared to the in-house MATLAB gas temperature calculation as a function of time for f = 50 Hz; (a) n_p = 1, (b) n_p = 5, (c) n_p = 10.

This publication is available free of charge from: https://doi.org/10.6028/NIST.TN.2083r1

Table D2. Mean error of the gas temperature as a function of the ratio of the fit window size to the wave period ($= \gamma_t$).

f [Hz]	f_s [kHz]	n_p [-]	t_w [ms]	t_p [ms]	γ_t [-]	Error [%]
2	1	1	2	500	0.004	4.5E-05 %
50	25	1	0.08	20	0.004	1.3E-03 %
50	10	1	0.2	20	0.01	1.5E-02 %
2	1	5	10	500	0.02	5.5E-03 %
50	5	1	0.4	20	0.02	0.1 %
50	25	5	0.4	20	0.02	0.1 %
10	1	1	2	100	0.02	1.2 %
2	1	10	20	500	0.04	0.0 %
50	25	10	0.8	20	0.04	0.4 %
20	1	1	2	50	0.04	0.7 %
50	2	1	1	20	0.05	0.4 %
50	10	5	1	20	0.05	0.4 %
50	10	10	2	20	0.1	2 %
50	5	5	2	20	0.1	2 %
50	1	1	2	20	0.1	3 %
10	1	5	10	100	0.1	7 %
50	5	10	4	20	0.2	6 %
10	1	10	20	100	0.2	10 %
20	1	5	10	50	0.2	17 %
50	2	5	5	20	0.25	15 %
20	1	10	20	50	0.4	59 %
50	2	10	10	20	0.5	52 %
50	1	5	10	20	0.5	53 %
50	1	10	20	20	1.0	147 %

Figure D4 shows the fast Fourier power spectrum of the time series thermocouple bead temperature at four axial measurement positions (z = 10 cm, 60 cm, 120 cm and 210 cm) along the centerline. Figure D5 is based on results like those in Figure D4 and shows the dominant frequency of the time series of the thermocouple bead temperature as a function of axial distance above the burner along the centerline. The mean and standard deviation of the dominant frequency measured along the centerline are 1.39 Hz ± 0.013 Hz, which is consistent with the pool fire frequency of 1.37 Hz, estimated in *Section 3.4*. The results show that changes in the thermocouple temperature correspond to the dominant flame pulsation at all fire locations.

In this study, the data acquisition system (DAQ) sampling frequency is 60 Hz and the MATLAB calculation uses a fit window size, t_w, set to 33.3 ms with n_p = 1. The parameter γ_t for the dominant frequency is 0.046, using Eq. D11. The mean error is approximately 0.4 % as seen in Table D2. Thus, the current fit windows size of 33 ms is suitable to correct the temperature measurements with the sampling

frequency of 60 Hz, considering the dominant frequency of the time series thermocouple bead temperature of 1.39 Hz. However, the power spectrum of the time series thermocouple bead temperature has a wide band of frequencies as seen in Figure D4, so it is challenging to estimate the uncertainty in the determination of the time derivative of the bead temperature ($u_c(dT_b/dt)$), considering only a frequency analysis. Instead, the uncertainty, $u_c(dT_b/dt)$, is estimated using a FDS simulation as described in *Appendix D.3*.

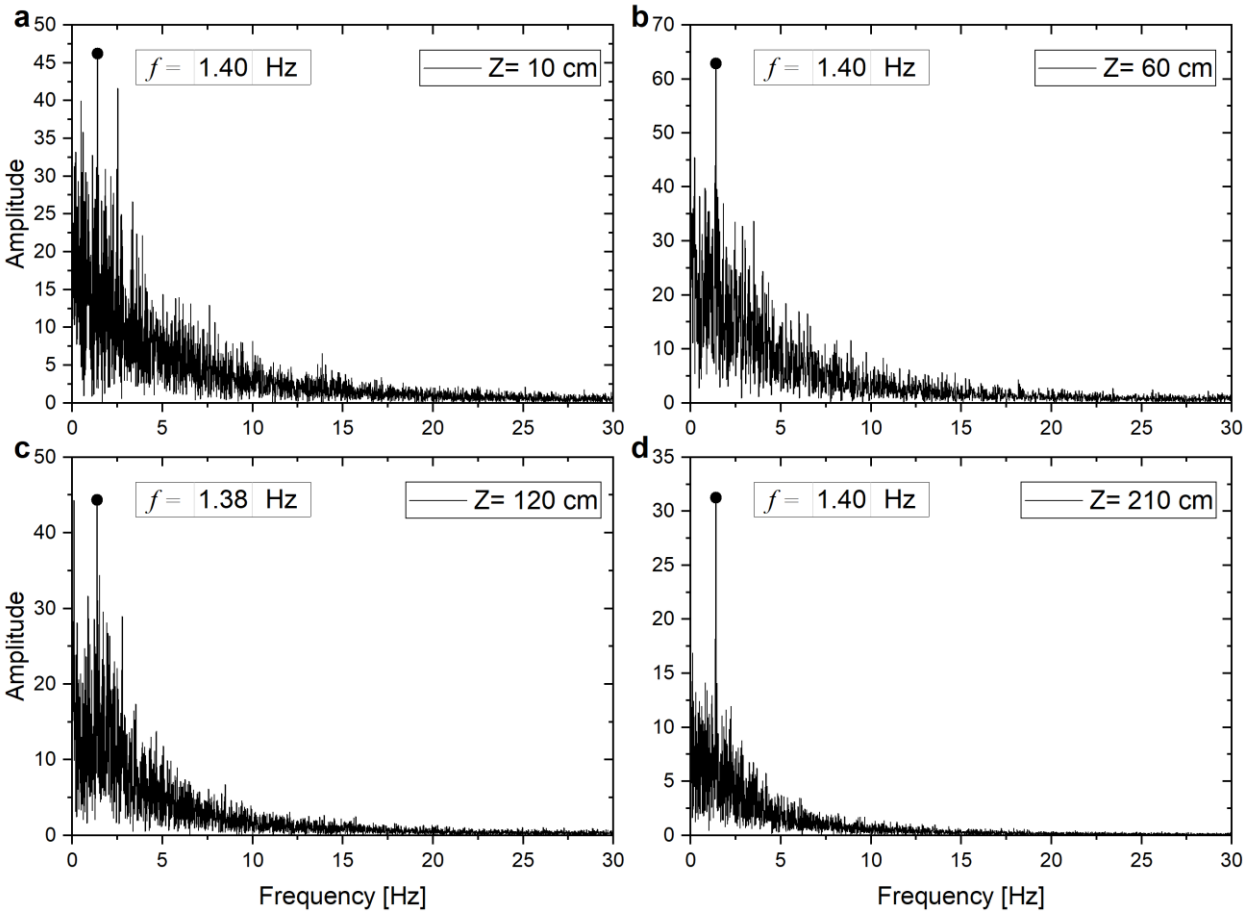

Figure D4. Fast Fourier power spectrum of the time series of the thermocouple bead temperature along the centerline; (a) at z = 10 cm (Exp. 03/11, Repeat no. 1), (b) at z = 60 cm (Exp. 03/26, Repeat no. 1), (c) at z = 120 cm (Exp. 03/11, Repeat no. 1) and (d) at z = 210 cm (Exp. 03/11, Repeat no.1). The dominant frequency of the bead temperature measurement at each position is noted.

This publication is available free of charge from: https://doi.org/10.6028/NIST.TN.2083r1

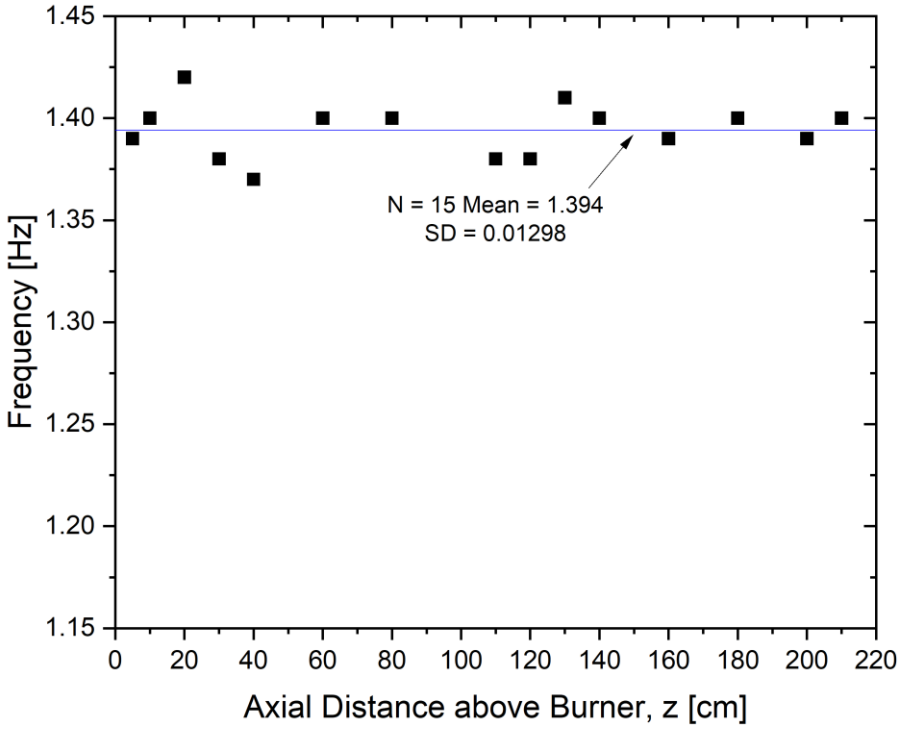

Figure D5. Dominant frequency of the time series of the thermocouple bead temperature as a function of axial distance above the burner along the centerline. The mean and standard deviation of the dominant frequency are 1.39 Hz ± 0.013 Hz.

D.3 Evaluation of the Gas Temperature MATLAB Calculation using FDS

In this section, a FDS simulation is used to evaluate the efficacy and test the limitations of the MATLAB code gas temperature determination. FDS is used to simulate the gas and thermocouple bead temperatures. FDS [6] calculates the gas temperature. The thermocouple bead temperature is calculated by FDS, assuming a spherical bead using Eq. 5 of this report. The FDS default values for bead emissivity, density, and temperature dependent thermophysical properties are modified to match the S type thermocouple as used in the experiment. Preliminary comparisons showed that the FDS bead temperature and the experimentally measured values are similar, lending confidence in using this method. Here, the simulated FDS thermocouple bead temperature is taken as input for the MATLAB code. Then, the MATLAB code is used to calculate the gas temperature, which is compared with the gas temperature from the FDS simulation. This approach provides a way to estimate the error in the calculated gas temperature introduced through use of the MATLAB code. An alternative approach to determine the uncertainty using a propagation of error analysis of Eqs. E1 - E4 led to non-physical and unreasonably large temperature values.

The input parameters in the FDS simulation and the MATLAB code were set to match each other. Appendix H lists the FDS input file, which was taken from the FDS Validation Guide calculation of the 1 m methanol pool fire considered here. The bead diameter (d_b) is taken as 153.3 µm. For thermocouple input parameters in FDS, thermophysical properties of the thermocouple bead, such as emissivity, specific heat and density, are taken from Table A2, using the measured temperatures from the experiments and

assuming that the thermocouples are purely platinum. The Reynolds number for the thermocouple bead is calculated using the local mean gas velocity obtained from the FDS simulation presented in Table D1. In the MATLAB code, the value of dT_b/dt is calculated using a second order polynomial fit considering three consecutive data points in the temperature time series. The data saving frequency (f_s) in the FDS simulation is set to 1.4 kHz and the fit window size (t_w) is set to 1.4 ms.

Figure D6 shows the mean and standard deviation of the gas temperature as a function of the axial distance above the burner along the centerline obtained in the FDS simulation $(T_{g,FDS})$ and calculated by the MATLAB code $(T_{g,MAT})$. The difference in the mean and standard deviation of $T_{g,MAT}$ as compared to the FDS simulation results are presented in Table D3. The deviation of $\overline{T}_{g,MAT}$ along the centerline as compared to $T_{g,FDS}$ is 27 K (or 3 %) on-average and is always less than 50 K (or 5 %). The difference in the standard deviation of $\sigma_{T_{g,MAT}}$ is 15 K (or 8 %) on average and always less then 36 K (or 14 %). These differences are considered an estimate of the uncertainty in the determination of the time derivative of the bead temperature in the MATLAB code. This result, combined with other uncertainty sources, is used in to estimate the total uncertainty of the experimental value of T_g and σ_{T_g} as discussed in *Section E.1*.

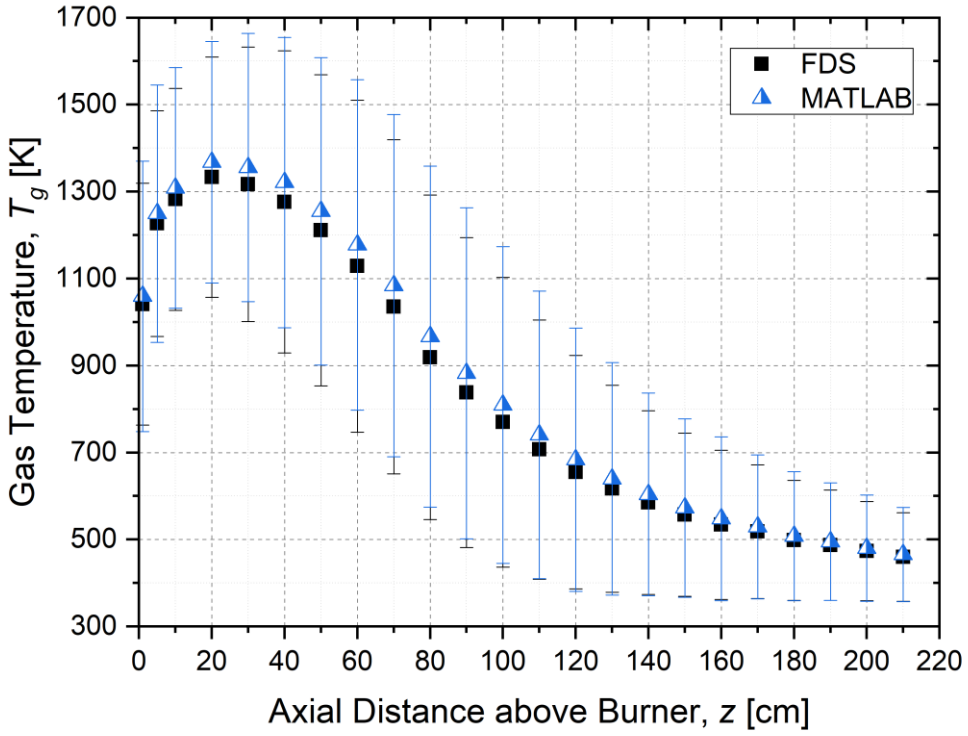

Figure D6. Comparison of the mean and standard deviation of the gas temperature by the FDS simulation with the measured thermocouple temperatures corrected for thermal inertia and radiative loss by the MATLAB code as a function of the axial distance above the burner centerline.

This publication is available free of charge from: https://doi.org/10.6028/NIST.TN.2083r1

Table D3. Comparison of the mean and standard deviation of the corrected gas temperatures using FDS ($\bar{T}_{g,FDS}$ and $\sigma_{T_{g,FDS}}$) and the in-house MATLAB code ($\bar{T}_{g,MAT}$ and $\sigma_{T_{g,MAT}}$) as a function of the axial distance above the burner along the fire centerline.

z [cm]	r [cm]	$\overline{T}_{g,FDS}$ [K]	$\overline{T}_{g,MAT}$ [K]	$\frac{\overline{T}_{g,MAT} - \overline{T}_{g,FDS}}{\overline{T}_{g,FDS}}$	$\sigma_{T_{g,FDS}}$ [K]	$\sigma_{T_{g,MAT}}$ [K]	$\frac{\sigma_{T_{g,MAT}} - \sigma_{T_{g,FDS}}}{\sigma_{T_{g,FDS}}}$
1	0	1037	1059	2 %	276	311	13 %
5	0	1226	1249	2 %	260	296	14 %
10	0	1281	1308	2 %	255	277	9 %
20	0	1331	1367	3 %	276	278	1 %
30	0	1314	1356	3 %	316	309	-2 %
40	0	1273	1321	4 %	348	334	-4 %
50	0	1208	1255	4 %	358	353	-1 %
60	0	1126	1177	5 %	382	380	-0.5 %
70	0	1034	1084	5 %	384	394	2 %
80	0	918	967	5 %	374	392	5 %
90	0	837	882	5 %	357	381	7 %
100	0	770	810	5 %	334	364	9 %
110	0	707	741	5 %	299	331	10 %
120	0	656	684	4 %	270	303	12 %
130	0	618	639	3 %	239	267	12 %
140	0	587	604	3 %	211	233	10 %
150	0	560	573	2 %	188	205	9 %
160	0	537	548	2 %	171	188	10 %
170	0	520	529	2 %	154	166	8 %
180	0	499	508	2 %	138	148	7 %
190	0	488	495	1 %	127	135	6 %
200	0	474	480	1 %	115	122	6 %
210	0	460	466	1 %	103	108	6 %

This publication is available free of charge from: https://doi.org/10.6028/NIST.TN.2083r1

E Uncertainty Analysis

Estimates of uncertainty are evaluated using the method descried by Taylor and Kuyatt [14]. A series of measurement, denoted by y, can be expressed as a function of its associated independent variables, x_i. The function f in Eq. E1 contains all quantities that significantly contribute to the measurement:

$$y = f(x_1, x_2, x_3, \cdots, x_N) \tag{E1}$$

In the case that all input parameters are uncorrelated, the combined standard uncertainty is given by Eq. E2, referred to as *the law of propagation of uncertainty*.

$$u_c(y) = \sqrt{\sum_{i=1}^{N} \left(s_i \cdot u(x_i)\right)^2} \tag{E2}$$

where $u_c(y)$ is the combined standard uncertainty and $u(x_i)$ is the standard uncertainty of each input parameter. The parameter, s_i, is the non-dimensional sensitivity coefficient, defined as:

$$s_i = \frac{\partial f}{\partial x_i}\frac{x_i}{y} \tag{E3}$$

A series of measurements allows computation of statistics of their uncertainties during steady burning and the standard deviation of the output estimate, σ_y, is considered an uncertainty component. The expanded combined uncertainty, $U_c(y)$, is defined as:

$$U_c(y) = k\sqrt{u_c(y)^2 + \sigma_y^2} \tag{E4}$$

where the coverage factor, k, is taken as equal to 2, so that the expanded combined uncertainty, U_c, defines an interval representing approximately a 95 % confidence level.

E.1 Gas Temperature Uncertainty Methodology

The instantaneous thermal inertia temperature correction term is as large as hundreds of degrees, whereas its mean value is less than 1 K (see *Section 3.7*). In other words, the thermal inertia correction term has a negligible influence on the mean gas temperature, but does amplify the value of the instantaneous temperature extremes. Table E1 presents the mean and standard deviation of the gas temperature time series measurements as a function of location. The contributions of the thermal inertia and radiative loss correction terms to the mean and standard deviation of the gas temperature are also shown. Correction of the mean temperature due to radiative loss along the centerline was about 1 % on average, varying from near zero at the top of the fire plume to 1.7 % at the hottest fire locations as seen in Table E1. The last column in the table shows that the uncertainty in the thermal inertia correction term represents, on average, about 54 % of the standard deviation of the gas temperature for locations along the centerline. In contrast, the uncertainty in the radiative loss term contributes little influence on the standard deviation of the gas temperature. For these reasons, the uncertainties of the mean and standard deviation of the gas temperature were separately analyzed.

In this section, the uncertainty of the instantaneous gas temperature is estimated. Next, the uncertainties of the mean and standard deviation of the gas temperature are separately analyzed. Appendix E.1.1 presents the uncertainty of the instantaneous gas temperature for every data point in the time series. The contribution of the uncertainty of the bead temperature, radiative loss correction temperature and thermal inertia correction temperature is analyzed for the instantaneous gas temperature. Appendix E.1.2 presents the uncertainty of the mean and standard deviation of the gas temperature separately.

Table E1. Mean and standard deviation of the measured gas temperature (T_g), the radiative loss correction term (T_{rad}) and the thermal inertia correction term (T_{the}) along the burner centerline in the 1 m methanol pool fire. The bar above the symbol represents the mean value of that parameter.

z [cm]	r [cm]	$\overline{T}_g$ [K]	$\overline{T}_{rad}$ [K]	$\overline{T}_{the}$ [K]	$\frac{\overline{T}_{rad}}{\overline{T}_g}$	σ_{T_g} [K]	$\sigma_{T_{rad}}$ [K]	$\sigma_{T_{the}}$ [K[	$\frac{\sigma_{T_{the}}}{\sigma_{T_g}}$
5	0	1144	15.0	0.13	1.3 %	424	15	330	38 %
10	0	1274	20.6	0.14	1.6 %	244	16.5	343	66 %
20	0	1359	23.5	-0.22	1.7 %	211	14.8	290	65 %
30	0	1371	23.2	0.11	1.7 %	209	13.1	271	63 %
40	0	1318	20.3	0.1	1.5 %	249	12.8	273	55 %
60	0	1214	14.9	0.03	1.2 %	269	11.4	287	53 %
80	0	1008	8.0	-0.02	0.8 %	286	8.7	291	51 %
100	0	819	3.7	0.15	0.5 %	267	5.8	265	50 %
110	0	750	2.5	0.1	0.3 %	239	4.4	236	49 %
120	0	695	1.7	0.14	0.2 %	217	3.3	214	49 %
130	0	631	1.1	0.08	0.2 %	191	2.4	186	49 %
140	0	605	0.8	-0.04	0.1 %	177	1.8	174	49 %
160	0	561	0.5	0.07	0.1 %	155	1.3	149	48 %
180	0	515	0.3	0.05	0.1 %	121	0.6	120	50 %
200	0	472	0.1	-0.05	0.0 %	96	0.3	96	50 %
210	0	458	0.1	-0.07	0.0 %	92	0.3	90	49 %

E.1.1 Uncertainty of the Instantaneous Gas Temperature

Based on the energy balance at the thermocouple bead (Eq. 3), the instantaneous gas temperature (T_g) is rewritten as:

$$T_g = T_b + \frac{\rho_b c_{p,b} d_b^2}{6\mathrm{Nu}\lambda_g}\frac{dT_b}{dt} + \frac{\epsilon\sigma d_b}{\mathrm{Nu}\lambda_g}\left(T_b^4 - T_{surr}^4\right) \quad \text{(E5)}$$

where the second and third terms on the right side represent the instantaneous thermal inertia correction term (T_{the}) and the instantaneous radiative loss correction term (T_{rad}), respectively.

The uncertainty of the instantaneous gas temperature, $u_c(T_g)$, is estimated as:

$$u_c(T_g) = \sqrt{u_c(T_b)^2 + u_c(T_{rad})^2 + u_c(T_{the})^2} \quad \text{(E6)}$$

This publication is available free of charge from: https://doi.org/10.6028/NIST.TN.2083r1

where $u_c(T_b)$ is the uncertainty of the instantaneous bead temperature. The relative uncertainty of the instantaneous bead temperature has a constant value of 0.65 % which is the square root of the sum of squares of the temperature calibration error (0.25 % in 273 K < T_b < 1733 K) [39] and DAQ measurement uncertainty (0.6 %) for the application range of the thermocouple [40]. $u_c(T_{rad})$ and $u_c(T_{the})$ was calculated using the propagation error method [14] based on the energy balance at the thermocouple bead as described by Eq. E5.

The term $u_c(T_{rad})$ is the uncertainty of the instantaneous radiative loss correction term in Eq. E6:

$$u_c(T_{rad}) = \sqrt{u_c(\epsilon_b)^2 + u_c(d_b)^2 + \left(4u_c(T_b)\right)^2 + u_c\left(\lambda_g\right)^2 + u_c(\mathrm{Nu})^2} \tag{E7}$$

The value of $u_c(\mathrm{Nu})$ is estimated as:

$$u_c(\mathrm{Nu}) = \sqrt{\left(\frac{1}{2}u_c(\mathrm{Re}_d)\right)^2 + \left(\frac{1}{3}u_c(\mathrm{Pr})\right)^2} \tag{E8}$$

and $u_c(T_{the})$ is the uncertainty of the instantaneous thermal inertia correction term in Eq. E6:

$$u_c(T_{the}) = \sqrt{u_c(\rho_b)^2 + u_c\left(c_{p,b}\right)^2 + u_c(\mathrm{Nu})^2 + u_c\left(\lambda_g\right)^2 + \left(2 \cdot u_c(d_b)\right)^2 + u_c\left(\frac{dT_b}{dt}\right)} \tag{E9}$$

The bead temperature is measured with a sampling rate of 60 Hz. The instantaneous uncertainty is calculated for every data point in the time series.

The measurement uncertainty of the bead temperature affects the temperature-dependent thermophysical properties of the air and thermocouple bead calculated with Eqs. A1 - A2, leading to the propagation of error in the radiative loss and thermal inertia correction terms. The uncertainty of the instantaneous temperature is influenced by uncertainty of the temperature-dependent thermophysical properties of the thermocouple. Here, the uncertainties of the bead diameter, gas velocity and dT_b/dt are approximately constant, taking the values presented in Table E2.

Table E2. Uncertainties of the bead diameter, gas velocity and dT_b/dt.

Parameter, x	**Uncertainty, $u_c(x)$**
Bead diameter (d_b)	5 %[a]
Gas velocity (V_g)	4 %[b]
dT_b/dt	5 %[c]

[a] in general.

[b] from Ref. [6].

[c] in *Appendix D.3*, the uncertainty of the time derivative of the bead temperature due to the polynomial fitting was 8 % on average along the centerline. Thus, the uncertainty of dT_b/dt was estimated as 5 %.

This publication is available free of charge from: https://doi.org/10.6028/NIST.TN.2083r1

The uncertainty analysis described below is conducted at (z, r) = (30 cm, 0 cm), which is considered a representative location (Experiment date: 03/11, Repeat no. 3). Figure E1 shows the gas temperature and the bead temperature as a function of time and the error band (red color) indicates the absolute uncertainty of the instantaneous gas temperature, $u_c(T_g)$. The uncertainty increases when the bead temperature changes rapidly, that is, when dT_b/dt is large.

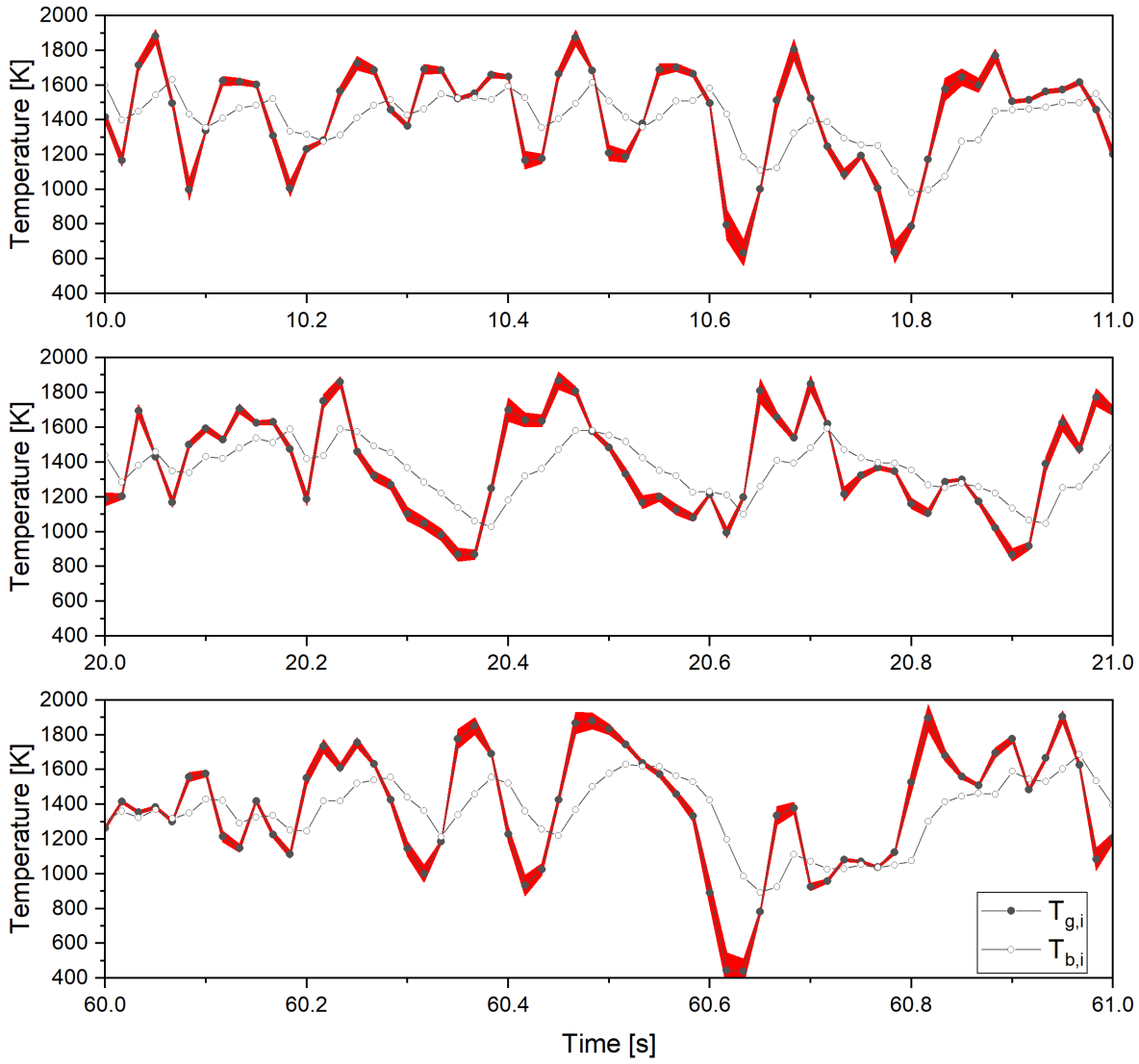

Figure E1. Gas temperature (T_g) and the thermocouple bead temperature (T_b) as a function of time during three periods of the experiment; the error band (red color) indicates the absolute uncertainty of the instantaneous gas temperature at (z, r) = (30 cm, 0 cm), (Experiment date: 03/11, Repeat no. 3).

This publication is available free of charge from: https://doi.org/10.6028/NIST.TN.2083r1

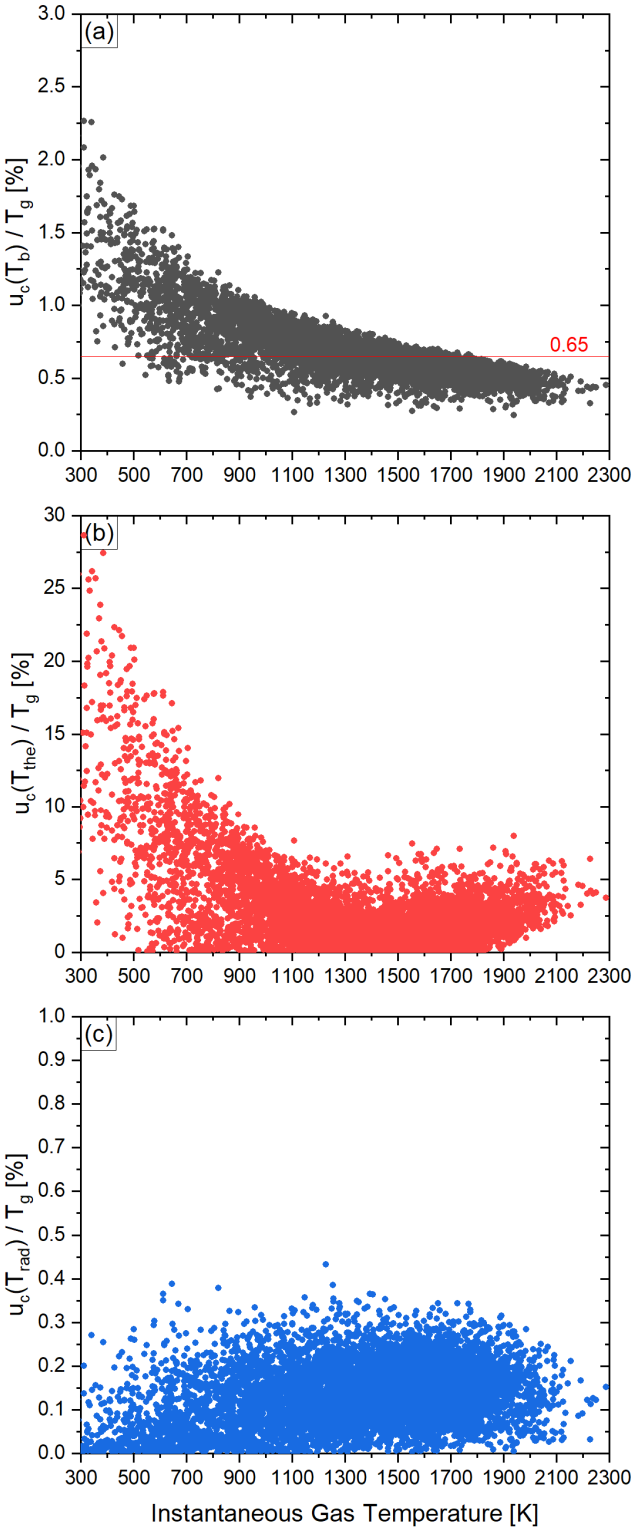

Figure E2. Relative uncertainty of the instantaneous gas temperature contributed by (a) the instantaneous measured bead temperature, (b) the thermal inertia correction term and (c) the radiative loss correction term as a function of the instantaneous gas temperature at (z, r) = (30 cm, 0 cm), (Experiment date: 03/11, Repeat no. 3).

This publication is available free of charge from: https://doi.org/10.6028/NIST.TN.2083r1

Figure E2 shows the contributions of $u_c(T_b), u_c(T_{rad})$ and $u_c(T_{the})$ to the relative uncertainty of the corrected instantaneous gas temperature (T_g) as a function of the corrected instantaneous gas temperature. In Figure E2a, $u_c(T_b)/T_g$ increases as T_g decreases. The relative uncertainty of the instantaneous bead temperature, $u_c(T_b)/T_b$, has a constant value of about 0.65 % (see discussion below Eq. E6). For T_g < 500 K, $u_c(T_b)/T_g$ is larger than about 0.65 %, which suggests that the corrected instantaneous gas temperature (T_g) is smaller than the measured thermocouple bead temperature (T_b). This result must be due to the thermal inertia correction term because the radiative loss correction term is always positive. This is the reason that the relative uncertainty of T_{the}/T_g increased rapidly as T_g decreased as seen in Figure E2c. On the other hand, $u_c(T_b)/T_g$ is larger than 0.65 % for T_g > 1900 K, indicating that T_g is larger than T_b.

Figure E3 shows contributions of the uncertainty of the instantaneous gas temperature uncertainty $(u_c(T_g))$ by uncertainties in the bead temperature $(u_c(T_b))$, the radiative loss correction term $(u_c(T_{rad}))$, and the thermal inertia correction term $(u_c(T_{the}))$ as a function of $T_g(t)$. For T_g < 700 K or T_g > 2000 K, $u_c(T_{the})$ is the dominant contributor to the uncertainty. On the other hand, the contributions appear to be distributed randomly for 700 K < T_g < 2000 K. As expected, $u_c(T_{rad})$ increases with T_g.

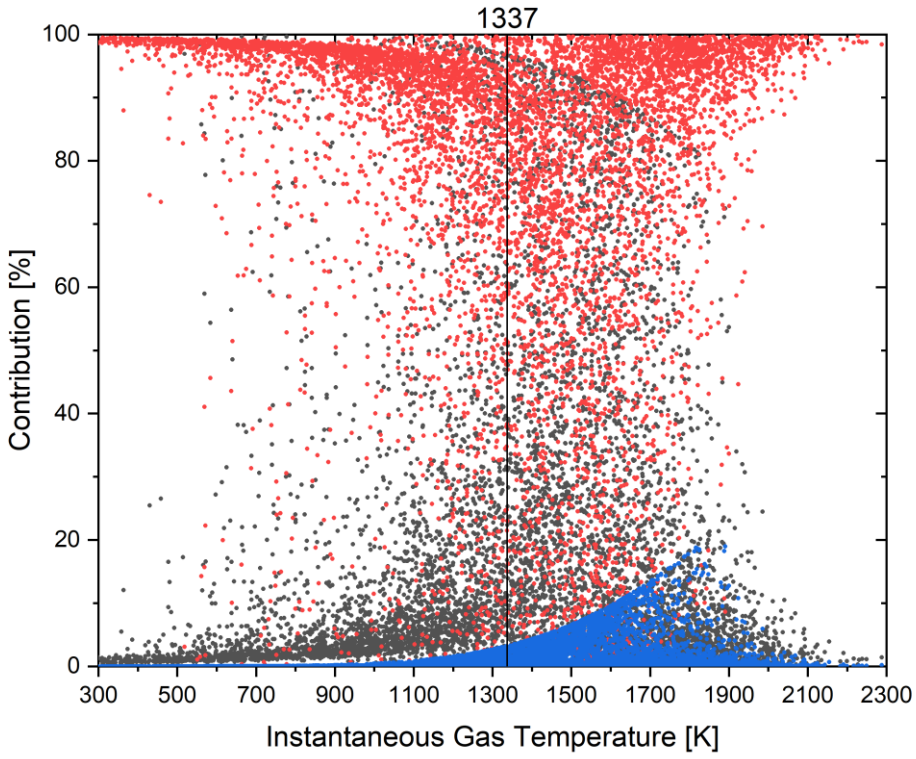

Figure E3. Contribution of the uncertainty of the bead temperature (black symbols), the radiative loss correction term (blue symbols) and the thermal inertia correction term (red symbols) to the uncertainty of the instantaneous gas temperature as a function of the gas temperature at (z, r) = (30 cm, 0 cm), (Experiment date: 03/11, Repeat no. 3).

This publication is available free of charge from: https://doi.org/10.6028/NIST.TN.2083r1

Figure E4 shows the mean contribution to the uncertainty of the instantaneous gas temperature by $u_c(T_b)$, $u_c(T_{rad})$ and $u_c(T_{the})$ as a function of the gas temperature. Here, the mean contribution represents the average uncertainty contributions considering data binned in 100 K increments of T_g for 300 K < T_g < 2300 K. As expected, $u_c(T_{the})$ is the dominant contributor to $u_c(T_g)$ for T_g < 700 K or T_g > 2000 K, whereas for 700 K < T_g < 2000 K, $u_c(T_b)$ is also important.

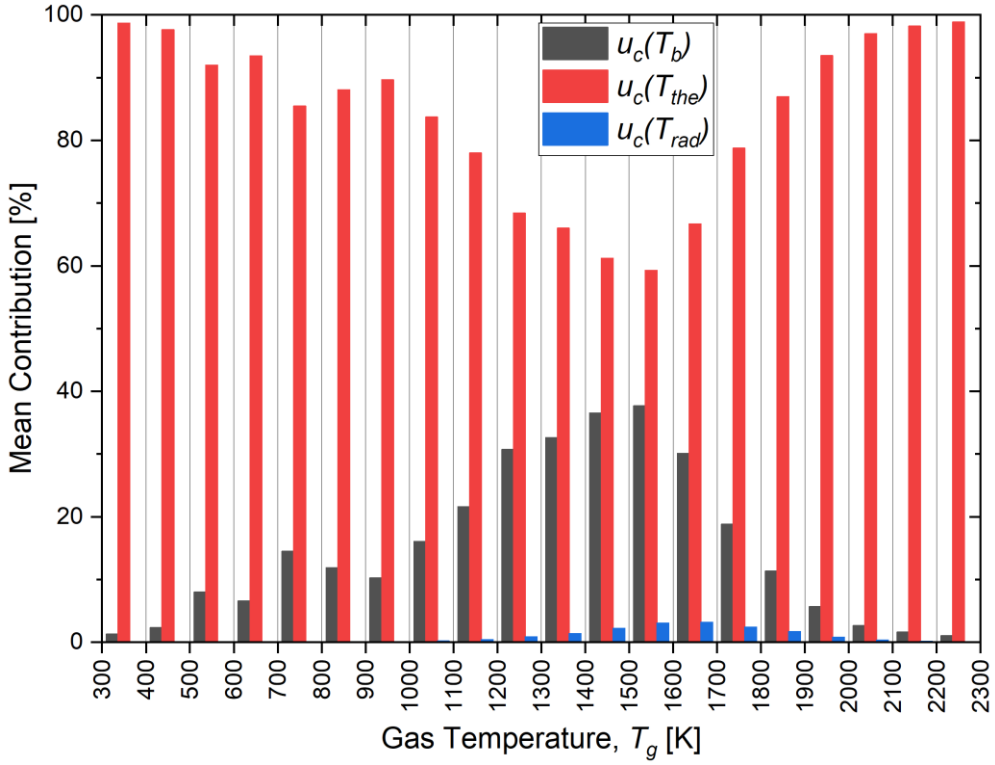

Figure E4. Mean contribution of the uncertainty of the bead temperature, radiative loss correction and the thermal inertia correction term to the uncertainty of the instantaneous gas temperature as a function of the gas temperature at (z, r) = (30 cm, 0 cm), (Experiment date: 03/11, Repeat no. 3); the Y axis represents the average uncertainty contributions considering data binned in 100 K increments of T_g for 300 K < T_g < 2300 K.

Figure E5 shows the relative uncertainty of T_g as a function of the instantaneous gas temperature for one time series experimental dataset at one location. The red line represents a second order polynomial fit to the data. The distribution and magnitude of uncertainties are similar to the relative uncertainty of T_{the} seen in Figure E2, it means that the uncertainty of the instantaneous thermal inertia correction temperature contributes dominantly to the uncertainty of the instantaneous gas temperature. As the gas temperature approached the ambient temperature, the relative uncertainty of T_g rapidly increased. The results show that unreasonably low gas temperatures (close to the ambient temperature) were sometimes measured, indicating some bias in the term dT_b/dt as it rapidly changed. This was not unexpected.

This publication is available free of charge from: https://doi.org/10.6028/NIST.TN.2083r1

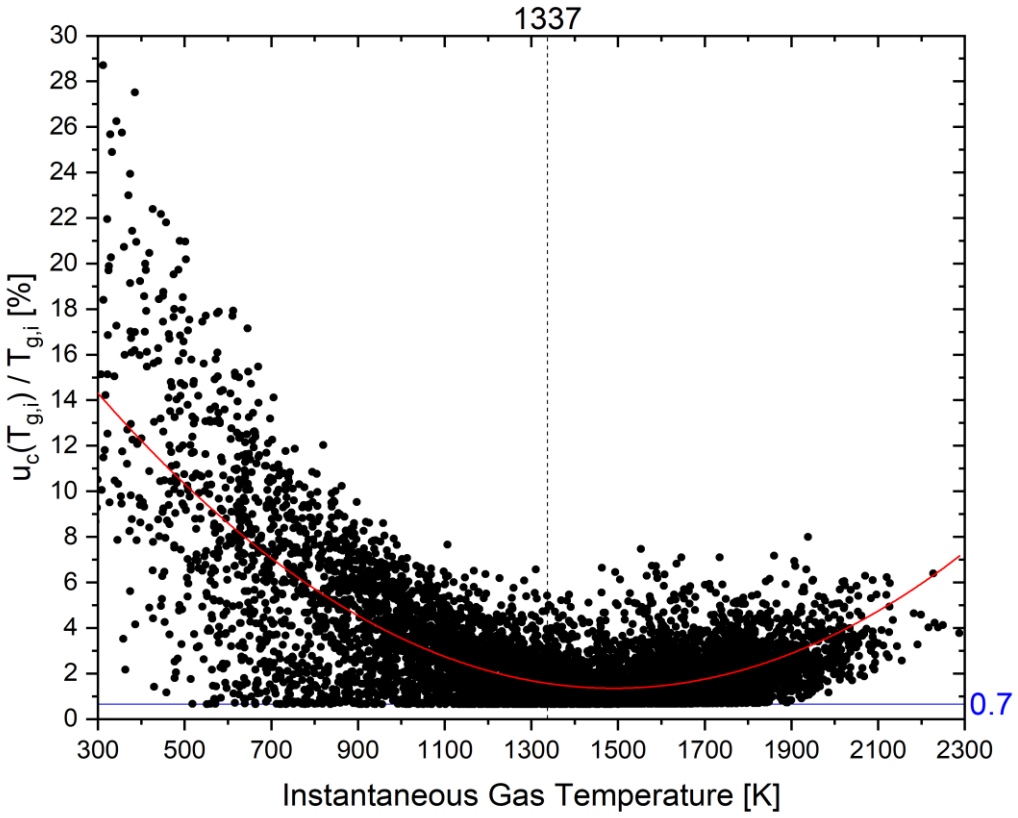

Figure E5. Relative uncertainty of the instantaneous gas temperature as a function of the gas temperature at (z, r) = (30 cm, 0 cm), (Experiment date: 03/11, Repeat no. 3).

E.1.2 Uncertainty of the Mean and Standard Deviation of the Gas Temperature

E.1.2.1 Uncertainty of the Mean Gas Temperature

The uncertainty of the mean gas temperature is estimated considering the energy balance on the thermocouple bead (see Eq. 5). Experimental repeatability (σ_R) and measurement accuracy of the devices, such as thermocouple and data acquisition system, are also considered as part of the uncertainty analysis.

The expanded combined uncertainty of the mean gas temperature, $U_c(\overline{T}_g)$, was calculated with Eq. E10, here the uncertainty from the thermal inertia correction term was excluded since it contributes to the instantaneous gas temperature, but not to the mean temperature.

$$U_c(\overline{T}_g) = 2\sqrt{u_c(\overline{T}_b)^2 + u_c(\overline{T}_{rad})^2 + \sigma_R(\overline{T}_g)^2} \tag{E10}$$

where the term $u_c(\overline{T}_b)$ is estimated considering the calibration error of the thermocouple, $u_c(T_{cal})$, and the accuracy of the data acquisition (DAQ) system, $u_c(T_{\mathrm{DAQ}})$ in Eq. E11. The calibration error of a Type S thermocouple is 0.25 % in 273 K < T_b < 1733 K [39]. The measurement uncertainty of the data acquisition (DAQ) system is approximately 0.6 % for the application range of the thermocouple [40].

$$u_c(\overline{T}_b) = \sqrt{u_c(T_{cal})^2 + u_c(T_{\mathrm{DAQ}})^2 + \sigma_R(\overline{T}_b)^2} \quad \text{(E11)}$$

$u_c(\overline{T}_{rad})$ was related with the thermophysical properties of the gas and the thermocouple bead.

$$u_c(\overline{T}_{rad}) = \sqrt{u_c(\overline{\epsilon}_b)^2 + u_c(d_b)^2 + \left(4u_c(\overline{T}_b)\right)^2 + u_c(\overline{\lambda}_g)^2 + u_c(\overline{\mathrm{Nu}})^2 + \sigma_R(\overline{T}_{rad})^2} \quad \text{(E12)}$$

where d_b is the bead diameter of the thermocouple, taken as $u_c(d_b)$ was 5 %. The value of $u_c(\overline{\mathrm{Nu}})$ is estimated as:

$$u_c(\overline{\mathrm{Nu}}) = \sqrt{\left(\frac{1}{2}u_c(\overline{\mathrm{Re}}_d)\right)^2 + \left(\frac{1}{3}u_c(\overline{\mathrm{Pr}})\right)^2 + \sigma_R(\overline{\mathrm{Nu}})^2} \quad \text{(E8)}$$

In Eq. E8, $u_c(\overline{\mathrm{Re}_d})$ and $u_c(\overline{\mathrm{Pr}})$ are estimated as:

$$u_c(\overline{\mathrm{Re}}_d) = \sqrt{u_c(d_b)^2 + u_c(\overline{v}_g)^2 + u_c(\overline{V}_g)^2 + \sigma_R(\overline{\mathrm{Re}}_d)^2} \quad \text{(E13)}$$

$$u_c(\overline{\mathrm{Pr}}) = \sqrt{u_c(\overline{c}_{p,g})^2 + u_c(\overline{\mu}_g)^2 + u_c(\overline{\lambda}_g)^2 + \sigma_R(\overline{\mathrm{Pr}})^2} \quad \text{(E14)}$$

Table E3 shows the uncertainty budget of the mean thermocouple bead temperature ($\overline{T}_b$) and the mean radiative correction term ($\overline{T}_{rad}$) at (z, r) = (30 cm, 0 cm), using Eqn. E11 and E12.

Table E3. Uncertainty budget of the mean thermocouple bead temperature ($\overline{T}_b$) and the mean radiative correction term ($\overline{T}_{rad}$) at (z, r) = (30 cm, 0 cm).

Uncertainty	**Parameter** x	$s(x)_i$ **[-]**	**Uncertainty** $u_c(x)$ **[-]**	**Contribution [%]**
TC bead temperature, $u_c(\overline{T}_b)$	DAQ measurement uncertainty (T_{DAQ})	1	0.60 %	6 %
	Thermocouple calibration error (T_{cal})	1	0.25 %	1 %
	Repeatability (σ_R)	1	2.4 %	93 %
	$\overline{T}_b$		2.5 %	100 %
Radiative loss correction term, $u_c(\overline{T}_{rad})$	$\overline{\epsilon}_b$	1	2.4 %	3 %
	d_b	1	5.0 %	13 %
	$\overline{T}_b$	4	2.5 %	50 %
	$\overline{\lambda}_g$	1	1.6 %	1 %
	$\overline{\mathrm{Nu}}$	1	3.9 %	8 %
	Repeatability (σ_R)	1	7.0 %	25 %
	$\overline{T}_{rad}$		14 %	100 %

This publication is available free of charge from: https://doi.org/10.6028/NIST.TN.2083r1

The uncertainty budget of the mean gas temperature ($\overline{T}_g$) listed in Table E4. The mean gas temperature and its expanded combined uncertainty at (z, r) = (30 cm, 0 cm) are 1371 K ± 7 % ($k = 2$).

Table E4. Uncertainty budget of the mean gas temperature ($\overline{T}_g$) at (z, r) = (30 cm, 0 cm).

Parameter x	**Mean value** $\overline{x}$ **[K]**	**Uncertainty** $u_c(x)$ **[K]**	**Contribution [%]**
Radiative loss correction term, $\overline{T}_{rad}$	23	3	0.3 %
Thermocouple bead temperature, $\overline{T}_b$	1347	33	48 %
Repeatability (σ_R)	-	34	51 %
Gas temperature, $\overline{T}_g$	1371	47	100 %

E.1.2.2 Uncertainty of the Standard Deviation of the Gas Temperature

The expanded combined uncertainty of the standard deviation of the corrected gas temperature, $U_c(\sigma_{T_g})$ is calculated using Eq. E15 and the results are presented in *Appendix E.1.2.3* below. The gas temperature time series can be characterized by its mean and standard deviation. The standard deviation has an uncertainty associated with the instrument characteristics, most notably, its time response. If the time response is slow, the extremes of the instantaneous temperature will not reflect the true gas temperature and the standard deviation will be cut-off. Thus, there is some uncertainty in determining the standard deviation of the gas temperature. In this regard, the uncertainty of the radiative loss correction term is negligibly small compared to the thermal inertia correction term, so it is not considered here. The expanded combined uncertainty of the standard deviation of the gas temperature, $U_c(\sigma_{T_g})$, can be estimated as:

$$U_c\left(\sigma_{T_g}\right) = 2\sqrt{u_c\left(\sigma_{T_{the}}\right)^2 + \sigma_R\left(\sigma_{T_g}\right)^2} \tag{E15}$$

The term $u_c(\sigma_{T_{the}})$ was estimated as:

$$u_c\left(\sigma_{T_{the}}\right) = \sqrt{u_c\left(\sigma_{\rho_b}\right)^2 + u_c\left(\sigma_{c_{p,b}}\right)^2 + u_c(\sigma_{\mathrm{Nu}})^2 + u_c\left(\sigma_{\lambda_g}\right)^2 + \left(2 \cdot u_c(d_b)\right)^2 + u_c\left(\frac{dT_b}{dt}\right)^2} \tag{E16}$$

The terms $u_c(d_b)$ and $u_c(dT_b/dt)$ are listed in Table E2. The term $u_c(\sigma_{\mathrm{Nu}})$ is estimated as:

$$u_c(\sigma_{\mathrm{Nu}}) = \sqrt{\left(\frac{1}{2}u_c\left(\sigma_{\mathrm{Re}_d}\right)\right)^2 + \left(\frac{1}{3}u_c(\sigma_{\mathrm{Pr}})\right)^2} \tag{E17}$$

In Eq. E17, the term $u_c(\sigma_{\mathrm{Re}_d})$ and $u_c(\sigma_{\mathrm{Pr}})$ are estimated as:

$$u_c\left(\sigma_{\mathrm{Re}_d}\right) = \sqrt{u_c(d_b)^2 + u_c\left(\sigma_{\nu_g}\right)^2 + u_c\left(\sigma_{V_g}\right)^2} \tag{E18}$$

This publication is available free of charge from: https://doi.org/10.6028/NIST.TN.2083r1

$$u_c(\sigma_{\mathrm{Pr}}) = \sqrt{u_c\left(\sigma_{c_{p,g}}\right)^2 + u_c\left(\sigma_{\mu_g}\right)^2 + u_c\left(\sigma_{\lambda_g}\right)^2} \tag{E19}$$

Table E5 shows the uncertainty budget of the standard deviation of the thermal inertia correction term ($\sigma_{T_{the}}$) and the gas temperature (σ_{T_g}) at (z, r) = (30 cm, 0 cm), using Eqn. E15 and E16. The standard deviation of the gas temperature and its expanded combined uncertainty at (z, r) = (30 cm, 0 cm) are 350 K ± 30 % ($k = 2$).

Table E5. Uncertainty budget of the standard deviation of the thermal inertia correction term ($\sigma_{T_{the}}$) and the gas temperature (σ_{T_g}) at (z, r) = (30 cm, 0 cm).

Uncertainty	**Parameter x**	**$s(x)_i$ [-]**	**Uncertainty $u_c(x)$ [-]**	**Contribution [%]**
Thermal inertia correction term, $u_c(\sigma_{T_{the}})$	σ_{ρ_b}	1	0.04 %	0.0 %
	$\sigma_{c_{p,b}}$	1	0.5 %	0.2 %
	d_b	2	5.0 %	70 %
	σ_{λ_g}	1	1.6 %	2 %
	σ_{Nu}	1	3.8 %	10 %
	dT_b/dt	1	5.0 %	18 %
	$\sigma_{T_{the}}$		12 %	100 %
Gas temperature, $u_c(\sigma_{T_g})$	$\sigma_{T_{the}}$	1	12 %	63 %
	Repeatability (σ_R)	1	9 %	37 %
	σ_{T_g}		15 %	100 %

E.1.2.3 Combined Uncertainties of the Thermocouple and Corrected Gas Temperatures

Table E6 presents the measured mean thermocouple bead temperature ($\overline{T}_b$) and its standard deviation (σ_{T_b}), as well as the expanded combined uncertainties ($U_c(\overline{T}_g)$ and $U_c(\sigma_{T_g})$) of the corrected mean gas temperature ($\overline{T}_g$) and its standard deviation (σ_{T_g}), respectively, as described in *Appendices E.1.2.1* and *E.1.2.2*. It should be noted that the $\overline{T}_g$ is always larger than $\overline{T}_b$ due to the correction for radiative loss, and that $U_c(\sigma_{T_g})$ is always larger than $U_c(\overline{T}_g)$ mainly due to the uncertainty associated with the thermal inertia correction term. The average value of the combined uncertainty $U_c(\overline{T}_g)$ of the mean gas temperature ($\overline{T}_g$) is equal to 5 % and the average value of the combined uncertainty $U_c(\sigma_{T_g})$ of the standard deviation of the gas temperature measurement (σ_{T_g}) is significantly larger and equal to 26 %.

This publication is available free of charge from: https://doi.org/10.6028/NIST.TN.2083r1

Table E6. Mean and standard deviation of the measured bead temperature (T_b) and the corrected gas temperature (T_g) as a function of the axial and radial position; the expanded combined uncertainties ($U_c(\overline{T}_g)$ and $U_c(\sigma_{T_g})$) of the mean and standard deviation of the gas temperature ($\overline{T}_g$ and σ_{T_g}) are presented separately.

z [cm]	r [cm]	$\overline{T}_b$ [K]	σ_{T_b} [K]	$\overline{T}_g$ [K]	$U_c(\overline{T}_g)$ [-]	σ_{T_g} [K]	$U_c(\sigma_{T_g})$ [-]
5	0	1129	252	1144	9 %	424	24 %
10	0	1253	244	1274	3 %	430	24 %
20	0	1335	211	1359	3 %	367	25 %
30	0	1347	209	1371	7 %	350	30 %
40	0	1297	249	1318	6 %	378	24 %
60	0	1187	278	1202	4 %	411	23 %
80	0	1000	286	1008	15 %	413	27 %
100	0	816	267	819	12 %	380	25 %
110	0	748	239	750	7 %	338	25 %
120	0	693	217	695	4 %	307	24 %
130	0	630	191	631	16 %	267	29 %
140	0	604	177	605	2 %	249	23 %
160	0	561	155	561	1 %	216	23 %
180	0	515	121	515	9 %	171	26 %
200	0	472	96	472	5 %	136	24 %
210	0	458	92	458	1 %	129	23 %
20	-10	1291	237	1313	2 %	383	24 %
60	-10	1016	301	1024	7 %	415	24 %
100	-10	701	247	703	1 %	338	23 %
140	-10	552	169	553	1 %	233	23 %
180	-10	516	128	516	1 %	180	23 %
20	10	1269	250	1290	1 %	405	23 %
60	10	1105	294	1118	10 %	433	25 %
100	10	816	275	820	1 %	396	23 %
140	10	622	197	623	1 %	276	23 %
180	10	514	134	515	1 %	188	23 %
20	20	901	322	909	27 %	477	31 %
60	20	733	293	737	11 %	415	25 %
100	20	696	261	698	1 %	380	23 %
140	20	549	261	549	1 %	380	23 %
180	20	462	111	462	1 %	162	23 %
20	30	674	327	678	25 %	454	31 %
60	30	541	245	542	6 %	336	24 %
100	30	522	198	523	1 %	278	23 %

----- Table E6 Continued on Next Page -----

This publication is available free of charge from: https://doi.org/10.6028/NIST.TN.2083r1

z [cm]	r [cm]	$\overline{T}_b$ [K]	σ_{T_b} [K]	$\overline{T}_g$ [K]	$U_c(\overline{T}_g)$ [-]	σ_{T_g} [K]	$U_c(\sigma_{T_g})$ [-]
140	30	488	149	488	1 %	218	23 %
180	30	413	96	413	1 %	143	23 %
20	40	465	271	467	11 %	364	29 %
60	40	443	197	444	8 %	265	26 %
100	40	441	151	441	1 %	216	23 %
140	40	428	122	428	1 %	183	23 %
180	40	393	91	393	1 %	139	23 %
20	50	302	48	303	5 %	70	59 %
60	50	338	102	338	10 %	135	43 %
100	50	380	102	380	1 %	149	23 %
140	50	391	95	391	1 %	151	23 %
180	50	351	68	351	1 %	105	23 %

E.2 Uncertainty of the Heat Release Rate

In this study, the actual heat release rate ($\dot{Q}_a$) is measured using oxygen consumption calorimetry and compared with the ideal heat release rate ($\dot{Q}$) calculated from the mass burning rate, ($\dot{m}\Delta H_c$). The mean and standard deviation of the mass burning rate ($\dot{m}$), the ideal heat release rate and the actual heat release rate in repeat experiments are listed in Table E7. Appendix Sections E.2.1 and E.2.2 provide the uncertainties of the actual heat release rate and the ideal heat release rate, respectively.

Table E7. Mean and standard deviation of the measured mass burning rate ($\dot{m}$), the ideal heat release rate ($\dot{Q}$) and the heat release rate obtained from calorimetry ($\dot{Q}_a$) in three repeat experiments.

Date	$\overline{\dot{m}}$ [g/s]	$\sigma(\dot{m})$ [g/s]	$\overline{\dot{Q}}$ [kW]	$\sigma(\dot{Q})$ [kW]	$\overline{\dot{Q}}_a$ [kW]	$\sigma(\dot{Q}_a)$ [kW]
03/11/2019	13.0	0.3	258	6	250	21
03/19/2019	12.8	0.3	254	6	254	18
03/26/2019	12.6	0.8	251	16	263	22

E.2.1 Uncertainty of the Actual Heat Release Rate

The expanded combined uncertainty of the actual heat release rate measured by oxygen consumption calorimetry is estimated as:

$$U_c(\dot{Q}_a) = 2\sqrt{u(\dot{Q}_a)^2 + u_c(\dot{Q}_{cal})^2 + \sigma\left(\overline{\dot{Q}}_a\right)^2} \quad \text{(E20)}$$

where $u(\dot{Q}_a)$ is the standard uncertainty of the measured heat release rate and $u_c(\dot{Q}_{cal})$ is the calorimetry measurement uncertainty previously reported as 3.4 % [13]. Here, $\sigma(\overline{\dot{Q}}_a)$ is the repeatability of the measurement. The mean and expanded combined uncertainty of $\dot{Q}_a$ is 256 kW ± 18 % (± 45 kW).

This publication is available free of charge from: https://doi.org/10.6028/NIST.TN.2083r1

E.2.2 Uncertainty of the Ideal Heat Release Rate

The expanded combined uncertainty of the ideal heat release rate calculated from the burning rate is estimated as:

$$U_c(\dot{Q}) = 2\sqrt{u(\dot{Q})^2 + \sigma\left(\overline{\dot{Q}}\right)^2 + u_c(\dot{m})^2} \quad \text{(E21)}$$

where $u(\dot{Q})$ is the standard uncertainty of the ideal heat release rate and $\sigma(\overline{\dot{Q}})$ is the repeatability of the measurement. $u_c(\dot{m})$ is the combined uncertainty of the mass burning rate. The mean and expanded combined uncertainty of the ideal heat releaser rate is 254 kW ± 7 % (±19 kW).

E.3 Uncertainty of the Radiative Heat Flux

The heat flux gauges were calibrated using a secondary standard gauge in a well-characterized calibration facility [21]. The calibration method and apparatus are described in Ref. [41]; the systematic uncertainty for the calibration, $u_c(cal)$, is estimated as 2.3 % [21]. The measurement accuracy of the data acquisition system (DAQ, Model: SCXI-1600), $u_c(DAQ)$, is 0.076 % in an application range [40]. The expanded combined uncertainty of the corrected heat flux is estimated as:

$$U_c(\dot{q}_c'') = 2\sqrt{\sigma(\dot{q}_c'')^2 + \sigma_R\left(\overline{\dot{q}_c''}\right)^2 + u_c(cal.)^2 + u_c(DAQ)^2} \quad \text{(E22)}$$

where $\sigma_R(\overline{\dot{q}_c''})$ is the repeatability in repeat measurements. Appendix E.3.1 presents the heat flux correction method to remove the background heat flux from the (uncorrected) measured heat flux.

E.3.1 Background Heat Flux Estimate

The measured (uncorrected) heat flux can be affected by the temperature of surroundings (walls, calorimeter hood) and the water circulating in the gauge. The ambient air temperature and the cooling water temperature were maintained on consistently 26 °C ± 0.8 °C and 15 °C ± 0.1 °C, averaged from 2000 s to 5000 s as seen in Figure E6.

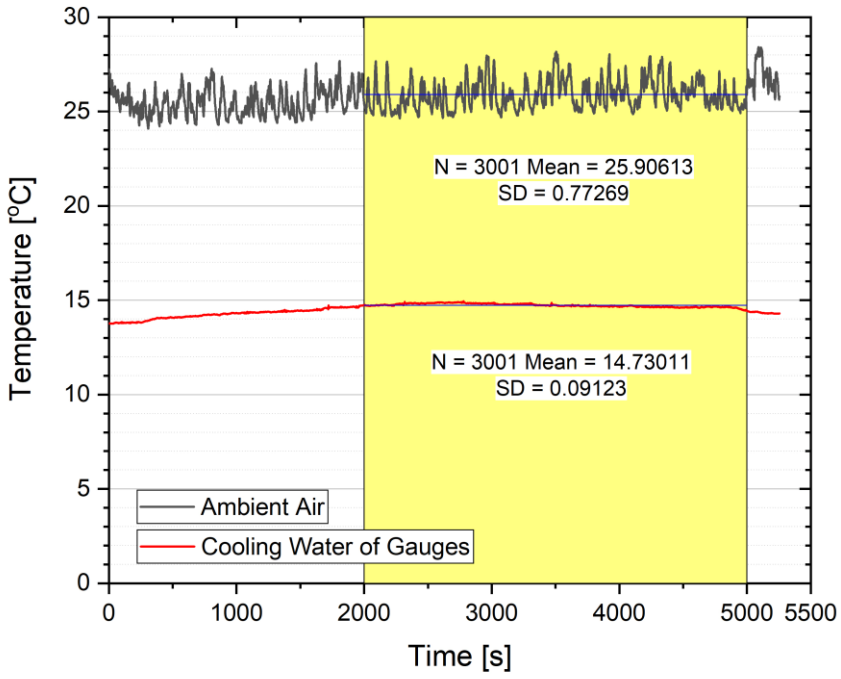

Figure E6. Ambient temperature and cooling water temperature of heat flux gauges as a function of time in Test 1; The yellow region indicates the average window.

In general, the transient heat flux followed approximately the trends as seen in Figure E7. The heat flux slightly increased during the steady burning period as the fire slowly heated up the surroundings continuously. Immediately after the fire was extinguished, the heat flux declined sharply, then slowly decreased as the surroundings cooled; an inflection point formed as seen in Figure E7. In this study, two curve fits are used to represent the time series heat flux data to find the inflection point, which is takes as the background heat flux ($\dot{q}_b''$). The corrected heat flux ($\dot{q}_c''$) is then calculated as:

$$\dot{q}_c'' = \dot{q}_s'' - \dot{q}_b'' \tag{E23}$$

where $\dot{q}_s$ is the measured (uncorrected) heat flux during the steady burning.

This publication is available free of charge from: https://doi.org/10.6028/NIST.TN.2083r1

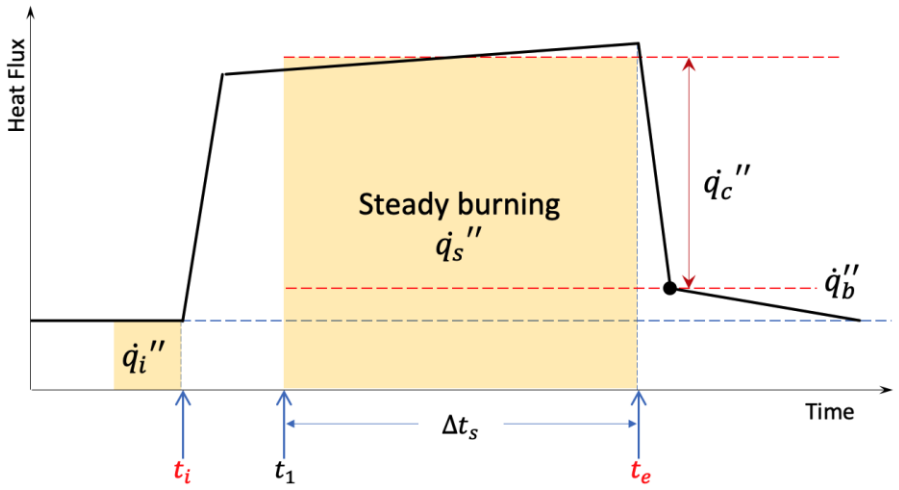

Figure E7. Heat flux change with time; t_i and t_e are the fire ignition and extinction times, respectively.

E.3.2 Radiative Heat Flux in the Downward Direction

The radiative heat flux was measured using the radial heat flux gauges (Gauge 6 - 11 seen in Figure 4, see *Section 2.2*). The mean, standard deviation and the extended uncertainty of the corrected heat flux measured in the downward direction is listed in Table E8. The uncertainty at r = 117 cm is relatively large due to the relatively large standard deviation of the measured heat flux.

Table E8. Mean, standard deviation and expanded combined uncertainty of the corrected heat flux in the downward direction as a function of radial distance from the burner centerline.

z [cm]	r [cm]	$\overline{\dot{q}_c''}$ [kW/m^2]	σ [kW/m^2]	$U_c(\dot{q}_c'')$ [-]
0	52.5	5.11	1.02	40 %
0	57.7	4.07	0.32	16 %
0	71.5	2.62	0.91	69 %
0	117	1.03	0.60	117 %
0	167.2	0.35	0.16	90 %
0	207.2	0.20	0.05	52 %

E.3.3 Radiative Heat Flux in the Radial Direction

The radiative heat flux was measured using the heat flux gauges faced to the fire (Gauge 1 - 5 and Gauge 12 - 14 seen in Figure 4). The mean, standard deviation heat flux and the extended uncertainty of the corrected heat flux in the radial direction is listed in Table E9.

This publication is available free of charge from: https://doi.org/10.6028/NIST.TN.2083r1

Table E9. Mean, standard deviation and expanded combined uncertainty of the corrected heat flux in the radial direction as a function of the distance from the centerline and distance above the burner.

z [cm]	r [cm]	$\overline{\dot{q}_c''}$ [kW/m^2]	σ [kW/m^2]	$U_c(\dot{q}_c'')$ [-]	z [cm]	r [cm]	$\overline{\dot{q}_c''}$ [kW/m^2]	σ [kW/m^2]	$U_c(\dot{q}_c'')$ [-]
0	207.5	0.84	0.03	8 %	60	450	0.22	0.03	24 %
40	300	0.56	0.03	13 %	60	500	0.16	0.03	36 %
40	325	0.47	0.03	15 %	80	300	0.56	0.03	13 %
40	350	0.39	0.04	19 %	80	325	0.47	0.03	15 %
40	400	0.27	0.03	22 %	80	350	0.39	0.04	19 %
40	450	0.20	0.02	23 %	80	400	0.27	0.03	22 %
40	500	0.16	0.03	32 %	80	450	0.20	0.02	23 %
45	207.5	0.98	0.08	17 %	80	500	0.16	0.03	32 %
60	300	0.57	0.03	12 %	90	207.5	1.00	0.10	21 %
60	325	0.49	0.03	14 %	135	207.5	0.82	0.09	22 %
60	350	0.41	0.03	17 %	179.5	207.5	0.67	0.08	24 %
60	400	0.28	0.03	22 %					

E.4 Uncertainty of the Radiative Fraction

The radiative fraction (χ_{rad}) is defined by Eq. 11 and is rewritten here for convenience:

$$\chi_{rad} = \frac{\dot{Q}_{rad}}{\dot{Q}} \tag{E24}$$

where $\dot{Q}$ is the actual heat release rate measured using oxygen consumption calorimetry and $\dot{Q}_{rad}$ is the radiative emission by the fire to the surroundings and the pool surface (see Eq. 13). The expanded combined uncertainty of the radiative fraction is estimated as:

$$U_c(\chi_{rad}) = 2\sqrt{u_c(\dot{Q}_{rad})^2 + u_c(\dot{Q}_a)^2} \tag{E25}$$

In this study, the total radiative emission from the fire ($\dot{Q}_{rad}$) is estimated using two methods including integration of the measured heat flux distribution over a virtual cylindrical surface and a single point estimate. In Eq. E25, the term $u_c(\dot{Q}_{rad})$ is presented separately using each method and the results are compared. Appendix E.4.1 provides the uncertainty analysis of χ_{rad} using integration method using the polynomial fitting functions. Appendix E.4.2 provides the uncertainty analysis of χ_{rad} for a single point estimate.

E.4.1 Uncertainty of the Radiative Fraction Based on Fitting Functions

The total radiative heat emission from the fire ($\dot{Q}_{rad}$) is broken into the radiative energy emitted by the fire to the surroundings except to the fuel surface ($\dot{Q}_r$) and the radiative heat feedback to the fuel surface ($\dot{Q}_{sr}$). Based on a propagation of uncertainty analysis of Eq. 13, the expanded combined uncertainty of $\dot{Q}_{rad}$ is:

This publication is available free of charge from: https://doi.org/10.6028/NIST.TN.2083r1

$$U_c(\dot{Q}_{rad}) = 2\sqrt{u_c(\dot{Q}_r)^2 + u_c(\dot{Q}_{sr})^2} \quad \text{(E26)}$$

To determine $\dot{Q}_r$, the radiative heat flux through a virtual cylinder surrounding the fire (see Eq. 13) is integrated using either a cubic or linear fit, depending on the integration region. The energy difference in the fits is treated as the uncertainty, $u_c(\dot{Q}_r)$ estimated as 2.9 %. The total heat feedback to the fuel surface ($\dot{Q}_s$) is broken into radiative ($\dot{Q}_{sr}$) and convective heat feedback ($\dot{Q}_{sc}$) such that $\dot{Q}_{sr} = \dot{Q}_s - \dot{Q}_{sc}$. Here, the term $\dot{Q}_{sc}$ is calculated using Eq. 14 considering thin film theory. To determine ($\dot{Q}_s$), the fractional heat feedback to the fuel surface (χ_s) in the 1 m pool fire is assumed to be about the same as in the 30 cm poll fire (= 0.082 ± 24 %; k = 2) [29]. The expanded combined uncertainty of the term ($\dot{Q}_{sr}$) is then estimated as:

$$U_c(\dot{Q}_{sr}) = 2\sqrt{\left(u_c(\chi_s)^2 + u_c(\dot{Q}_a)^2\right) + u_c(\dot{Q}_{sc})^2} \quad \text{(E27)}$$

where the first two terms on the right represent $u_c(\dot{Q}_r)^2$ in Eq. E26. For convenience, Table E10 summarizes the uncertainties of parameters contributing to the uncertainty of χ_{rad}. The uncertainties in the table are expressed as relative values in the form of percentages. A propagation of uncertainty analysis shows that the mean and expanded combined uncertainty of the radiative fraction using Eq. 13 is 0.22 ± 16 %.

Table E10. Uncertainty scorecard: expanded combined uncertainty of parameters related to the radiative fraction based on the radiative energy integrated using fitting functions.

Parameter x	**Relevant Equation**	**Expanded combined uncertainty** $U_c(x)$ **[-]**
$\dot{m}''$	Eq. 14	7 %
T_o	Eq. 14	1 %
$\dot{Q}_a$	Eqs. 11 and 12	17 %
$\dot{Q}_{rad}$	Eqs. 11-13 and E26	12 %
$\dot{Q}_r$	Eqs. 11-13	6 %
$\dot{Q}_{sr}$	Eqs. 11-13 and E27	36 %
$\dot{Q}_{sc}$	Eqs. 14 and E27	26 %
χ_{sr}	Eqs. 11-12 and E26	31 %
χ_r	Eqs. 11 and 12	18 %
χ_s	Eqs. 13 and 14	24 %†
χ_{sc}	Eqs. 13 and 14	31 %
χ_{rad}	Eqs. 13 and E24	16 %

† assumed to be the same as in a 30 cm methanol pool fire [29].

E.4.2 Uncertainty of the Radiative Fraction Estimate Based on a Single Point Measurement

Modak [30] suggests that a distance five times the diameter of a fire is adequately far enough away to use a single point location measurement of the total radiative flux, assuming isotropy. For isotropic radiation, the radiative energy emitted from a fire ($\dot{Q}_{rad}$) is expressed by Eq. 15 and rewritten here for convenience:

$$\dot{Q}_{rad} = 4\pi r^2 \dot{q}''(r,z) \tag{E28}$$

The results show the flame radiative power output assuming radiative isotropy tends to underestimate the total radiative energy emitted by the flame with a bias of about 2 % at *r/D* = 5. This is treated here as uncertainty in the single point radiation estimate method, $u_c(\dot{Q}_{rad,model})$. The expanded combined uncertainty of the radiative heat flux using a single point estimate is estimated as:

$$U_c(\chi_{rad}) = 2\sqrt{u_c(\dot{q}'')^2 + u_c\left(\dot{Q}_{rad,model}\right)^2 + u_c\left(\dot{Q}_a\right)^2} \tag{E29}$$

The mean and expanded combined uncertainty of the radiative fraction using a single point estimate is estimated as 0.20 ± 34 %.

F Liquid Fuel Temperature

Table F1 lists the mean, standard deviation and expanded combined uncertainty of the liquid fuel temperature (T_l) as a function of the axial distance below the burning fuel surface. The radial position of the thermocouple is 35 cm from the burner centerline. The temperature dropped with distance from the surface, which was nearly at the boiling point of methanol.

Table F1. Mean, standard deviation and expanded combined uncertainty of the liquid fuel temperature as a function of the axial distance below the burning fuel surface. The radial position of the thermocouple is 35 cm from the burner centerline.

Test no.	z **[mm]**	$\overline{T}_l$ **[°C]**	σ_{T_l} **[°C]**	$U_c(T_l)$ **[-]**
Test 1	0.4	65	0.5	1.7 %
	-0.4	65	0.6	1.8 %
	-1.7	64	0.7	2.3 %
	-3.3	56	1.1	3.8 %
	-5.7	42	0.5	2.3 %
	-11	30	0.3	2.4 %
	-20.6	22	0.1	1.0 %
	-25.4	21	0.1	1.0 %
	-40.8	22	0.2	1.3 %
Test 2	-51	19	0.1	1.1 %
	-0.1	64	0.4	1.3 %
	-1.2	66	0.4	1.9 %
	-3.3	65	0.6	2.3 %
	-5.2	58	0.7	1.4 %
	-10	46	0.3	0.6 %
	-20.3	34	0.1	0.5 %
	-40.4	27	0.1	0.3 %
	-40.8	26	0.0	0.0 %

G Cold Length of the Thermocouple Wire

According to Ref. [42], conductive heat loss is negligible if the actual length of the thermocouple wire (l) is grader than 10 times the *cold length* of the wire (l_c), that is : $l/l_c > 10$, where the cold length of the thermocouple wire is given by Ref. [42]:

$$l_c = \frac{d_w}{2}\sqrt{\frac{\lambda_w}{\lambda_g \cdot \mathrm{Nu}}} \tag{G1}$$

and d_w and λ_w are the diameter and thermal conductivity of the wire, respectively. Assuming that the wire is cylindrical, the Nusselt number correlation for the circular cylinder in crossflow [43] is defined as:

$$\mathrm{Nu} = 0.989\mathrm{Re}_d{}^{0.330}\mathrm{Pr}^{1/3}; \qquad 0.4 \le \mathrm{Re}_d \le 4, \qquad \mathrm{Pr} \ge 0.7 \tag{G2}$$

This criterion accounts for both the characteristics of the flow and the thermocouple's thermophysical properties. Applying Eqs. G1 - G2, the mean and standard deviation of the cold length for T_g averaged from 400 K to 1600 K is 0.94 mm ± 0.02 mm. The cold length and relevant variables depending on temperature are listed in Table A.8. Here, the distance between the bead and ceramic tube was 1 cm; thus, conductive heat loss was neglected in the energy balance of the bead.

Table G1. Cold length and its variables as a function of temperature in V_g= 2 m/s, d_w= 50μm; The mean and standard deviation of cold length is 0.94 mm ± 0.02 mm.

T_g [K]	ν_g [m²/s]	$\mathrm{Re_d}$ [-]	Pr [-]	Nu [-]	λ_w† [W/m/K]	λ_g [W/m/K]	l_c [mm]
400	2.59E-05	3.9	0.69	1.36	71.5	3.37E-02	0.99
500	3.78E-05	2.6	0.68	1.20	72.0	4.04E-02	0.96
600	5.13E-05	2.0	0.68	1.08	72.6	4.66E-02	0.95
700	6.61E-05	1.5	0.68	1.00	73.4	5.24E-02	0.94
800	8.21E-05	1.2	0.69	0.93	74.5	5.77E-02	0.93
900	9.94E-05	1.0	0.70	0.88	75.7	6.28E-02	0.93
1000	1.18E-04	0.9	0.70	0.83	77.1	6.75E-02	0.93
1100	1.37E-04	0.7	0.71	0.79	78.7	7.21E-02	0.93
1200	1.57E-04	0.6	0.71	0.76	80.6	7.64E-02	0.93
1300	1.79E-04	0.6	0.72	0.73	82.6	8.05E-02	0.94
1400	2.01E-04	0.5	0.72	0.70	84.8	8.45E-02	0.94
1600	2.47E-04	0.4	0.72	0.66	89.9	9.20E-02	0.96

†from Ref. [44]

This publication is available free of charge from: https://doi.org/10.6028/NIST.TN.2083r1

H FDS Input File

&HEAD CHID='NIST_TN2083_Methanol_1m_pan_1cm_grid', TITLE='NIST Methanol Pool, 1 m pan, 1 cm resolution' /

&TIME T_END=60/

&MISC TMPA=25., SIMULATION_MODE='LES' /

&DUMP DT_HRR=1.0, DT_DEVC_LINE=50., DT_RESTART=10.0, DT_DEVC=1E-7/

&MESH XB=-0.3, 0.0,-0.3,0.0,-0.2, 0.2, IJK=30,30,40, MULT_ID='mesh' /
&MULT ID='mesh', DX=0.3, DY=0.3, DZ=0.4, I_LOWER=-1, I_UPPER=2, J_LOWER=-1, J_UPPER=2, K_UPPER=5 /

&COMB RADIATIVE_FRACTION=0.22, SUPPRESSION=.FALSE., N_SIMPLE_CHEMISTRY_REACTIONS=2, FUEL_C_TO_CO_FRACTION=1.0, FUEL_H_TO_H2_FRACTION=0.5 /

&REAC FUEL='METHANOL' /

&SLCF PBY=0.001, QUANTITY='VELOCITY', VECTOR=.TRUE. /
&SLCF PBY=0.001, QUANTITY='TEMPERATURE', CELL_CENTERED=.TRUE. /
&SLCF PBY=0.001, QUANTITY='TEMPERATURE' /
&SLCF PBY=0.001, QUANTITY='VOLUME FRACTION', SPEC_ID='OXYGEN', CELL_CENTERED=.TRUE. /
&SLCF PBY=0.001, QUANTITY='VOLUME FRACTION', SPEC_ID='CARBON DIOXIDE', CELL_CENTERED=.TRUE. /
&SLCF PBY=0.001, QUANTITY='VOLUME FRACTION', SPEC_ID='CARBON MONOXIDE', CELL_CENTERED=.TRUE. /
&SLCF PBY=0.001, QUANTITY='VOLUME FRACTION', SPEC_ID='METHANOL', CELL_CENTERED=.TRUE. /

&MATL ID='STEEL', CONDUCTIVITY=54, DENSITY=7800, SPECIFIC_HEAT=0.465, EMISSIVITY=0.8 /

&SURF ID='PAN', COLOR='GRAY 50', MATL_ID='STEEL', THICKNESS=0.003/

&SURF ID='POOL', COLOR='LIGHT BLUE', SPEC_ID='METHANOL', TMP_FRONT=64.6, MASS_FLUX=0.0163 /

&VENT MB='ZMIN', SURF_ID='OPEN' /
&VENT MB='ZMAX', SURF_ID='OPEN' /
&VENT MB='YMIN', SURF_ID='OPEN' /
&VENT MB='YMAX', SURF_ID='OPEN' /
&VENT MB='XMIN', SURF_ID='OPEN' /
&VENT MB='XMAX', SURF_ID='OPEN' /

&PROP ID='T_db153_R00_Z001 props', BEAD_DIAMETER=153.3E-6, BEAD_EMISSIVITY=0.135, BEAD_DENSITY=21241, BEAD_SPECIFIC_HEAT=0.155/
&PROP ID='T_db153_R00_Z005 props', BEAD_DIAMETER=153.3E-6, BEAD_EMISSIVITY=0.135, BEAD_DENSITY=21241, BEAD_SPECIFIC_HEAT=0.155/
&PROP ID='T_db153_R00_Z010 props', BEAD_DIAMETER=153.3E-6, BEAD_EMISSIVITY=0.150,

BEAD_DENSITY=21210, BEAD_SPECIFIC_HEAT=0.158/
&PROP ID='T_db153_R00_Z020 props', BEAD_DIAMETER=153.3E-6, BEAD_EMISSIVITY=0.160, BEAD_DENSITY=21190, BEAD_SPECIFIC_HEAT=0.160/
&PROP ID='T_db153_R00_Z030 props', BEAD_DIAMETER=153.3E-6, BEAD_EMISSIVITY=0.161, BEAD_DENSITY=21187, BEAD_SPECIFIC_HEAT=0.160/
&PROP ID='T_db153_R00_Z040 props', BEAD_DIAMETER=153.3E-6, BEAD_EMISSIVITY=0.159, BEAD_DENSITY=21191, BEAD_SPECIFIC_HEAT=0.160/
&PROP ID='T_db153_R00_Z050 props', BEAD_DIAMETER=153.3E-6, BEAD_EMISSIVITY=0.152, BEAD_DENSITY=21204, BEAD_SPECIFIC_HEAT=0.158/
&PROP ID='T_db153_R00_Z060 props', BEAD_DIAMETER=153.3E-6, BEAD_EMISSIVITY=0.145, BEAD_DENSITY=21219, BEAD_SPECIFIC_HEAT=0.157/
&PROP ID='T_db153_R00_Z070 props', BEAD_DIAMETER=153.3E-6, BEAD_EMISSIVITY=0.131, BEAD_DENSITY=21245, BEAD_SPECIFIC_HEAT=0.154/
&PROP ID='T_db153_R00_Z080 props', BEAD_DIAMETER=153.3E-6, BEAD_EMISSIVITY=0.116, BEAD_DENSITY=21273, BEAD_SPECIFIC_HEAT=0.151/
&PROP ID='T_db153_R00_Z090 props', BEAD_DIAMETER=153.3E-6, BEAD_EMISSIVITY=0.102, BEAD_DENSITY=21296, BEAD_SPECIFIC_HEAT=0.149/
&PROP ID='T_db153_R00_Z100 props', BEAD_DIAMETER=153.3E-6, BEAD_EMISSIVITY=0.088, BEAD_DENSITY=21319, BEAD_SPECIFIC_HEAT=0.147/
&PROP ID='T_db153_R00_Z110 props', BEAD_DIAMETER=153.3E-6, BEAD_EMISSIVITY=0.077, BEAD_DENSITY=21336, BEAD_SPECIFIC_HEAT=0.145/
&PROP ID='T_db153_R00_Z120 props', BEAD_DIAMETER=153.3E-6, BEAD_EMISSIVITY=0.068, BEAD_DENSITY=21349, BEAD_SPECIFIC_HEAT=0.144/
&PROP ID='T_db153_R00_Z130 props', BEAD_DIAMETER=153.3E-6, BEAD_EMISSIVITY=0.057, BEAD_DENSITY=21365, BEAD_SPECIFIC_HEAT=0.142/
&PROP ID='T_db153_R00_Z140 props', BEAD_DIAMETER=153.3E-6, BEAD_EMISSIVITY=0.055, BEAD_DENSITY=21368, BEAD_SPECIFIC_HEAT=0.142/
&PROP ID='T_db153_R00_Z150 props', BEAD_DIAMETER=153.3E-6, BEAD_EMISSIVITY=0.050, BEAD_DENSITY=21375, BEAD_SPECIFIC_HEAT=0.141/
&PROP ID='T_db153_R00_Z160 props', BEAD_DIAMETER=153.3E-6, BEAD_EMISSIVITY=0.044, BEAD_DENSITY=21383, BEAD_SPECIFIC_HEAT=0.140/
&PROP ID='T_db153_R00_Z170 props', BEAD_DIAMETER=153.3E-6, BEAD_EMISSIVITY=0.040, BEAD_DENSITY=21388, BEAD_SPECIFIC_HEAT=0.140/
&PROP ID='T_db153_R00_Z180 props', BEAD_DIAMETER=153.3E-6, BEAD_EMISSIVITY=0.035, BEAD_DENSITY=21394, BEAD_SPECIFIC_HEAT=0.139/
&PROP ID='T_db153_R00_Z190 props', BEAD_DIAMETER=153.3E-6, BEAD_EMISSIVITY=0.031, BEAD_DENSITY=21399, BEAD_SPECIFIC_HEAT=0.139/
&PROP ID='T_db153_R00_Z200 props', BEAD_DIAMETER=153.3E-6, BEAD_EMISSIVITY=0.026, BEAD_DENSITY=21405, BEAD_SPECIFIC_HEAT=0.138/
&PROP ID='T_db153_R00_Z210 props', BEAD_DIAMETER=153.3E-6, BEAD_EMISSIVITY=0.023, BEAD_DENSITY=21408, BEAD_SPECIFIC_HEAT=0.138/
&PROP ID='T_db153_R10_Z001 props', BEAD_DIAMETER=153.3E-6, BEAD_EMISSIVITY=0.142, BEAD_DENSITY=21224, BEAD_SPECIFIC_HEAT=0.156/
&PROP ID='T_db153_R10_Z005 props', BEAD_DIAMETER=153.3E-6, BEAD_EMISSIVITY=0.144, BEAD_DENSITY=21219, BEAD_SPECIFIC_HEAT=0.157/
&PROP ID='T_db153_R10_Z010 props', BEAD_DIAMETER=153.3E-6, BEAD_EMISSIVITY=0.148,

BEAD_DENSITY=21213, BEAD_SPECIFIC_HEAT=0.158/
&PROP ID='T_db153_R10_Z020 props', BEAD_DIAMETER=153.3E-6, BEAD_EMISSIVITY=0.155, BEAD_DENSITY=21199, BEAD_SPECIFIC_HEAT=0.159/
&PROP ID='T_db153_R10_Z030 props', BEAD_DIAMETER=153.3E-6, BEAD_EMISSIVITY=0.149, BEAD_DENSITY=21210, BEAD_SPECIFIC_HEAT=0.158/
&PROP ID='T_db153_R10_Z040 props', BEAD_DIAMETER=153.3E-6, BEAD_EMISSIVITY=0.143, BEAD_DENSITY=21222, BEAD_SPECIFIC_HEAT=0.157/
&PROP ID='T_db153_R10_Z050 props', BEAD_DIAMETER=153.3E-6, BEAD_EMISSIVITY=0.136, BEAD_DENSITY=21234, BEAD_SPECIFIC_HEAT=0.155/
&PROP ID='T_db153_R10_Z060 props', BEAD_DIAMETER=153.3E-6, BEAD_EMISSIVITY=0.130, BEAD_DENSITY=21247, BEAD_SPECIFIC_HEAT=0.154/
&PROP ID='T_db153_R10_Z070 props', BEAD_DIAMETER=153.3E-6, BEAD_EMISSIVITY=0.119, BEAD_DENSITY=21267, BEAD_SPECIFIC_HEAT=0.152/
&PROP ID='T_db153_R10_Z080 props', BEAD_DIAMETER=153.3E-6, BEAD_EMISSIVITY=0.108, BEAD_DENSITY=21285, BEAD_SPECIFIC_HEAT=0.150/
&PROP ID='T_db153_R10_Z090 props', BEAD_DIAMETER=153.3E-6, BEAD_EMISSIVITY=0.097, BEAD_DENSITY=21303, BEAD_SPECIFIC_HEAT=0.148/
&PROP ID='T_db153_R10_Z100 props', BEAD_DIAMETER=153.3E-6, BEAD_EMISSIVITY=0.088, BEAD_DENSITY=21319, BEAD_SPECIFIC_HEAT=0.147/
&PROP ID='T_db153_R10_Z110 props', BEAD_DIAMETER=153.3E-6, BEAD_EMISSIVITY=0.078, BEAD_DENSITY=21334, BEAD_SPECIFIC_HEAT=0.145/
&PROP ID='T_db153_R10_Z120 props', BEAD_DIAMETER=153.3E-6, BEAD_EMISSIVITY=0.069, BEAD_DENSITY=21347, BEAD_SPECIFIC_HEAT=0.144/
&PROP ID='T_db153_R10_Z130 props', BEAD_DIAMETER=153.3E-6, BEAD_EMISSIVITY=0.062, BEAD_DENSITY=21358, BEAD_SPECIFIC_HEAT=0.143/
&PROP ID='T_db153_R10_Z140 props', BEAD_DIAMETER=153.3E-6, BEAD_EMISSIVITY=0.055, BEAD_DENSITY=21367, BEAD_SPECIFIC_HEAT=0.142/
&PROP ID='T_db153_R10_Z150 props', BEAD_DIAMETER=153.3E-6, BEAD_EMISSIVITY=0.049, BEAD_DENSITY=21376, BEAD_SPECIFIC_HEAT=0.141/
&PROP ID='T_db153_R10_Z160 props', BEAD_DIAMETER=153.3E-6, BEAD_EMISSIVITY=0.043, BEAD_DENSITY=21384, BEAD_SPECIFIC_HEAT=0.140/
&PROP ID='T_db153_R10_Z170 props', BEAD_DIAMETER=153.3E-6, BEAD_EMISSIVITY=0.039, BEAD_DENSITY=21389, BEAD_SPECIFIC_HEAT=0.140/
&PROP ID='T_db153_R10_Z180 props', BEAD_DIAMETER=153.3E-6, BEAD_EMISSIVITY=0.035, BEAD_DENSITY=21394, BEAD_SPECIFIC_HEAT=0.139/
&PROP ID='T_db153_R10_Z190 props', BEAD_DIAMETER=153.3E-6, BEAD_EMISSIVITY=0.030, BEAD_DENSITY=21401, BEAD_SPECIFIC_HEAT=0.138/
&PROP ID='T_db153_R10_Z200 props', BEAD_DIAMETER=153.3E-6, BEAD_EMISSIVITY=0.026, BEAD_DENSITY=21406, BEAD_SPECIFIC_HEAT=0.138/
&PROP ID='T_db153_R10_Z210 props', BEAD_DIAMETER=153.3E-6, BEAD_EMISSIVITY=0.022, BEAD_DENSITY=21410, BEAD_SPECIFIC_HEAT=0.137/
&PROP ID='T_db153_R20_Z001 props', BEAD_DIAMETER=153.3E-6, BEAD_EMISSIVITY=0.104, BEAD_DENSITY=21289, BEAD_SPECIFIC_HEAT=0.150/
&PROP ID='T_db153_R20_Z005 props', BEAD_DIAMETER=153.3E-6, BEAD_EMISSIVITY=0.103, BEAD_DENSITY=21290, BEAD_SPECIFIC_HEAT=0.150/
&PROP ID='T_db153_R20_Z010 props', BEAD_DIAMETER=153.3E-6, BEAD_EMISSIVITY=0.102,

BEAD_DENSITY=21292, BEAD_SPECIFIC_HEAT=0.150/
&PROP ID='T_db153_R20_Z020 props', BEAD_DIAMETER=153.3E-6, BEAD_EMISSIVITY=0.099, BEAD_DENSITY=21298, BEAD_SPECIFIC_HEAT=0.149/
&PROP ID='T_db153_R20_Z030 props', BEAD_DIAMETER=153.3E-6, BEAD_EMISSIVITY=0.095, BEAD_DENSITY=21303, BEAD_SPECIFIC_HEAT=0.148/
&PROP ID='T_db153_R20_Z040 props', BEAD_DIAMETER=153.3E-6, BEAD_EMISSIVITY=0.089, BEAD_DENSITY=21313, BEAD_SPECIFIC_HEAT=0.147/
&PROP ID='T_db153_R20_Z050 props', BEAD_DIAMETER=153.3E-6, BEAD_EMISSIVITY=0.081, BEAD_DENSITY=21325, BEAD_SPECIFIC_HEAT=0.146/
&PROP ID='T_db153_R20_Z060 props', BEAD_DIAMETER=153.3E-6, BEAD_EMISSIVITY=0.073, BEAD_DENSITY=21340, BEAD_SPECIFIC_HEAT=0.145/
&PROP ID='T_db153_R20_Z070 props', BEAD_DIAMETER=153.3E-6, BEAD_EMISSIVITY=0.072, BEAD_DENSITY=21341, BEAD_SPECIFIC_HEAT=0.145/
&PROP ID='T_db153_R20_Z080 props', BEAD_DIAMETER=153.3E-6, BEAD_EMISSIVITY=0.071, BEAD_DENSITY=21343, BEAD_SPECIFIC_HEAT=0.144/
&PROP ID='T_db153_R20_Z090 props', BEAD_DIAMETER=153.3E-6, BEAD_EMISSIVITY=0.069, BEAD_DENSITY=21346, BEAD_SPECIFIC_HEAT=0.144/
&PROP ID='T_db153_R20_Z100 props', BEAD_DIAMETER=153.3E-6, BEAD_EMISSIVITY=0.067, BEAD_DENSITY=21349, BEAD_SPECIFIC_HEAT=0.144/
&PROP ID='T_db153_R20_Z110 props', BEAD_DIAMETER=153.3E-6, BEAD_EMISSIVITY=0.061, BEAD_DENSITY=21358, BEAD_SPECIFIC_HEAT=0.143/
&PROP ID='T_db153_R20_Z120 props', BEAD_DIAMETER=153.3E-6, BEAD_EMISSIVITY=0.054, BEAD_DENSITY=21368, BEAD_SPECIFIC_HEAT=0.142/
&PROP ID='T_db153_R20_Z130 props', BEAD_DIAMETER=153.3E-6, BEAD_EMISSIVITY=0.048, BEAD_DENSITY=21377, BEAD_SPECIFIC_HEAT=0.141/
&PROP ID='T_db153_R20_Z140 props', BEAD_DIAMETER=153.3E-6, BEAD_EMISSIVITY=0.041, BEAD_DENSITY=21386, BEAD_SPECIFIC_HEAT=0.140/
&PROP ID='T_db153_R20_Z150 props', BEAD_DIAMETER=153.3E-6, BEAD_EMISSIVITY=0.037, BEAD_DENSITY=21391, BEAD_SPECIFIC_HEAT=0.139/
&PROP ID='T_db153_R20_Z160 props', BEAD_DIAMETER=153.3E-6, BEAD_EMISSIVITY=0.032, BEAD_DENSITY=21397, BEAD_SPECIFIC_HEAT=0.139/
&PROP ID='T_db153_R20_Z170 props', BEAD_DIAMETER=153.3E-6, BEAD_EMISSIVITY=0.028, BEAD_DENSITY=21402, BEAD_SPECIFIC_HEAT=0.138/
&PROP ID='T_db153_R20_Z180 props', BEAD_DIAMETER=153.3E-6, BEAD_EMISSIVITY=0.024, BEAD_DENSITY=21407, BEAD_SPECIFIC_HEAT=0.138/
&PROP ID='T_db153_R20_Z190 props', BEAD_DIAMETER=153.3E-6, BEAD_EMISSIVITY=0.021, BEAD_DENSITY=21411, BEAD_SPECIFIC_HEAT=0.137/
&PROP ID='T_db153_R20_Z200 props', BEAD_DIAMETER=153.3E-6, BEAD_EMISSIVITY=0.018, BEAD_DENSITY=21415, BEAD_SPECIFIC_HEAT=0.137/
&PROP ID='T_db153_R20_Z210 props', BEAD_DIAMETER=153.3E-6, BEAD_EMISSIVITY=0.016, BEAD_DENSITY=21418, BEAD_SPECIFIC_HEAT=0.137/
&PROP ID='T_db153_R30_Z001 props', BEAD_DIAMETER=153.3E-6, BEAD_EMISSIVITY=0.065, BEAD_DENSITY=21347, BEAD_SPECIFIC_HEAT=0.144/
&PROP ID='T_db153_R30_Z005 props', BEAD_DIAMETER=153.3E-6, BEAD_EMISSIVITY=0.064, BEAD_DENSITY=21349, BEAD_SPECIFIC_HEAT=0.144/
&PROP ID='T_db153_R30_Z010 props', BEAD_DIAMETER=153.3E-6, BEAD_EMISSIVITY=0.063,

BEAD_DENSITY=21350, BEAD_SPECIFIC_HEAT=0.144/
&PROP ID='T_db153_R30_Z020 props', BEAD_DIAMETER=153.3E-6, BEAD_EMISSIVITY=0.060, BEAD_DENSITY=21354, BEAD_SPECIFIC_HEAT=0.143/
&PROP ID='T_db153_R30_Z030 props', BEAD_DIAMETER=153.3E-6, BEAD_EMISSIVITY=0.054, BEAD_DENSITY=21363, BEAD_SPECIFIC_HEAT=0.142/
&PROP ID='T_db153_R30_Z040 props', BEAD_DIAMETER=153.3E-6, BEAD_EMISSIVITY=0.048, BEAD_DENSITY=21371, BEAD_SPECIFIC_HEAT=0.141/
&PROP ID='T_db153_R30_Z050 props', BEAD_DIAMETER=153.3E-6, BEAD_EMISSIVITY=0.042, BEAD_DENSITY=21379, BEAD_SPECIFIC_HEAT=0.141/
&PROP ID='T_db153_R30_Z060 props', BEAD_DIAMETER=153.3E-6, BEAD_EMISSIVITY=0.037, BEAD_DENSITY=21388, BEAD_SPECIFIC_HEAT=0.140/
&PROP ID='T_db153_R30_Z070 props', BEAD_DIAMETER=153.3E-6, BEAD_EMISSIVITY=0.037, BEAD_DENSITY=21389, BEAD_SPECIFIC_HEAT=0.140/
&PROP ID='T_db153_R30_Z080 props', BEAD_DIAMETER=153.3E-6, BEAD_EMISSIVITY=0.036, BEAD_DENSITY=21389, BEAD_SPECIFIC_HEAT=0.140/
&PROP ID='T_db153_R30_Z090 props', BEAD_DIAMETER=153.3E-6, BEAD_EMISSIVITY=0.036, BEAD_DENSITY=21391, BEAD_SPECIFIC_HEAT=0.139/
&PROP ID='T_db153_R30_Z100 props', BEAD_DIAMETER=153.3E-6, BEAD_EMISSIVITY=0.035, BEAD_DENSITY=21392, BEAD_SPECIFIC_HEAT=0.139/
&PROP ID='T_db153_R30_Z110 props', BEAD_DIAMETER=153.3E-6, BEAD_EMISSIVITY=0.034, BEAD_DENSITY=21394, BEAD_SPECIFIC_HEAT=0.139/
&PROP ID='T_db153_R30_Z120 props', BEAD_DIAMETER=153.3E-6, BEAD_EMISSIVITY=0.033, BEAD_DENSITY=21396, BEAD_SPECIFIC_HEAT=0.139/
&PROP ID='T_db153_R30_Z130 props', BEAD_DIAMETER=153.3E-6, BEAD_EMISSIVITY=0.031, BEAD_DENSITY=21398, BEAD_SPECIFIC_HEAT=0.139/
&PROP ID='T_db153_R30_Z140 props', BEAD_DIAMETER=153.3E-6, BEAD_EMISSIVITY=0.029, BEAD_DENSITY=21401, BEAD_SPECIFIC_HEAT=0.138/
&PROP ID='T_db153_R30_Z150 props', BEAD_DIAMETER=153.3E-6, BEAD_EMISSIVITY=0.025, BEAD_DENSITY=21406, BEAD_SPECIFIC_HEAT=0.138/
&PROP ID='T_db153_R30_Z160 props', BEAD_DIAMETER=153.3E-6, BEAD_EMISSIVITY=0.021, BEAD_DENSITY=21410, BEAD_SPECIFIC_HEAT=0.137/
&PROP ID='T_db153_R30_Z170 props', BEAD_DIAMETER=153.3E-6, BEAD_EMISSIVITY=0.017, BEAD_DENSITY=21415, BEAD_SPECIFIC_HEAT=0.137/
&PROP ID='T_db153_R30_Z180 props', BEAD_DIAMETER=153.3E-6, BEAD_EMISSIVITY=0.013, BEAD_DENSITY=21420, BEAD_SPECIFIC_HEAT=0.137/
&PROP ID='T_db153_R30_Z190 props', BEAD_DIAMETER=153.3E-6, BEAD_EMISSIVITY=0.012, BEAD_DENSITY=21422, BEAD_SPECIFIC_HEAT=0.136/
&PROP ID='T_db153_R30_Z200 props', BEAD_DIAMETER=153.3E-6, BEAD_EMISSIVITY=0.010, BEAD_DENSITY=21424, BEAD_SPECIFIC_HEAT=0.136/
&PROP ID='T_db153_R30_Z210 props', BEAD_DIAMETER=153.3E-6, BEAD_EMISSIVITY=0.009, BEAD_DENSITY=21426, BEAD_SPECIFIC_HEAT=0.136/
&PROP ID='T_db153_R40_Z001 props', BEAD_DIAMETER=153.3E-6, BEAD_EMISSIVITY=0.031, BEAD_DENSITY=21398, BEAD_SPECIFIC_HEAT=0.139/
&PROP ID='T_db153_R40_Z005 props', BEAD_DIAMETER=153.3E-6, BEAD_EMISSIVITY=0.029, BEAD_DENSITY=21400, BEAD_SPECIFIC_HEAT=0.139/
&PROP ID='T_db153_R40_Z010 props', BEAD_DIAMETER=153.3E-6, BEAD_EMISSIVITY=0.026,

BEAD_DENSITY=21402, BEAD_SPECIFIC_HEAT=0.138/
&PROP ID='T_db153_R40_Z020 props', BEAD_DIAMETER=153.3E-6, BEAD_EMISSIVITY=0.020,
BEAD_DENSITY=21407, BEAD_SPECIFIC_HEAT=0.138/
&PROP ID='T_db153_R40_Z030 props', BEAD_DIAMETER=153.3E-6, BEAD_EMISSIVITY=0.020,
BEAD_DENSITY=21409, BEAD_SPECIFIC_HEAT=0.138/
&PROP ID='T_db153_R40_Z040 props', BEAD_DIAMETER=153.3E-6, BEAD_EMISSIVITY=0.019,
BEAD_DENSITY=21411, BEAD_SPECIFIC_HEAT=0.137/
&PROP ID='T_db153_R40_Z050 props', BEAD_DIAMETER=153.3E-6, BEAD_EMISSIVITY=0.018,
BEAD_DENSITY=21412, BEAD_SPECIFIC_HEAT=0.137/
&PROP ID='T_db153_R40_Z060 props', BEAD_DIAMETER=153.3E-6, BEAD_EMISSIVITY=0.018,
BEAD_DENSITY=21412, BEAD_SPECIFIC_HEAT=0.137/
&PROP ID='T_db153_R40_Z070 props', BEAD_DIAMETER=153.3E-6, BEAD_EMISSIVITY=0.017,
BEAD_DENSITY=21413, BEAD_SPECIFIC_HEAT=0.137/
&PROP ID='T_db153_R40_Z080 props', BEAD_DIAMETER=153.3E-6, BEAD_EMISSIVITY=0.017,
BEAD_DENSITY=21413, BEAD_SPECIFIC_HEAT=0.137/
&PROP ID='T_db153_R40_Z090 props', BEAD_DIAMETER=153.3E-6, BEAD_EMISSIVITY=0.018,
BEAD_DENSITY=21413, BEAD_SPECIFIC_HEAT=0.137/
&PROP ID='T_db153_R40_Z100 props', BEAD_DIAMETER=153.3E-6, BEAD_EMISSIVITY=0.018,
BEAD_DENSITY=21413, BEAD_SPECIFIC_HEAT=0.137/
&PROP ID='T_db153_R40_Z110 props', BEAD_DIAMETER=153.3E-6, BEAD_EMISSIVITY=0.018,
BEAD_DENSITY=21413, BEAD_SPECIFIC_HEAT=0.137/
&PROP ID='T_db153_R40_Z120 props', BEAD_DIAMETER=153.3E-6, BEAD_EMISSIVITY=0.018,
BEAD_DENSITY=21414, BEAD_SPECIFIC_HEAT=0.137/
&PROP ID='T_db153_R40_Z130 props', BEAD_DIAMETER=153.3E-6, BEAD_EMISSIVITY=0.017,
BEAD_DENSITY=21415, BEAD_SPECIFIC_HEAT=0.137/
&PROP ID='T_db153_R40_Z140 props', BEAD_DIAMETER=153.3E-6, BEAD_EMISSIVITY=0.016,
BEAD_DENSITY=21416, BEAD_SPECIFIC_HEAT=0.137/
&PROP ID='T_db153_R40_Z150 props', BEAD_DIAMETER=153.3E-6, BEAD_EMISSIVITY=0.014,
BEAD_DENSITY=21418, BEAD_SPECIFIC_HEAT=0.137/
&PROP ID='T_db153_R40_Z160 props', BEAD_DIAMETER=153.3E-6, BEAD_EMISSIVITY=0.012,
BEAD_DENSITY=21420, BEAD_SPECIFIC_HEAT=0.136/
&PROP ID='T_db153_R40_Z170 props', BEAD_DIAMETER=153.3E-6, BEAD_EMISSIVITY=0.010,
BEAD_DENSITY=21423, BEAD_SPECIFIC_HEAT=0.136/
&PROP ID='T_db153_R40_Z180 props', BEAD_DIAMETER=153.3E-6, BEAD_EMISSIVITY=0.009,
BEAD_DENSITY=21425, BEAD_SPECIFIC_HEAT=0.136/
&PROP ID='T_db153_R40_Z190 props', BEAD_DIAMETER=153.3E-6, BEAD_EMISSIVITY=0.007,
BEAD_DENSITY=21428, BEAD_SPECIFIC_HEAT=0.136/
&PROP ID='T_db153_R40_Z200 props', BEAD_DIAMETER=153.3E-6, BEAD_EMISSIVITY=0.005,
BEAD_DENSITY=21430, BEAD_SPECIFIC_HEAT=0.135/
&PROP ID='T_db153_R40_Z210 props', BEAD_DIAMETER=153.3E-6, BEAD_EMISSIVITY=0.003,
BEAD_DENSITY=21432, BEAD_SPECIFIC_HEAT=0.135/
&PROP ID='T_db153_R50_Z001 props', BEAD_DIAMETER=153.3E-6, BEAD_EMISSIVITY=0.019,
BEAD_DENSITY=21434, BEAD_SPECIFIC_HEAT=0.135/
&PROP ID='T_db153_R50_Z005 props', BEAD_DIAMETER=153.3E-6, BEAD_EMISSIVITY=0.017,
BEAD_DENSITY=21437, BEAD_SPECIFIC_HEAT=0.135/
&PROP ID='T_db153_R50_Z010 props', BEAD_DIAMETER=153.3E-6, BEAD_EMISSIVITY=0.016,

BEAD_DENSITY=21441, BEAD_SPECIFIC_HEAT=0.134/
&PROP ID='T_db153_R50_Z020 props', BEAD_DIAMETER=153.3E-6, BEAD_EMISSIVITY=0.013, BEAD_DENSITY=21448, BEAD_SPECIFIC_HEAT=0.134/
&PROP ID='T_db153_R50_Z030 props', BEAD_DIAMETER=153.3E-6, BEAD_EMISSIVITY=0.010, BEAD_DENSITY=21445, BEAD_SPECIFIC_HEAT=0.134/
&PROP ID='T_db153_R50_Z040 props', BEAD_DIAMETER=153.3E-6, BEAD_EMISSIVITY=0.008, BEAD_DENSITY=21443, BEAD_SPECIFIC_HEAT=0.134/
&PROP ID='T_db153_R50_Z050 props', BEAD_DIAMETER=153.3E-6, BEAD_EMISSIVITY=0.006, BEAD_DENSITY=21441, BEAD_SPECIFIC_HEAT=0.134/
&PROP ID='T_db153_R50_Z060 props', BEAD_DIAMETER=153.3E-6, BEAD_EMISSIVITY=0.005, BEAD_DENSITY=21439, BEAD_SPECIFIC_HEAT=0.135/
&PROP ID='T_db153_R50_Z070 props', BEAD_DIAMETER=153.3E-6, BEAD_EMISSIVITY=0.005, BEAD_DENSITY=21436, BEAD_SPECIFIC_HEAT=0.135/
&PROP ID='T_db153_R50_Z080 props', BEAD_DIAMETER=153.3E-6, BEAD_EMISSIVITY=0.005, BEAD_DENSITY=21433, BEAD_SPECIFIC_HEAT=0.135/
&PROP ID='T_db153_R50_Z090 props', BEAD_DIAMETER=153.3E-6, BEAD_EMISSIVITY=0.005, BEAD_DENSITY=21431, BEAD_SPECIFIC_HEAT=0.135/
&PROP ID='T_db153_R50_Z100 props', BEAD_DIAMETER=153.3E-6, BEAD_EMISSIVITY=0.005, BEAD_DENSITY=21428, BEAD_SPECIFIC_HEAT=0.136/
&PROP ID='T_db153_R50_Z110 props', BEAD_DIAMETER=153.3E-6, BEAD_EMISSIVITY=0.006, BEAD_DENSITY=21427, BEAD_SPECIFIC_HEAT=0.136/
&PROP ID='T_db153_R50_Z120 props', BEAD_DIAMETER=153.3E-6, BEAD_EMISSIVITY=0.007, BEAD_DENSITY=21427, BEAD_SPECIFIC_HEAT=0.136/
&PROP ID='T_db153_R50_Z130 props', BEAD_DIAMETER=153.3E-6, BEAD_EMISSIVITY=0.007, BEAD_DENSITY=21426, BEAD_SPECIFIC_HEAT=0.136/
&PROP ID='T_db153_R50_Z140 props', BEAD_DIAMETER=153.3E-6, BEAD_EMISSIVITY=0.008, BEAD_DENSITY=21425, BEAD_SPECIFIC_HEAT=0.136/
&PROP ID='T_db153_R50_Z150 props', BEAD_DIAMETER=153.3E-6, BEAD_EMISSIVITY=0.006, BEAD_DENSITY=21428, BEAD_SPECIFIC_HEAT=0.136/
&PROP ID='T_db153_R50_Z160 props', BEAD_DIAMETER=153.3E-6, BEAD_EMISSIVITY=0.005, BEAD_DENSITY=21430, BEAD_SPECIFIC_HEAT=0.135/
&PROP ID='T_db153_R50_Z170 props', BEAD_DIAMETER=153.3E-6, BEAD_EMISSIVITY=0.003, BEAD_DENSITY=21433, BEAD_SPECIFIC_HEAT=0.135/
&PROP ID='T_db153_R50_Z180 props', BEAD_DIAMETER=153.3E-6, BEAD_EMISSIVITY=0.001, BEAD_DENSITY=21435, BEAD_SPECIFIC_HEAT=0.135/
&PROP ID='T_db153_R50_Z190 props', BEAD_DIAMETER=153.3E-6, BEAD_EMISSIVITY=0.001, BEAD_DENSITY=21437, BEAD_SPECIFIC_HEAT=0.135/
&PROP ID='T_db153_R50_Z200 props', BEAD_DIAMETER=153.3E-6, BEAD_EMISSIVITY=0.001, BEAD_DENSITY=21438, BEAD_SPECIFIC_HEAT=0.135/
&PROP ID='T_db153_R50_Z210 props', BEAD_DIAMETER=153.3E-6, BEAD_EMISSIVITY=0.001, BEAD_DENSITY=21440, BEAD_SPECIFIC_HEAT=0.135/

&DEVC ID='T_db153_R00_Z001', PROP_ID='T_db153_R00_Z001 props', QUANTITY='THERMOCOUPLE', XYZ=0.0,0.0,0.02, CONVERSION_ADDEND=273.15, UNITS='K'/
&DEVC ID='T_db153_R00_Z005', PROP_ID='T_db153_R00_Z005 props', QUANTITY='THERMOCOUPLE', XYZ=0.0,0.0,0.06, CONVERSION_ADDEND=273.15, UNITS='K'/
&DEVC ID='T_db153_R00_Z010', PROP_ID='T_db153_R00_Z010 props',

QUANTITY='THERMOCOUPLE', XYZ=0.0,0.0,0.11, CONVERSION_ADDEND=273.15, UNITS='K'/
&DEVC ID='T_db153_R00_Z020', PROP_ID='T_db153_R00_Z020 props',
QUANTITY='THERMOCOUPLE', XYZ=0.0,0.0,0.21, CONVERSION_ADDEND=273.15, UNITS='K'/
&DEVC ID='T_db153_R00_Z030', PROP_ID='T_db153_R00_Z030 props',
QUANTITY='THERMOCOUPLE', XYZ=0.0,0.0,0.31, CONVERSION_ADDEND=273.15, UNITS='K'/
&DEVC ID='T_db153_R00_Z040', PROP_ID='T_db153_R00_Z040 props',
QUANTITY='THERMOCOUPLE', XYZ=0.0,0.0,0.41, CONVERSION_ADDEND=273.15, UNITS='K'/
&DEVC ID='T_db153_R00_Z050', PROP_ID='T_db153_R00_Z050 props',
QUANTITY='THERMOCOUPLE', XYZ=0.0,0.0,0.51, CONVERSION_ADDEND=273.15, UNITS='K'/
&DEVC ID='T_db153_R00_Z060', PROP_ID='T_db153_R00_Z060 props',
QUANTITY='THERMOCOUPLE', XYZ=0.0,0.0,0.61, CONVERSION_ADDEND=273.15, UNITS='K'/
&DEVC ID='T_db153_R00_Z070', PROP_ID='T_db153_R00_Z070 props',
QUANTITY='THERMOCOUPLE', XYZ=0.0,0.0,0.71, CONVERSION_ADDEND=273.15, UNITS='K'/
&DEVC ID='T_db153_R00_Z080', PROP_ID='T_db153_R00_Z080 props',
QUANTITY='THERMOCOUPLE', XYZ=0.0,0.0,0.81, CONVERSION_ADDEND=273.15, UNITS='K'/
&DEVC ID='T_db153_R00_Z090', PROP_ID='T_db153_R00_Z090 props',
QUANTITY='THERMOCOUPLE', XYZ=0.0,0.0,0.91, CONVERSION_ADDEND=273.15, UNITS='K'/
&DEVC ID='T_db153_R00_Z100', PROP_ID='T_db153_R00_Z100 props',
QUANTITY='THERMOCOUPLE', XYZ=0.0,0.0,1.01, CONVERSION_ADDEND=273.15, UNITS='K'/
&DEVC ID='T_db153_R00_Z110', PROP_ID='T_db153_R00_Z110 props',
QUANTITY='THERMOCOUPLE', XYZ=0.0,0.0,1.11, CONVERSION_ADDEND=273.15, UNITS='K'/
&DEVC ID='T_db153_R00_Z120', PROP_ID='T_db153_R00_Z120 props',
QUANTITY='THERMOCOUPLE', XYZ=0.0,0.0,1.21, CONVERSION_ADDEND=273.15, UNITS='K'/
&DEVC ID='T_db153_R00_Z130', PROP_ID='T_db153_R00_Z130 props',
QUANTITY='THERMOCOUPLE', XYZ=0.0,0.0,1.31, CONVERSION_ADDEND=273.15, UNITS='K'/
&DEVC ID='T_db153_R00_Z140', PROP_ID='T_db153_R00_Z140 props',
QUANTITY='THERMOCOUPLE', XYZ=0.0,0.0,1.41, CONVERSION_ADDEND=273.15, UNITS='K'/
&DEVC ID='T_db153_R00_Z150', PROP_ID='T_db153_R00_Z150 props',
QUANTITY='THERMOCOUPLE', XYZ=0.0,0.0,1.51, CONVERSION_ADDEND=273.15, UNITS='K'/
&DEVC ID='T_db153_R00_Z160', PROP_ID='T_db153_R00_Z160 props',
QUANTITY='THERMOCOUPLE', XYZ=0.0,0.0,1.61, CONVERSION_ADDEND=273.15, UNITS='K'/
&DEVC ID='T_db153_R00_Z170', PROP_ID='T_db153_R00_Z170 props',
QUANTITY='THERMOCOUPLE', XYZ=0.0,0.0,1.71, CONVERSION_ADDEND=273.15, UNITS='K'/
&DEVC ID='T_db153_R00_Z180', PROP_ID='T_db153_R00_Z180 props',
QUANTITY='THERMOCOUPLE', XYZ=0.0,0.0,1.81, CONVERSION_ADDEND=273.15, UNITS='K'/
&DEVC ID='T_db153_R00_Z190', PROP_ID='T_db153_R00_Z190 props',
QUANTITY='THERMOCOUPLE', XYZ=0.0,0.0,1.91, CONVERSION_ADDEND=273.15, UNITS='K'/
&DEVC ID='T_db153_R00_Z200', PROP_ID='T_db153_R00_Z200 props',
QUANTITY='THERMOCOUPLE', XYZ=0.0,0.0,2.01, CONVERSION_ADDEND=273.15, UNITS='K'/
&DEVC ID='T_db153_R00_Z210', PROP_ID='T_db153_R00_Z210 props',
QUANTITY='THERMOCOUPLE', XYZ=0.0,0.0,2.11, CONVERSION_ADDEND=273.15, UNITS='K'/
&DEVC ID='T_db153_R10_Z001', PROP_ID='T_db153_R10_Z001 props',
QUANTITY='THERMOCOUPLE', XYZ=0.1,0.0,0.02, CONVERSION_ADDEND=273.15, UNITS='K'/
&DEVC ID='T_db153_R10_Z005', PROP_ID='T_db153_R10_Z005 props',
QUANTITY='THERMOCOUPLE', XYZ=0.1,0.0,0.06, CONVERSION_ADDEND=273.15, UNITS='K'/
&DEVC ID='T_db153_R10_Z010', PROP_ID='T_db153_R10_Z010 props',

QUANTITY='THERMOCOUPLE', XYZ=0.1,0.0,0.11, CONVERSION_ADDEND=273.15, UNITS='K'/
&DEVC ID='T_db153_R10_Z020', PROP_ID='T_db153_R10_Z020 props',
QUANTITY='THERMOCOUPLE', XYZ=0.1,0.0,0.21, CONVERSION_ADDEND=273.15, UNITS='K'/
&DEVC ID='T_db153_R10_Z030', PROP_ID='T_db153_R10_Z030 props',
QUANTITY='THERMOCOUPLE', XYZ=0.1,0.0,0.31, CONVERSION_ADDEND=273.15, UNITS='K'/
&DEVC ID='T_db153_R10_Z040', PROP_ID='T_db153_R10_Z040 props',
QUANTITY='THERMOCOUPLE', XYZ=0.1,0.0,0.41, CONVERSION_ADDEND=273.15, UNITS='K'/
&DEVC ID='T_db153_R10_Z050', PROP_ID='T_db153_R10_Z050 props',
QUANTITY='THERMOCOUPLE', XYZ=0.1,0.0,0.51, CONVERSION_ADDEND=273.15, UNITS='K'/
&DEVC ID='T_db153_R10_Z060', PROP_ID='T_db153_R10_Z060 props',
QUANTITY='THERMOCOUPLE', XYZ=0.1,0.0,0.61, CONVERSION_ADDEND=273.15, UNITS='K'/
&DEVC ID='T_db153_R10_Z070', PROP_ID='T_db153_R10_Z070 props',
QUANTITY='THERMOCOUPLE', XYZ=0.1,0.0,0.71, CONVERSION_ADDEND=273.15, UNITS='K'/
&DEVC ID='T_db153_R10_Z080', PROP_ID='T_db153_R10_Z080 props',
QUANTITY='THERMOCOUPLE', XYZ=0.1,0.0,0.81, CONVERSION_ADDEND=273.15, UNITS='K'/
&DEVC ID='T_db153_R10_Z090', PROP_ID='T_db153_R10_Z090 props',
QUANTITY='THERMOCOUPLE', XYZ=0.1,0.0,0.91, CONVERSION_ADDEND=273.15, UNITS='K'/
&DEVC ID='T_db153_R10_Z100', PROP_ID='T_db153_R10_Z100 props',
QUANTITY='THERMOCOUPLE', XYZ=0.1,0.0,1.01, CONVERSION_ADDEND=273.15, UNITS='K'/
&DEVC ID='T_db153_R10_Z110', PROP_ID='T_db153_R10_Z110 props',
QUANTITY='THERMOCOUPLE', XYZ=0.1,0.0,1.11, CONVERSION_ADDEND=273.15, UNITS='K'/
&DEVC ID='T_db153_R10_Z120', PROP_ID='T_db153_R10_Z120 props',
QUANTITY='THERMOCOUPLE', XYZ=0.1,0.0,1.21, CONVERSION_ADDEND=273.15, UNITS='K'/
&DEVC ID='T_db153_R10_Z130', PROP_ID='T_db153_R10_Z130 props',
QUANTITY='THERMOCOUPLE', XYZ=0.1,0.0,1.31, CONVERSION_ADDEND=273.15, UNITS='K'/
&DEVC ID='T_db153_R10_Z140', PROP_ID='T_db153_R10_Z140 props',
QUANTITY='THERMOCOUPLE', XYZ=0.1,0.0,1.41, CONVERSION_ADDEND=273.15, UNITS='K'/
&DEVC ID='T_db153_R10_Z150', PROP_ID='T_db153_R10_Z150 props',
QUANTITY='THERMOCOUPLE', XYZ=0.1,0.0,1.51, CONVERSION_ADDEND=273.15, UNITS='K'/
&DEVC ID='T_db153_R10_Z160', PROP_ID='T_db153_R10_Z160 props',
QUANTITY='THERMOCOUPLE', XYZ=0.1,0.0,1.61, CONVERSION_ADDEND=273.15, UNITS='K'/
&DEVC ID='T_db153_R10_Z170', PROP_ID='T_db153_R10_Z170 props',
QUANTITY='THERMOCOUPLE', XYZ=0.1,0.0,1.71, CONVERSION_ADDEND=273.15, UNITS='K'/
&DEVC ID='T_db153_R10_Z180', PROP_ID='T_db153_R10_Z180 props',
QUANTITY='THERMOCOUPLE', XYZ=0.1,0.0,1.81, CONVERSION_ADDEND=273.15, UNITS='K'/
&DEVC ID='T_db153_R10_Z190', PROP_ID='T_db153_R10_Z190 props',
QUANTITY='THERMOCOUPLE', XYZ=0.1,0.0,1.91, CONVERSION_ADDEND=273.15, UNITS='K'/
&DEVC ID='T_db153_R10_Z200', PROP_ID='T_db153_R10_Z200 props',
QUANTITY='THERMOCOUPLE', XYZ=0.1,0.0,2.01, CONVERSION_ADDEND=273.15, UNITS='K'/
&DEVC ID='T_db153_R10_Z210', PROP_ID='T_db153_R10_Z210 props',
QUANTITY='THERMOCOUPLE', XYZ=0.1,0.0,2.11, CONVERSION_ADDEND=273.15, UNITS='K'/
&DEVC ID='T_db153_R20_Z001', PROP_ID='T_db153_R20_Z001 props',
QUANTITY='THERMOCOUPLE', XYZ=0.2,0.0,0.02, CONVERSION_ADDEND=273.15, UNITS='K'/
&DEVC ID='T_db153_R20_Z005', PROP_ID='T_db153_R20_Z005 props',
QUANTITY='THERMOCOUPLE', XYZ=0.2,0.0,0.06, CONVERSION_ADDEND=273.15, UNITS='K'/
&DEVC ID='T_db153_R20_Z010', PROP_ID='T_db153_R20_Z010 props',

QUANTITY='THERMOCOUPLE', XYZ=0.2,0.0,0.11, CONVERSION_ADDEND=273.15, UNITS='K'/
&DEVC ID='T_db153_R20_Z020', PROP_ID='T_db153_R20_Z020 props',
QUANTITY='THERMOCOUPLE', XYZ=0.2,0.0,0.21, CONVERSION_ADDEND=273.15, UNITS='K'/
&DEVC ID='T_db153_R20_Z030', PROP_ID='T_db153_R20_Z030 props',
QUANTITY='THERMOCOUPLE', XYZ=0.2,0.0,0.31, CONVERSION_ADDEND=273.15, UNITS='K'/
&DEVC ID='T_db153_R20_Z040', PROP_ID='T_db153_R20_Z040 props',
QUANTITY='THERMOCOUPLE', XYZ=0.2,0.0,0.41, CONVERSION_ADDEND=273.15, UNITS='K'/
&DEVC ID='T_db153_R20_Z050', PROP_ID='T_db153_R20_Z050 props',
QUANTITY='THERMOCOUPLE', XYZ=0.2,0.0,0.51, CONVERSION_ADDEND=273.15, UNITS='K'/
&DEVC ID='T_db153_R20_Z060', PROP_ID='T_db153_R20_Z060 props',
QUANTITY='THERMOCOUPLE', XYZ=0.2,0.0,0.61, CONVERSION_ADDEND=273.15, UNITS='K'/
&DEVC ID='T_db153_R20_Z070', PROP_ID='T_db153_R20_Z070 props',
QUANTITY='THERMOCOUPLE', XYZ=0.2,0.0,0.71, CONVERSION_ADDEND=273.15, UNITS='K'/
&DEVC ID='T_db153_R20_Z080', PROP_ID='T_db153_R20_Z080 props',
QUANTITY='THERMOCOUPLE', XYZ=0.2,0.0,0.81, CONVERSION_ADDEND=273.15, UNITS='K'/
&DEVC ID='T_db153_R20_Z090', PROP_ID='T_db153_R20_Z090 props',
QUANTITY='THERMOCOUPLE', XYZ=0.2,0.0,0.91, CONVERSION_ADDEND=273.15, UNITS='K'/
&DEVC ID='T_db153_R20_Z100', PROP_ID='T_db153_R20_Z100 props',
QUANTITY='THERMOCOUPLE', XYZ=0.2,0.0,1.01, CONVERSION_ADDEND=273.15, UNITS='K'/
&DEVC ID='T_db153_R20_Z110', PROP_ID='T_db153_R20_Z110 props',
QUANTITY='THERMOCOUPLE', XYZ=0.2,0.0,1.11, CONVERSION_ADDEND=273.15, UNITS='K'/
&DEVC ID='T_db153_R20_Z120', PROP_ID='T_db153_R20_Z120 props',
QUANTITY='THERMOCOUPLE', XYZ=0.2,0.0,1.21, CONVERSION_ADDEND=273.15, UNITS='K'/
&DEVC ID='T_db153_R20_Z130', PROP_ID='T_db153_R20_Z130 props',
QUANTITY='THERMOCOUPLE', XYZ=0.2,0.0,1.31, CONVERSION_ADDEND=273.15, UNITS='K'/
&DEVC ID='T_db153_R20_Z140', PROP_ID='T_db153_R20_Z140 props',
QUANTITY='THERMOCOUPLE', XYZ=0.2,0.0,1.41, CONVERSION_ADDEND=273.15, UNITS='K'/
&DEVC ID='T_db153_R20_Z150', PROP_ID='T_db153_R20_Z150 props',
QUANTITY='THERMOCOUPLE', XYZ=0.2,0.0,1.51, CONVERSION_ADDEND=273.15, UNITS='K'/
&DEVC ID='T_db153_R20_Z160', PROP_ID='T_db153_R20_Z160 props',
QUANTITY='THERMOCOUPLE', XYZ=0.2,0.0,1.61, CONVERSION_ADDEND=273.15, UNITS='K'/
&DEVC ID='T_db153_R20_Z170', PROP_ID='T_db153_R20_Z170 props',
QUANTITY='THERMOCOUPLE', XYZ=0.2,0.0,1.71, CONVERSION_ADDEND=273.15, UNITS='K'/
&DEVC ID='T_db153_R20_Z180', PROP_ID='T_db153_R20_Z180 props',
QUANTITY='THERMOCOUPLE', XYZ=0.2,0.0,1.81, CONVERSION_ADDEND=273.15, UNITS='K'/
&DEVC ID='T_db153_R20_Z190', PROP_ID='T_db153_R20_Z190 props',
QUANTITY='THERMOCOUPLE', XYZ=0.2,0.0,1.91, CONVERSION_ADDEND=273.15, UNITS='K'/
&DEVC ID='T_db153_R20_Z200', PROP_ID='T_db153_R20_Z200 props',
QUANTITY='THERMOCOUPLE', XYZ=0.2,0.0,2.01, CONVERSION_ADDEND=273.15, UNITS='K'/
&DEVC ID='T_db153_R20_Z210', PROP_ID='T_db153_R20_Z210 props',
QUANTITY='THERMOCOUPLE', XYZ=0.2,0.0,2.11, CONVERSION_ADDEND=273.15, UNITS='K'/
&DEVC ID='T_db153_R30_Z001', PROP_ID='T_db153_R30_Z001 props',
QUANTITY='THERMOCOUPLE', XYZ=0.3,0.0,0.02, CONVERSION_ADDEND=273.15, UNITS='K'/
&DEVC ID='T_db153_R30_Z005', PROP_ID='T_db153_R30_Z005 props',
QUANTITY='THERMOCOUPLE', XYZ=0.3,0.0,0.06, CONVERSION_ADDEND=273.15, UNITS='K'/
&DEVC ID='T_db153_R30_Z010', PROP_ID='T_db153_R30_Z010 props',

QUANTITY='THERMOCOUPLE', XYZ=0.3,0.0,0.11, CONVERSION_ADDEND=273.15, UNITS='K'/
&DEVC ID='T_db153_R30_Z020', PROP_ID='T_db153_R30_Z020 props',
QUANTITY='THERMOCOUPLE', XYZ=0.3,0.0,0.21, CONVERSION_ADDEND=273.15, UNITS='K'/
&DEVC ID='T_db153_R30_Z030', PROP_ID='T_db153_R30_Z030 props',
QUANTITY='THERMOCOUPLE', XYZ=0.3,0.0,0.31, CONVERSION_ADDEND=273.15, UNITS='K'/
&DEVC ID='T_db153_R30_Z040', PROP_ID='T_db153_R30_Z040 props',
QUANTITY='THERMOCOUPLE', XYZ=0.3,0.0,0.41, CONVERSION_ADDEND=273.15, UNITS='K'/
&DEVC ID='T_db153_R30_Z050', PROP_ID='T_db153_R30_Z050 props',
QUANTITY='THERMOCOUPLE', XYZ=0.3,0.0,0.51, CONVERSION_ADDEND=273.15, UNITS='K'/
&DEVC ID='T_db153_R30_Z060', PROP_ID='T_db153_R30_Z060 props',
QUANTITY='THERMOCOUPLE', XYZ=0.3,0.0,0.61, CONVERSION_ADDEND=273.15, UNITS='K'/
&DEVC ID='T_db153_R30_Z070', PROP_ID='T_db153_R30_Z070 props',
QUANTITY='THERMOCOUPLE', XYZ=0.3,0.0,0.71, CONVERSION_ADDEND=273.15, UNITS='K'/
&DEVC ID='T_db153_R30_Z080', PROP_ID='T_db153_R30_Z080 props',
QUANTITY='THERMOCOUPLE', XYZ=0.3,0.0,0.81, CONVERSION_ADDEND=273.15, UNITS='K'/
&DEVC ID='T_db153_R30_Z090', PROP_ID='T_db153_R30_Z090 props',
QUANTITY='THERMOCOUPLE', XYZ=0.3,0.0,0.91, CONVERSION_ADDEND=273.15, UNITS='K'/
&DEVC ID='T_db153_R30_Z100', PROP_ID='T_db153_R30_Z100 props',
QUANTITY='THERMOCOUPLE', XYZ=0.3,0.0,1.01, CONVERSION_ADDEND=273.15, UNITS='K'/
&DEVC ID='T_db153_R30_Z110', PROP_ID='T_db153_R30_Z110 props',
QUANTITY='THERMOCOUPLE', XYZ=0.3,0.0,1.11, CONVERSION_ADDEND=273.15, UNITS='K'/
&DEVC ID='T_db153_R30_Z120', PROP_ID='T_db153_R30_Z120 props',
QUANTITY='THERMOCOUPLE', XYZ=0.3,0.0,1.21, CONVERSION_ADDEND=273.15, UNITS='K'/
&DEVC ID='T_db153_R30_Z130', PROP_ID='T_db153_R30_Z130 props',
QUANTITY='THERMOCOUPLE', XYZ=0.3,0.0,1.31, CONVERSION_ADDEND=273.15, UNITS='K'/
&DEVC ID='T_db153_R30_Z140', PROP_ID='T_db153_R30_Z140 props',
QUANTITY='THERMOCOUPLE', XYZ=0.3,0.0,1.41, CONVERSION_ADDEND=273.15, UNITS='K'/
&DEVC ID='T_db153_R30_Z150', PROP_ID='T_db153_R30_Z150 props',
QUANTITY='THERMOCOUPLE', XYZ=0.3,0.0,1.51, CONVERSION_ADDEND=273.15, UNITS='K'/
&DEVC ID='T_db153_R30_Z160', PROP_ID='T_db153_R30_Z160 props',
QUANTITY='THERMOCOUPLE', XYZ=0.3,0.0,1.61, CONVERSION_ADDEND=273.15, UNITS='K'/
&DEVC ID='T_db153_R30_Z170', PROP_ID='T_db153_R30_Z170 props',
QUANTITY='THERMOCOUPLE', XYZ=0.3,0.0,1.71, CONVERSION_ADDEND=273.15, UNITS='K'/
&DEVC ID='T_db153_R30_Z180', PROP_ID='T_db153_R30_Z180 props',
QUANTITY='THERMOCOUPLE', XYZ=0.3,0.0,1.81, CONVERSION_ADDEND=273.15, UNITS='K'/
&DEVC ID='T_db153_R30_Z190', PROP_ID='T_db153_R30_Z190 props',
QUANTITY='THERMOCOUPLE', XYZ=0.3,0.0,1.91, CONVERSION_ADDEND=273.15, UNITS='K'/
&DEVC ID='T_db153_R30_Z200', PROP_ID='T_db153_R30_Z200 props',
QUANTITY='THERMOCOUPLE', XYZ=0.3,0.0,2.01, CONVERSION_ADDEND=273.15, UNITS='K'/
&DEVC ID='T_db153_R30_Z210', PROP_ID='T_db153_R30_Z210 props',
QUANTITY='THERMOCOUPLE', XYZ=0.3,0.0,2.11, CONVERSION_ADDEND=273.15, UNITS='K'/
&DEVC ID='T_db153_R40_Z001', PROP_ID='T_db153_R40_Z001 props',
QUANTITY='THERMOCOUPLE', XYZ=0.4,0.0,0.02, CONVERSION_ADDEND=273.15, UNITS='K'/
&DEVC ID='T_db153_R40_Z005', PROP_ID='T_db153_R40_Z005 props',
QUANTITY='THERMOCOUPLE', XYZ=0.4,0.0,0.06, CONVERSION_ADDEND=273.15, UNITS='K'/
&DEVC ID='T_db153_R40_Z010', PROP_ID='T_db153_R40_Z010 props',

QUANTITY='THERMOCOUPLE', XYZ=0.4,0.0,0.11, CONVERSION_ADDEND=273.15, UNITS='K'/
&DEVC ID='T_db153_R40_Z020', PROP_ID='T_db153_R40_Z020 props',
QUANTITY='THERMOCOUPLE', XYZ=0.4,0.0,0.21, CONVERSION_ADDEND=273.15, UNITS='K'/
&DEVC ID='T_db153_R40_Z030', PROP_ID='T_db153_R40_Z030 props',
QUANTITY='THERMOCOUPLE', XYZ=0.4,0.0,0.31, CONVERSION_ADDEND=273.15, UNITS='K'/
&DEVC ID='T_db153_R40_Z040', PROP_ID='T_db153_R40_Z040 props',
QUANTITY='THERMOCOUPLE', XYZ=0.4,0.0,0.41, CONVERSION_ADDEND=273.15, UNITS='K'/
&DEVC ID='T_db153_R40_Z050', PROP_ID='T_db153_R40_Z050 props',
QUANTITY='THERMOCOUPLE', XYZ=0.4,0.0,0.51, CONVERSION_ADDEND=273.15, UNITS='K'/
&DEVC ID='T_db153_R40_Z060', PROP_ID='T_db153_R40_Z060 props',
QUANTITY='THERMOCOUPLE', XYZ=0.4,0.0,0.61, CONVERSION_ADDEND=273.15, UNITS='K'/
&DEVC ID='T_db153_R40_Z070', PROP_ID='T_db153_R40_Z070 props',
QUANTITY='THERMOCOUPLE', XYZ=0.4,0.0,0.71, CONVERSION_ADDEND=273.15, UNITS='K'/
&DEVC ID='T_db153_R40_Z080', PROP_ID='T_db153_R40_Z080 props',
QUANTITY='THERMOCOUPLE', XYZ=0.4,0.0,0.81, CONVERSION_ADDEND=273.15, UNITS='K'/
&DEVC ID='T_db153_R40_Z090', PROP_ID='T_db153_R40_Z090 props',
QUANTITY='THERMOCOUPLE', XYZ=0.4,0.0,0.91, CONVERSION_ADDEND=273.15, UNITS='K'/
&DEVC ID='T_db153_R40_Z100', PROP_ID='T_db153_R40_Z100 props',
QUANTITY='THERMOCOUPLE', XYZ=0.4,0.0,1.01, CONVERSION_ADDEND=273.15, UNITS='K'/
&DEVC ID='T_db153_R40_Z110', PROP_ID='T_db153_R40_Z110 props',
QUANTITY='THERMOCOUPLE', XYZ=0.4,0.0,1.11, CONVERSION_ADDEND=273.15, UNITS='K'/
&DEVC ID='T_db153_R40_Z120', PROP_ID='T_db153_R40_Z120 props',
QUANTITY='THERMOCOUPLE', XYZ=0.4,0.0,1.21, CONVERSION_ADDEND=273.15, UNITS='K'/
&DEVC ID='T_db153_R40_Z130', PROP_ID='T_db153_R40_Z130 props',
QUANTITY='THERMOCOUPLE', XYZ=0.4,0.0,1.31, CONVERSION_ADDEND=273.15, UNITS='K'/
&DEVC ID='T_db153_R40_Z140', PROP_ID='T_db153_R40_Z140 props',
QUANTITY='THERMOCOUPLE', XYZ=0.4,0.0,1.41, CONVERSION_ADDEND=273.15, UNITS='K'/
&DEVC ID='T_db153_R40_Z150', PROP_ID='T_db153_R40_Z150 props',
QUANTITY='THERMOCOUPLE', XYZ=0.4,0.0,1.51, CONVERSION_ADDEND=273.15, UNITS='K'/
&DEVC ID='T_db153_R40_Z160', PROP_ID='T_db153_R40_Z160 props',
QUANTITY='THERMOCOUPLE', XYZ=0.4,0.0,1.61, CONVERSION_ADDEND=273.15, UNITS='K'/
&DEVC ID='T_db153_R40_Z170', PROP_ID='T_db153_R40_Z170 props',
QUANTITY='THERMOCOUPLE', XYZ=0.4,0.0,1.71, CONVERSION_ADDEND=273.15, UNITS='K'/
&DEVC ID='T_db153_R40_Z180', PROP_ID='T_db153_R40_Z180 props',
QUANTITY='THERMOCOUPLE', XYZ=0.4,0.0,1.81, CONVERSION_ADDEND=273.15, UNITS='K'/
&DEVC ID='T_db153_R40_Z190', PROP_ID='T_db153_R40_Z190 props',
QUANTITY='THERMOCOUPLE', XYZ=0.4,0.0,1.91, CONVERSION_ADDEND=273.15, UNITS='K'/
&DEVC ID='T_db153_R40_Z200', PROP_ID='T_db153_R40_Z200 props',
QUANTITY='THERMOCOUPLE', XYZ=0.4,0.0,2.01, CONVERSION_ADDEND=273.15, UNITS='K'/
&DEVC ID='T_db153_R40_Z210', PROP_ID='T_db153_R40_Z210 props',
QUANTITY='THERMOCOUPLE', XYZ=0.4,0.0,2.11, CONVERSION_ADDEND=273.15, UNITS='K'/
&DEVC ID='T_db153_R50_Z001', PROP_ID='T_db153_R50_Z001 props',
QUANTITY='THERMOCOUPLE', XYZ=0.5,0.0,0.02, CONVERSION_ADDEND=273.15, UNITS='K'/
&DEVC ID='T_db153_R50_Z005', PROP_ID='T_db153_R50_Z005 props',
QUANTITY='THERMOCOUPLE', XYZ=0.5,0.0,0.06, CONVERSION_ADDEND=273.15, UNITS='K'/
&DEVC ID='T_db153_R50_Z010', PROP_ID='T_db153_R50_Z010 props',

QUANTITY='THERMOCOUPLE', XYZ=0.5,0.0,0.11, CONVERSION_ADDEND=273.15, UNITS='K'/
&DEVC ID='T_db153_R50_Z020', PROP_ID='T_db153_R50_Z020 props',
QUANTITY='THERMOCOUPLE', XYZ=0.5,0.0,0.21, CONVERSION_ADDEND=273.15, UNITS='K'/
&DEVC ID='T_db153_R50_Z030', PROP_ID='T_db153_R50_Z030 props',
QUANTITY='THERMOCOUPLE', XYZ=0.5,0.0,0.31, CONVERSION_ADDEND=273.15, UNITS='K'/
&DEVC ID='T_db153_R50_Z040', PROP_ID='T_db153_R50_Z040 props',
QUANTITY='THERMOCOUPLE', XYZ=0.5,0.0,0.41, CONVERSION_ADDEND=273.15, UNITS='K'/
&DEVC ID='T_db153_R50_Z050', PROP_ID='T_db153_R50_Z050 props',
QUANTITY='THERMOCOUPLE', XYZ=0.5,0.0,0.51, CONVERSION_ADDEND=273.15, UNITS='K'/
&DEVC ID='T_db153_R50_Z060', PROP_ID='T_db153_R50_Z060 props',
QUANTITY='THERMOCOUPLE', XYZ=0.5,0.0,0.61, CONVERSION_ADDEND=273.15, UNITS='K'/
&DEVC ID='T_db153_R50_Z070', PROP_ID='T_db153_R50_Z070 props',
QUANTITY='THERMOCOUPLE', XYZ=0.5,0.0,0.71, CONVERSION_ADDEND=273.15, UNITS='K'/
&DEVC ID='T_db153_R50_Z080', PROP_ID='T_db153_R50_Z080 props',
QUANTITY='THERMOCOUPLE', XYZ=0.5,0.0,0.81, CONVERSION_ADDEND=273.15, UNITS='K'/
&DEVC ID='T_db153_R50_Z090', PROP_ID='T_db153_R50_Z090 props',
QUANTITY='THERMOCOUPLE', XYZ=0.5,0.0,0.91, CONVERSION_ADDEND=273.15, UNITS='K'/
&DEVC ID='T_db153_R50_Z100', PROP_ID='T_db153_R50_Z100 props',
QUANTITY='THERMOCOUPLE', XYZ=0.5,0.0,1.01, CONVERSION_ADDEND=273.15, UNITS='K'/
&DEVC ID='T_db153_R50_Z110', PROP_ID='T_db153_R50_Z110 props',
QUANTITY='THERMOCOUPLE', XYZ=0.5,0.0,1.11, CONVERSION_ADDEND=273.15, UNITS='K'/
&DEVC ID='T_db153_R50_Z120', PROP_ID='T_db153_R50_Z120 props',
QUANTITY='THERMOCOUPLE', XYZ=0.5,0.0,1.21, CONVERSION_ADDEND=273.15, UNITS='K'/
&DEVC ID='T_db153_R50_Z130', PROP_ID='T_db153_R50_Z130 props',
QUANTITY='THERMOCOUPLE', XYZ=0.5,0.0,1.31, CONVERSION_ADDEND=273.15, UNITS='K'/
&DEVC ID='T_db153_R50_Z140', PROP_ID='T_db153_R50_Z140 props',
QUANTITY='THERMOCOUPLE', XYZ=0.5,0.0,1.41, CONVERSION_ADDEND=273.15, UNITS='K'/
&DEVC ID='T_db153_R50_Z150', PROP_ID='T_db153_R50_Z150 props',
QUANTITY='THERMOCOUPLE', XYZ=0.5,0.0,1.51, CONVERSION_ADDEND=273.15, UNITS='K'/
&DEVC ID='T_db153_R50_Z160', PROP_ID='T_db153_R50_Z160 props',
QUANTITY='THERMOCOUPLE', XYZ=0.5,0.0,1.61, CONVERSION_ADDEND=273.15, UNITS='K'/
&DEVC ID='T_db153_R50_Z170', PROP_ID='T_db153_R50_Z170 props',
QUANTITY='THERMOCOUPLE', XYZ=0.5,0.0,1.71, CONVERSION_ADDEND=273.15, UNITS='K'/
&DEVC ID='T_db153_R50_Z180', PROP_ID='T_db153_R50_Z180 props',
QUANTITY='THERMOCOUPLE', XYZ=0.5,0.0,1.81, CONVERSION_ADDEND=273.15, UNITS='K'/
&DEVC ID='T_db153_R50_Z190', PROP_ID='T_db153_R50_Z190 props',
QUANTITY='THERMOCOUPLE', XYZ=0.5,0.0,1.91, CONVERSION_ADDEND=273.15, UNITS='K'/
&DEVC ID='T_db153_R50_Z200', PROP_ID='T_db153_R50_Z200 props',
QUANTITY='THERMOCOUPLE', XYZ=0.5,0.0,2.01, CONVERSION_ADDEND=273.15, UNITS='K'/
&DEVC ID='T_db153_R50_Z210', PROP_ID='T_db153_R50_Z210 props',
QUANTITY='THERMOCOUPLE', XYZ=0.5,0.0,2.11, CONVERSION_ADDEND=273.15, UNITS='K'/

&DEVC ID='T_gas_R00_Z001', QUANTITY='TEMPERATURE', XYZ=0.0,0.0,0.02,
CONVERSION_ADDEND=273.15, UNITS='K'/
&DEVC ID='T_gas_R00_Z005', QUANTITY='TEMPERATURE', XYZ=0.0,0.0,0.06,
CONVERSION_ADDEND=273.15, UNITS='K'/
&DEVC ID='T_gas_R00_Z010', QUANTITY='TEMPERATURE', XYZ=0.0,0.0,0.11,

CONVERSION_ADDEND=273.15, UNITS='K'/
&DEVC ID='T_gas_R00_Z020', QUANTITY='TEMPERATURE', XYZ=0.0,0.0,0.21,
CONVERSION_ADDEND=273.15, UNITS='K'/
&DEVC ID='T_gas_R00_Z030', QUANTITY='TEMPERATURE', XYZ=0.0,0.0,0.31,
CONVERSION_ADDEND=273.15, UNITS='K'/
&DEVC ID='T_gas_R00_Z040', QUANTITY='TEMPERATURE', XYZ=0.0,0.0,0.41,
CONVERSION_ADDEND=273.15, UNITS='K'/
&DEVC ID='T_gas_R00_Z050', QUANTITY='TEMPERATURE', XYZ=0.0,0.0,0.51,
CONVERSION_ADDEND=273.15, UNITS='K'/
&DEVC ID='T_gas_R00_Z060', QUANTITY='TEMPERATURE', XYZ=0.0,0.0,0.61,
CONVERSION_ADDEND=273.15, UNITS='K'/
&DEVC ID='T_gas_R00_Z070', QUANTITY='TEMPERATURE', XYZ=0.0,0.0,0.71,
CONVERSION_ADDEND=273.15, UNITS='K'/
&DEVC ID='T_gas_R00_Z080', QUANTITY='TEMPERATURE', XYZ=0.0,0.0,0.81,
CONVERSION_ADDEND=273.15, UNITS='K'/
&DEVC ID='T_gas_R00_Z090', QUANTITY='TEMPERATURE', XYZ=0.0,0.0,0.91,
CONVERSION_ADDEND=273.15, UNITS='K'/
&DEVC ID='T_gas_R00_Z100', QUANTITY='TEMPERATURE', XYZ=0.0,0.0,1.01,
CONVERSION_ADDEND=273.15, UNITS='K'/
&DEVC ID='T_gas_R00_Z110', QUANTITY='TEMPERATURE', XYZ=0.0,0.0,1.11,
CONVERSION_ADDEND=273.15, UNITS='K'/
&DEVC ID='T_gas_R00_Z120', QUANTITY='TEMPERATURE', XYZ=0.0,0.0,1.21,
CONVERSION_ADDEND=273.15, UNITS='K'/
&DEVC ID='T_gas_R00_Z130', QUANTITY='TEMPERATURE', XYZ=0.0,0.0,1.31,
CONVERSION_ADDEND=273.15, UNITS='K'/
&DEVC ID='T_gas_R00_Z140', QUANTITY='TEMPERATURE', XYZ=0.0,0.0,1.41,
CONVERSION_ADDEND=273.15, UNITS='K'/
&DEVC ID='T_gas_R00_Z150', QUANTITY='TEMPERATURE', XYZ=0.0,0.0,1.51,
CONVERSION_ADDEND=273.15, UNITS='K'/
&DEVC ID='T_gas_R00_Z160', QUANTITY='TEMPERATURE', XYZ=0.0,0.0,1.61,
CONVERSION_ADDEND=273.15, UNITS='K'/
&DEVC ID='T_gas_R00_Z170', QUANTITY='TEMPERATURE', XYZ=0.0,0.0,1.71,
CONVERSION_ADDEND=273.15, UNITS='K'/
&DEVC ID='T_gas_R00_Z180', QUANTITY='TEMPERATURE', XYZ=0.0,0.0,1.81,
CONVERSION_ADDEND=273.15, UNITS='K'/
&DEVC ID='T_gas_R00_Z190', QUANTITY='TEMPERATURE', XYZ=0.0,0.0,1.91,
CONVERSION_ADDEND=273.15, UNITS='K'/
&DEVC ID='T_gas_R00_Z200', QUANTITY='TEMPERATURE', XYZ=0.0,0.0,2.01,
CONVERSION_ADDEND=273.15, UNITS='K'/
&DEVC ID='T_gas_R00_Z210', QUANTITY='TEMPERATURE', XYZ=0.0,0.0,2.11,
CONVERSION_ADDEND=273.15, UNITS='K'/
&DEVC ID='T_gas_R10_Z001', QUANTITY='TEMPERATURE', XYZ=0.1,0.0,0.02,
CONVERSION_ADDEND=273.15, UNITS='K'/
&DEVC ID='T_gas_R10_Z005', QUANTITY='TEMPERATURE', XYZ=0.1,0.0,0.06,
CONVERSION_ADDEND=273.15, UNITS='K'/
&DEVC ID='T_gas_R10_Z010', QUANTITY='TEMPERATURE', XYZ=0.1,0.0,0.11,

CONVERSION_ADDEND=273.15, UNITS='K'/
&DEVC ID='T_gas_R10_Z020', QUANTITY='TEMPERATURE', XYZ=0.1,0.0,0.21,
CONVERSION_ADDEND=273.15, UNITS='K'/
&DEVC ID='T_gas_R10_Z030', QUANTITY='TEMPERATURE', XYZ=0.1,0.0,0.31,
CONVERSION_ADDEND=273.15, UNITS='K'/
&DEVC ID='T_gas_R10_Z040', QUANTITY='TEMPERATURE', XYZ=0.1,0.0,0.41,
CONVERSION_ADDEND=273.15, UNITS='K'/
&DEVC ID='T_gas_R10_Z050', QUANTITY='TEMPERATURE', XYZ=0.1,0.0,0.51,
CONVERSION_ADDEND=273.15, UNITS='K'/
&DEVC ID='T_gas_R10_Z060', QUANTITY='TEMPERATURE', XYZ=0.1,0.0,0.61,
CONVERSION_ADDEND=273.15, UNITS='K'/
&DEVC ID='T_gas_R10_Z070', QUANTITY='TEMPERATURE', XYZ=0.1,0.0,0.71,
CONVERSION_ADDEND=273.15, UNITS='K'/
&DEVC ID='T_gas_R10_Z080', QUANTITY='TEMPERATURE', XYZ=0.1,0.0,0.81,
CONVERSION_ADDEND=273.15, UNITS='K'/
&DEVC ID='T_gas_R10_Z090', QUANTITY='TEMPERATURE', XYZ=0.1,0.0,0.91,
CONVERSION_ADDEND=273.15, UNITS='K'/
&DEVC ID='T_gas_R10_Z100', QUANTITY='TEMPERATURE', XYZ=0.1,0.0,1.01,
CONVERSION_ADDEND=273.15, UNITS='K'/
&DEVC ID='T_gas_R10_Z110', QUANTITY='TEMPERATURE', XYZ=0.1,0.0,1.11,
CONVERSION_ADDEND=273.15, UNITS='K'/
&DEVC ID='T_gas_R10_Z120', QUANTITY='TEMPERATURE', XYZ=0.1,0.0,1.21,
CONVERSION_ADDEND=273.15, UNITS='K'/
&DEVC ID='T_gas_R10_Z130', QUANTITY='TEMPERATURE', XYZ=0.1,0.0,1.31,
CONVERSION_ADDEND=273.15, UNITS='K'/
&DEVC ID='T_gas_R10_Z140', QUANTITY='TEMPERATURE', XYZ=0.1,0.0,1.41,
CONVERSION_ADDEND=273.15, UNITS='K'/
&DEVC ID='T_gas_R10_Z150', QUANTITY='TEMPERATURE', XYZ=0.1,0.0,1.51,
CONVERSION_ADDEND=273.15, UNITS='K'/
&DEVC ID='T_gas_R10_Z160', QUANTITY='TEMPERATURE', XYZ=0.1,0.0,1.61,
CONVERSION_ADDEND=273.15, UNITS='K'/
&DEVC ID='T_gas_R10_Z170', QUANTITY='TEMPERATURE', XYZ=0.1,0.0,1.71,
CONVERSION_ADDEND=273.15, UNITS='K'/
&DEVC ID='T_gas_R10_Z180', QUANTITY='TEMPERATURE', XYZ=0.1,0.0,1.81,
CONVERSION_ADDEND=273.15, UNITS='K'/
&DEVC ID='T_gas_R10_Z190', QUANTITY='TEMPERATURE', XYZ=0.1,0.0,1.91,
CONVERSION_ADDEND=273.15, UNITS='K'/
&DEVC ID='T_gas_R10_Z200', QUANTITY='TEMPERATURE', XYZ=0.1,0.0,2.01,
CONVERSION_ADDEND=273.15, UNITS='K'/
&DEVC ID='T_gas_R10_Z210', QUANTITY='TEMPERATURE', XYZ=0.1,0.0,2.11,
CONVERSION_ADDEND=273.15, UNITS='K'/
&DEVC ID='T_gas_R20_Z001', QUANTITY='TEMPERATURE', XYZ=0.2,0.0,0.02,
CONVERSION_ADDEND=273.15, UNITS='K'/
&DEVC ID='T_gas_R20_Z005', QUANTITY='TEMPERATURE', XYZ=0.2,0.0,0.06,
CONVERSION_ADDEND=273.15, UNITS='K'/
&DEVC ID='T_gas_R20_Z010', QUANTITY='TEMPERATURE', XYZ=0.2,0.0,0.11,

CONVERSION_ADDEND=273.15, UNITS='K'/
&DEVC ID='T_gas_R20_Z020', QUANTITY='TEMPERATURE', XYZ=0.2,0.0,0.21,
CONVERSION_ADDEND=273.15, UNITS='K'/
&DEVC ID='T_gas_R20_Z030', QUANTITY='TEMPERATURE', XYZ=0.2,0.0,0.31,
CONVERSION_ADDEND=273.15, UNITS='K'/
&DEVC ID='T_gas_R20_Z040', QUANTITY='TEMPERATURE', XYZ=0.2,0.0,0.41,
CONVERSION_ADDEND=273.15, UNITS='K'/
&DEVC ID='T_gas_R20_Z050', QUANTITY='TEMPERATURE', XYZ=0.2,0.0,0.51,
CONVERSION_ADDEND=273.15, UNITS='K'/
&DEVC ID='T_gas_R20_Z060', QUANTITY='TEMPERATURE', XYZ=0.2,0.0,0.61,
CONVERSION_ADDEND=273.15, UNITS='K'/
&DEVC ID='T_gas_R20_Z070', QUANTITY='TEMPERATURE', XYZ=0.2,0.0,0.71,
CONVERSION_ADDEND=273.15, UNITS='K'/
&DEVC ID='T_gas_R20_Z080', QUANTITY='TEMPERATURE', XYZ=0.2,0.0,0.81,
CONVERSION_ADDEND=273.15, UNITS='K'/
&DEVC ID='T_gas_R20_Z090', QUANTITY='TEMPERATURE', XYZ=0.2,0.0,0.91,
CONVERSION_ADDEND=273.15, UNITS='K'/
&DEVC ID='T_gas_R20_Z100', QUANTITY='TEMPERATURE', XYZ=0.2,0.0,1.01,
CONVERSION_ADDEND=273.15, UNITS='K'/
&DEVC ID='T_gas_R20_Z110', QUANTITY='TEMPERATURE', XYZ=0.2,0.0,1.11,
CONVERSION_ADDEND=273.15, UNITS='K'/
&DEVC ID='T_gas_R20_Z120', QUANTITY='TEMPERATURE', XYZ=0.2,0.0,1.21,
CONVERSION_ADDEND=273.15, UNITS='K'/
&DEVC ID='T_gas_R20_Z130', QUANTITY='TEMPERATURE', XYZ=0.2,0.0,1.31,
CONVERSION_ADDEND=273.15, UNITS='K'/
&DEVC ID='T_gas_R20_Z140', QUANTITY='TEMPERATURE', XYZ=0.2,0.0,1.41,
CONVERSION_ADDEND=273.15, UNITS='K'/
&DEVC ID='T_gas_R20_Z150', QUANTITY='TEMPERATURE', XYZ=0.2,0.0,1.51,
CONVERSION_ADDEND=273.15, UNITS='K'/
&DEVC ID='T_gas_R20_Z160', QUANTITY='TEMPERATURE', XYZ=0.2,0.0,1.61,
CONVERSION_ADDEND=273.15, UNITS='K'/
&DEVC ID='T_gas_R20_Z170', QUANTITY='TEMPERATURE', XYZ=0.2,0.0,1.71,
CONVERSION_ADDEND=273.15, UNITS='K'/
&DEVC ID='T_gas_R20_Z180', QUANTITY='TEMPERATURE', XYZ=0.2,0.0,1.81,
CONVERSION_ADDEND=273.15, UNITS='K'/
&DEVC ID='T_gas_R20_Z190', QUANTITY='TEMPERATURE', XYZ=0.2,0.0,1.91,
CONVERSION_ADDEND=273.15, UNITS='K'/
&DEVC ID='T_gas_R20_Z200', QUANTITY='TEMPERATURE', XYZ=0.2,0.0,2.01,
CONVERSION_ADDEND=273.15, UNITS='K'/
&DEVC ID='T_gas_R20_Z210', QUANTITY='TEMPERATURE', XYZ=0.2,0.0,2.11,
CONVERSION_ADDEND=273.15, UNITS='K'/
&DEVC ID='T_gas_R30_Z001', QUANTITY='TEMPERATURE', XYZ=0.3,0.0,0.02,
CONVERSION_ADDEND=273.15, UNITS='K'/
&DEVC ID='T_gas_R30_Z005', QUANTITY='TEMPERATURE', XYZ=0.3,0.0,0.06,
CONVERSION_ADDEND=273.15, UNITS='K'/
&DEVC ID='T_gas_R30_Z010', QUANTITY='TEMPERATURE', XYZ=0.3,0.0,0.11,

CONVERSION_ADDEND=273.15, UNITS='K'/
&DEVC ID='T_gas_R30_Z020', QUANTITY='TEMPERATURE', XYZ=0.3,0.0,0.21,
CONVERSION_ADDEND=273.15, UNITS='K'/
&DEVC ID='T_gas_R30_Z030', QUANTITY='TEMPERATURE', XYZ=0.3,0.0,0.31,
CONVERSION_ADDEND=273.15, UNITS='K'/
&DEVC ID='T_gas_R30_Z040', QUANTITY='TEMPERATURE', XYZ=0.3,0.0,0.41,
CONVERSION_ADDEND=273.15, UNITS='K'/
&DEVC ID='T_gas_R30_Z050', QUANTITY='TEMPERATURE', XYZ=0.3,0.0,0.51,
CONVERSION_ADDEND=273.15, UNITS='K'/
&DEVC ID='T_gas_R30_Z060', QUANTITY='TEMPERATURE', XYZ=0.3,0.0,0.61,
CONVERSION_ADDEND=273.15, UNITS='K'/
&DEVC ID='T_gas_R30_Z070', QUANTITY='TEMPERATURE', XYZ=0.3,0.0,0.71,
CONVERSION_ADDEND=273.15, UNITS='K'/
&DEVC ID='T_gas_R30_Z080', QUANTITY='TEMPERATURE', XYZ=0.3,0.0,0.81,
CONVERSION_ADDEND=273.15, UNITS='K'/
&DEVC ID='T_gas_R30_Z090', QUANTITY='TEMPERATURE', XYZ=0.3,0.0,0.91,
CONVERSION_ADDEND=273.15, UNITS='K'/
&DEVC ID='T_gas_R30_Z100', QUANTITY='TEMPERATURE', XYZ=0.3,0.0,1.01,
CONVERSION_ADDEND=273.15, UNITS='K'/
&DEVC ID='T_gas_R30_Z110', QUANTITY='TEMPERATURE', XYZ=0.3,0.0,1.11,
CONVERSION_ADDEND=273.15, UNITS='K'/
&DEVC ID='T_gas_R30_Z120', QUANTITY='TEMPERATURE', XYZ=0.3,0.0,1.21,
CONVERSION_ADDEND=273.15, UNITS='K'/
&DEVC ID='T_gas_R30_Z130', QUANTITY='TEMPERATURE', XYZ=0.3,0.0,1.31,
CONVERSION_ADDEND=273.15, UNITS='K'/
&DEVC ID='T_gas_R30_Z140', QUANTITY='TEMPERATURE', XYZ=0.3,0.0,1.41,
CONVERSION_ADDEND=273.15, UNITS='K'/
&DEVC ID='T_gas_R30_Z150', QUANTITY='TEMPERATURE', XYZ=0.3,0.0,1.51,
CONVERSION_ADDEND=273.15, UNITS='K'/
&DEVC ID='T_gas_R30_Z160', QUANTITY='TEMPERATURE', XYZ=0.3,0.0,1.61,
CONVERSION_ADDEND=273.15, UNITS='K'/
&DEVC ID='T_gas_R30_Z170', QUANTITY='TEMPERATURE', XYZ=0.3,0.0,1.71,
CONVERSION_ADDEND=273.15, UNITS='K'/
&DEVC ID='T_gas_R30_Z180', QUANTITY='TEMPERATURE', XYZ=0.3,0.0,1.81,
CONVERSION_ADDEND=273.15, UNITS='K'/
&DEVC ID='T_gas_R30_Z190', QUANTITY='TEMPERATURE', XYZ=0.3,0.0,1.91,
CONVERSION_ADDEND=273.15, UNITS='K'/
&DEVC ID='T_gas_R30_Z200', QUANTITY='TEMPERATURE', XYZ=0.3,0.0,2.01,
CONVERSION_ADDEND=273.15, UNITS='K'/
&DEVC ID='T_gas_R30_Z210', QUANTITY='TEMPERATURE', XYZ=0.3,0.0,2.11,
CONVERSION_ADDEND=273.15, UNITS='K'/
&DEVC ID='T_gas_R40_Z001', QUANTITY='TEMPERATURE', XYZ=0.4,0.0,0.02,
CONVERSION_ADDEND=273.15, UNITS='K'/
&DEVC ID='T_gas_R40_Z005', QUANTITY='TEMPERATURE', XYZ=0.4,0.0,0.06,
CONVERSION_ADDEND=273.15, UNITS='K'/
&DEVC ID='T_gas_R40_Z010', QUANTITY='TEMPERATURE', XYZ=0.4,0.0,0.11,

CONVERSION_ADDEND=273.15, UNITS='K'/
&DEVC ID='T_gas_R40_Z020', QUANTITY='TEMPERATURE', XYZ=0.4,0.0,0.21,
CONVERSION_ADDEND=273.15, UNITS='K'/
&DEVC ID='T_gas_R40_Z030', QUANTITY='TEMPERATURE', XYZ=0.4,0.0,0.31,
CONVERSION_ADDEND=273.15, UNITS='K'/
&DEVC ID='T_gas_R40_Z040', QUANTITY='TEMPERATURE', XYZ=0.4,0.0,0.41,
CONVERSION_ADDEND=273.15, UNITS='K'/
&DEVC ID='T_gas_R40_Z050', QUANTITY='TEMPERATURE', XYZ=0.4,0.0,0.51,
CONVERSION_ADDEND=273.15, UNITS='K'/
&DEVC ID='T_gas_R40_Z060', QUANTITY='TEMPERATURE', XYZ=0.4,0.0,0.61,
CONVERSION_ADDEND=273.15, UNITS='K'/
&DEVC ID='T_gas_R40_Z070', QUANTITY='TEMPERATURE', XYZ=0.4,0.0,0.71,
CONVERSION_ADDEND=273.15, UNITS='K'/
&DEVC ID='T_gas_R40_Z080', QUANTITY='TEMPERATURE', XYZ=0.4,0.0,0.81,
CONVERSION_ADDEND=273.15, UNITS='K'/
&DEVC ID='T_gas_R40_Z090', QUANTITY='TEMPERATURE', XYZ=0.4,0.0,0.91,
CONVERSION_ADDEND=273.15, UNITS='K'/
&DEVC ID='T_gas_R40_Z100', QUANTITY='TEMPERATURE', XYZ=0.4,0.0,1.01,
CONVERSION_ADDEND=273.15, UNITS='K'/
&DEVC ID='T_gas_R40_Z110', QUANTITY='TEMPERATURE', XYZ=0.4,0.0,1.11,
CONVERSION_ADDEND=273.15, UNITS='K'/
&DEVC ID='T_gas_R40_Z120', QUANTITY='TEMPERATURE', XYZ=0.4,0.0,1.21,
CONVERSION_ADDEND=273.15, UNITS='K'/
&DEVC ID='T_gas_R40_Z130', QUANTITY='TEMPERATURE', XYZ=0.4,0.0,1.31,
CONVERSION_ADDEND=273.15, UNITS='K'/
&DEVC ID='T_gas_R40_Z140', QUANTITY='TEMPERATURE', XYZ=0.4,0.0,1.41,
CONVERSION_ADDEND=273.15, UNITS='K'/
&DEVC ID='T_gas_R40_Z150', QUANTITY='TEMPERATURE', XYZ=0.4,0.0,1.51,
CONVERSION_ADDEND=273.15, UNITS='K'/
&DEVC ID='T_gas_R40_Z160', QUANTITY='TEMPERATURE', XYZ=0.4,0.0,1.61,
CONVERSION_ADDEND=273.15, UNITS='K'/
&DEVC ID='T_gas_R40_Z170', QUANTITY='TEMPERATURE', XYZ=0.4,0.0,1.71,
CONVERSION_ADDEND=273.15, UNITS='K'/
&DEVC ID='T_gas_R40_Z180', QUANTITY='TEMPERATURE', XYZ=0.4,0.0,1.81,
CONVERSION_ADDEND=273.15, UNITS='K'/
&DEVC ID='T_gas_R40_Z190', QUANTITY='TEMPERATURE', XYZ=0.4,0.0,1.91,
CONVERSION_ADDEND=273.15, UNITS='K'/
&DEVC ID='T_gas_R40_Z200', QUANTITY='TEMPERATURE', XYZ=0.4,0.0,2.01,
CONVERSION_ADDEND=273.15, UNITS='K'/
&DEVC ID='T_gas_R40_Z210', QUANTITY='TEMPERATURE', XYZ=0.4,0.0,2.11,
CONVERSION_ADDEND=273.15, UNITS='K'/
&DEVC ID='T_gas_R50_Z001', QUANTITY='TEMPERATURE', XYZ=0.5,0.0,0.02,
CONVERSION_ADDEND=273.15, UNITS='K'/
&DEVC ID='T_gas_R50_Z005', QUANTITY='TEMPERATURE', XYZ=0.5,0.0,0.06,
CONVERSION_ADDEND=273.15, UNITS='K'/
&DEVC ID='T_gas_R50_Z010', QUANTITY='TEMPERATURE', XYZ=0.5,0.0,0.11,

CONVERSION_ADDEND=273.15, UNITS='K'/
&DEVC ID='T_gas_R50_Z020', QUANTITY='TEMPERATURE', XYZ=0.5,0.0,0.21,
CONVERSION_ADDEND=273.15, UNITS='K'/
&DEVC ID='T_gas_R50_Z030', QUANTITY='TEMPERATURE', XYZ=0.5,0.0,0.31,
CONVERSION_ADDEND=273.15, UNITS='K'/
&DEVC ID='T_gas_R50_Z040', QUANTITY='TEMPERATURE', XYZ=0.5,0.0,0.41,
CONVERSION_ADDEND=273.15, UNITS='K'/
&DEVC ID='T_gas_R50_Z050', QUANTITY='TEMPERATURE', XYZ=0.5,0.0,0.51,
CONVERSION_ADDEND=273.15, UNITS='K'/
&DEVC ID='T_gas_R50_Z060', QUANTITY='TEMPERATURE', XYZ=0.5,0.0,0.61,
CONVERSION_ADDEND=273.15, UNITS='K'/
&DEVC ID='T_gas_R50_Z070', QUANTITY='TEMPERATURE', XYZ=0.5,0.0,0.71,
CONVERSION_ADDEND=273.15, UNITS='K'/
&DEVC ID='T_gas_R50_Z080', QUANTITY='TEMPERATURE', XYZ=0.5,0.0,0.81,
CONVERSION_ADDEND=273.15, UNITS='K'/
&DEVC ID='T_gas_R50_Z090', QUANTITY='TEMPERATURE', XYZ=0.5,0.0,0.91,
CONVERSION_ADDEND=273.15, UNITS='K'/
&DEVC ID='T_gas_R50_Z100', QUANTITY='TEMPERATURE', XYZ=0.5,0.0,1.01,
CONVERSION_ADDEND=273.15, UNITS='K'/
&DEVC ID='T_gas_R50_Z110', QUANTITY='TEMPERATURE', XYZ=0.5,0.0,1.11,
CONVERSION_ADDEND=273.15, UNITS='K'/
&DEVC ID='T_gas_R50_Z120', QUANTITY='TEMPERATURE', XYZ=0.5,0.0,1.21,
CONVERSION_ADDEND=273.15, UNITS='K'/
&DEVC ID='T_gas_R50_Z130', QUANTITY='TEMPERATURE', XYZ=0.5,0.0,1.31,
CONVERSION_ADDEND=273.15, UNITS='K'/
&DEVC ID='T_gas_R50_Z140', QUANTITY='TEMPERATURE', XYZ=0.5,0.0,1.41,
CONVERSION_ADDEND=273.15, UNITS='K'/
&DEVC ID='T_gas_R50_Z150', QUANTITY='TEMPERATURE', XYZ=0.5,0.0,1.51,
CONVERSION_ADDEND=273.15, UNITS='K'/
&DEVC ID='T_gas_R50_Z160', QUANTITY='TEMPERATURE', XYZ=0.5,0.0,1.61,
CONVERSION_ADDEND=273.15, UNITS='K'/
&DEVC ID='T_gas_R50_Z170', QUANTITY='TEMPERATURE', XYZ=0.5,0.0,1.71,
CONVERSION_ADDEND=273.15, UNITS='K'/
&DEVC ID='T_gas_R50_Z180', QUANTITY='TEMPERATURE', XYZ=0.5,0.0,1.81,
CONVERSION_ADDEND=273.15, UNITS='K'/
&DEVC ID='T_gas_R50_Z190', QUANTITY='TEMPERATURE', XYZ=0.5,0.0,1.91,
CONVERSION_ADDEND=273.15, UNITS='K'/
&DEVC ID='T_gas_R50_Z200', QUANTITY='TEMPERATURE', XYZ=0.5,0.0,2.01,
CONVERSION_ADDEND=273.15, UNITS='K'/
&DEVC ID='T_gas_R50_Z210', QUANTITY='TEMPERATURE', XYZ=0.5,0.0,2.11,
CONVERSION_ADDEND=273.15, UNITS='K'/

&DEVC ID='V_R00_Z001', QUANTITY='VELOCITY', XYZ=0,0.0,0.02/
&DEVC ID='V_R00_Z005', QUANTITY='VELOCITY', XYZ=0,0.0,0.06/
&DEVC ID='V_R00_Z010', QUANTITY='VELOCITY', XYZ=0,0.0,0.11/
&DEVC ID='V_R00_Z020', QUANTITY='VELOCITY', XYZ=0,0.0,0.21/
&DEVC ID='V_R00_Z030', QUANTITY='VELOCITY', XYZ=0,0.0,0.31/

&DEVC ID='V_R00_Z040', QUANTITY='VELOCITY', XYZ=0,0.0,0.41/
&DEVC ID='V_R00_Z050', QUANTITY='VELOCITY', XYZ=0,0.0,0.51/
&DEVC ID='V_R00_Z060', QUANTITY='VELOCITY', XYZ=0,0.0,0.61/
&DEVC ID='V_R00_Z070', QUANTITY='VELOCITY', XYZ=0,0.0,0.71/
&DEVC ID='V_R00_Z080', QUANTITY='VELOCITY', XYZ=0,0.0,0.81/
&DEVC ID='V_R00_Z090', QUANTITY='VELOCITY', XYZ=0,0.0,0.91/
&DEVC ID='V_R00_Z100', QUANTITY='VELOCITY', XYZ=0,0.0,1.01/
&DEVC ID='V_R00_Z110', QUANTITY='VELOCITY', XYZ=0,0.0,1.11/
&DEVC ID='V_R00_Z120', QUANTITY='VELOCITY', XYZ=0,0.0,1.21/
&DEVC ID='V_R00_Z130', QUANTITY='VELOCITY', XYZ=0,0.0,1.31/
&DEVC ID='V_R00_Z140', QUANTITY='VELOCITY', XYZ=0,0.0,1.41/
&DEVC ID='V_R00_Z150', QUANTITY='VELOCITY', XYZ=0,0.0,1.51/
&DEVC ID='V_R00_Z160', QUANTITY='VELOCITY', XYZ=0,0.0,1.61/
&DEVC ID='V_R00_Z170', QUANTITY='VELOCITY', XYZ=0,0.0,1.71/
&DEVC ID='V_R00_Z180', QUANTITY='VELOCITY', XYZ=0,0.0,1.81/
&DEVC ID='V_R00_Z190', QUANTITY='VELOCITY', XYZ=0,0.0,1.91/
&DEVC ID='V_R00_Z200', QUANTITY='VELOCITY', XYZ=0,0.0,2.01/
&DEVC ID='V_R00_Z210', QUANTITY='VELOCITY', XYZ=0,0.0,2.11/
&DEVC ID='V_R10_Z001', QUANTITY='VELOCITY', XYZ=0.1,0.0,0.02/
&DEVC ID='V_R10_Z005', QUANTITY='VELOCITY', XYZ=0.1,0.0,0.06/
&DEVC ID='V_R10_Z010', QUANTITY='VELOCITY', XYZ=0.1,0.0,0.11/
&DEVC ID='V_R10_Z020', QUANTITY='VELOCITY', XYZ=0.1,0.0,0.21/
&DEVC ID='V_R10_Z030', QUANTITY='VELOCITY', XYZ=0.1,0.0,0.31/
&DEVC ID='V_R10_Z040', QUANTITY='VELOCITY', XYZ=0.1,0.0,0.41/
&DEVC ID='V_R10_Z050', QUANTITY='VELOCITY', XYZ=0.1,0.0,0.51/
&DEVC ID='V_R10_Z060', QUANTITY='VELOCITY', XYZ=0.1,0.0,0.61/
&DEVC ID='V_R10_Z070', QUANTITY='VELOCITY', XYZ=0.1,0.0,0.71/
&DEVC ID='V_R10_Z080', QUANTITY='VELOCITY', XYZ=0.1,0.0,0.81/
&DEVC ID='V_R10_Z090', QUANTITY='VELOCITY', XYZ=0.1,0.0,0.91/
&DEVC ID='V_R10_Z100', QUANTITY='VELOCITY', XYZ=0.1,0.0,1.01/
&DEVC ID='V_R10_Z110', QUANTITY='VELOCITY', XYZ=0.1,0.0,1.11/
&DEVC ID='V_R10_Z120', QUANTITY='VELOCITY', XYZ=0.1,0.0,1.21/
&DEVC ID='V_R10_Z130', QUANTITY='VELOCITY', XYZ=0.1,0.0,1.31/
&DEVC ID='V_R10_Z140', QUANTITY='VELOCITY', XYZ=0.1,0.0,1.41/
&DEVC ID='V_R10_Z150', QUANTITY='VELOCITY', XYZ=0.1,0.0,1.51/
&DEVC ID='V_R10_Z160', QUANTITY='VELOCITY', XYZ=0.1,0.0,1.61/
&DEVC ID='V_R10_Z170', QUANTITY='VELOCITY', XYZ=0.1,0.0,1.71/
&DEVC ID='V_R10_Z180', QUANTITY='VELOCITY', XYZ=0.1,0.0,1.81/
&DEVC ID='V_R10_Z190', QUANTITY='VELOCITY', XYZ=0.1,0.0,1.91/
&DEVC ID='V_R10_Z200', QUANTITY='VELOCITY', XYZ=0.1,0.0,2.01/
&DEVC ID='V_R10_Z210', QUANTITY='VELOCITY', XYZ=0.1,0.0,2.11/
&DEVC ID='V_R20_Z001', QUANTITY='VELOCITY', XYZ=0.2,0.0,0.02/
&DEVC ID='V_R20_Z005', QUANTITY='VELOCITY', XYZ=0.2,0.0,0.06/
&DEVC ID='V_R20_Z010', QUANTITY='VELOCITY', XYZ=0.2,0.0,0.11/
&DEVC ID='V_R20_Z020', QUANTITY='VELOCITY', XYZ=0.2,0.0,0.21/
&DEVC ID='V_R20_Z030', QUANTITY='VELOCITY', XYZ=0.2,0.0,0.31/

&DEVC ID='V_R20_Z040', QUANTITY='VELOCITY', XYZ=0.2,0.0,0.41/
&DEVC ID='V_R20_Z050', QUANTITY='VELOCITY', XYZ=0.2,0.0,0.51/
&DEVC ID='V_R20_Z060', QUANTITY='VELOCITY', XYZ=0.2,0.0,0.61/
&DEVC ID='V_R20_Z070', QUANTITY='VELOCITY', XYZ=0.2,0.0,0.71/
&DEVC ID='V_R20_Z080', QUANTITY='VELOCITY', XYZ=0.2,0.0,0.81/
&DEVC ID='V_R20_Z090', QUANTITY='VELOCITY', XYZ=0.2,0.0,0.91/
&DEVC ID='V_R20_Z100', QUANTITY='VELOCITY', XYZ=0.2,0.0,1.01/
&DEVC ID='V_R20_Z110', QUANTITY='VELOCITY', XYZ=0.2,0.0,1.11/
&DEVC ID='V_R20_Z120', QUANTITY='VELOCITY', XYZ=0.2,0.0,1.21/
&DEVC ID='V_R20_Z130', QUANTITY='VELOCITY', XYZ=0.2,0.0,1.31/
&DEVC ID='V_R20_Z140', QUANTITY='VELOCITY', XYZ=0.2,0.0,1.41/
&DEVC ID='V_R20_Z150', QUANTITY='VELOCITY', XYZ=0.2,0.0,1.51/
&DEVC ID='V_R20_Z160', QUANTITY='VELOCITY', XYZ=0.2,0.0,1.61/
&DEVC ID='V_R20_Z170', QUANTITY='VELOCITY', XYZ=0.2,0.0,1.71/
&DEVC ID='V_R20_Z180', QUANTITY='VELOCITY', XYZ=0.2,0.0,1.81/
&DEVC ID='V_R20_Z190', QUANTITY='VELOCITY', XYZ=0.2,0.0,1.91/
&DEVC ID='V_R20_Z200', QUANTITY='VELOCITY', XYZ=0.2,0.0,2.01/
&DEVC ID='V_R20_Z210', QUANTITY='VELOCITY', XYZ=0.2,0.0,2.11/
&DEVC ID='V_R30_Z001', QUANTITY='VELOCITY', XYZ=0.3,0.0,0.02/
&DEVC ID='V_R30_Z005', QUANTITY='VELOCITY', XYZ=0.3,0.0,0.06/
&DEVC ID='V_R30_Z010', QUANTITY='VELOCITY', XYZ=0.3,0.0,0.11/
&DEVC ID='V_R30_Z020', QUANTITY='VELOCITY', XYZ=0.3,0.0,0.21/
&DEVC ID='V_R30_Z030', QUANTITY='VELOCITY', XYZ=0.3,0.0,0.31/
&DEVC ID='V_R30_Z040', QUANTITY='VELOCITY', XYZ=0.3,0.0,0.41/
&DEVC ID='V_R30_Z050', QUANTITY='VELOCITY', XYZ=0.3,0.0,0.51/
&DEVC ID='V_R30_Z060', QUANTITY='VELOCITY', XYZ=0.3,0.0,0.61/
&DEVC ID='V_R30_Z070', QUANTITY='VELOCITY', XYZ=0.3,0.0,0.71/
&DEVC ID='V_R30_Z080', QUANTITY='VELOCITY', XYZ=0.3,0.0,0.81/
&DEVC ID='V_R30_Z090', QUANTITY='VELOCITY', XYZ=0.3,0.0,0.91/
&DEVC ID='V_R30_Z100', QUANTITY='VELOCITY', XYZ=0.3,0.0,1.01/
&DEVC ID='V_R30_Z110', QUANTITY='VELOCITY', XYZ=0.3,0.0,1.11/
&DEVC ID='V_R30_Z120', QUANTITY='VELOCITY', XYZ=0.3,0.0,1.21/
&DEVC ID='V_R30_Z130', QUANTITY='VELOCITY', XYZ=0.3,0.0,1.31/
&DEVC ID='V_R30_Z140', QUANTITY='VELOCITY', XYZ=0.3,0.0,1.41/
&DEVC ID='V_R30_Z150', QUANTITY='VELOCITY', XYZ=0.3,0.0,1.51/
&DEVC ID='V_R30_Z160', QUANTITY='VELOCITY', XYZ=0.3,0.0,1.61/
&DEVC ID='V_R30_Z170', QUANTITY='VELOCITY', XYZ=0.3,0.0,1.71/
&DEVC ID='V_R30_Z180', QUANTITY='VELOCITY', XYZ=0.3,0.0,1.81/
&DEVC ID='V_R30_Z190', QUANTITY='VELOCITY', XYZ=0.3,0.0,1.91/
&DEVC ID='V_R30_Z200', QUANTITY='VELOCITY', XYZ=0.3,0.0,2.01/
&DEVC ID='V_R30_Z210', QUANTITY='VELOCITY', XYZ=0.3,0.0,2.11/
&DEVC ID='V_R40_Z001', QUANTITY='VELOCITY', XYZ=0.4,0.0,0.02/
&DEVC ID='V_R40_Z005', QUANTITY='VELOCITY', XYZ=0.4,0.0,0.06/
&DEVC ID='V_R40_Z010', QUANTITY='VELOCITY', XYZ=0.4,0.0,0.11/
&DEVC ID='V_R40_Z020', QUANTITY='VELOCITY', XYZ=0.4,0.0,0.21/
&DEVC ID='V_R40_Z030', QUANTITY='VELOCITY', XYZ=0.4,0.0,0.31/

&DEVC ID='V_R40_Z040', QUANTITY='VELOCITY', XYZ=0.4,0.0,0.41/
&DEVC ID='V_R40_Z050', QUANTITY='VELOCITY', XYZ=0.4,0.0,0.51/
&DEVC ID='V_R40_Z060', QUANTITY='VELOCITY', XYZ=0.4,0.0,0.61/
&DEVC ID='V_R40_Z070', QUANTITY='VELOCITY', XYZ=0.4,0.0,0.71/
&DEVC ID='V_R40_Z080', QUANTITY='VELOCITY', XYZ=0.4,0.0,0.81/
&DEVC ID='V_R40_Z090', QUANTITY='VELOCITY', XYZ=0.4,0.0,0.91/
&DEVC ID='V_R40_Z100', QUANTITY='VELOCITY', XYZ=0.4,0.0,1.01/
&DEVC ID='V_R40_Z110', QUANTITY='VELOCITY', XYZ=0.4,0.0,1.11/
&DEVC ID='V_R40_Z120', QUANTITY='VELOCITY', XYZ=0.4,0.0,1.21/
&DEVC ID='V_R40_Z130', QUANTITY='VELOCITY', XYZ=0.4,0.0,1.31/
&DEVC ID='V_R40_Z140', QUANTITY='VELOCITY', XYZ=0.4,0.0,1.41/
&DEVC ID='V_R40_Z150', QUANTITY='VELOCITY', XYZ=0.4,0.0,1.51/
&DEVC ID='V_R40_Z160', QUANTITY='VELOCITY', XYZ=0.4,0.0,1.61/
&DEVC ID='V_R40_Z170', QUANTITY='VELOCITY', XYZ=0.4,0.0,1.71/
&DEVC ID='V_R40_Z180', QUANTITY='VELOCITY', XYZ=0.4,0.0,1.81/
&DEVC ID='V_R40_Z190', QUANTITY='VELOCITY', XYZ=0.4,0.0,1.91/
&DEVC ID='V_R40_Z200', QUANTITY='VELOCITY', XYZ=0.4,0.0,2.01/
&DEVC ID='V_R40_Z210', QUANTITY='VELOCITY', XYZ=0.4,0.0,2.11/
&DEVC ID='V_R50_Z001', QUANTITY='VELOCITY', XYZ=0.5,0.0,0.02/
&DEVC ID='V_R50_Z005', QUANTITY='VELOCITY', XYZ=0.5,0.0,0.06/
&DEVC ID='V_R50_Z010', QUANTITY='VELOCITY', XYZ=0.5,0.0,0.11/
&DEVC ID='V_R50_Z020', QUANTITY='VELOCITY', XYZ=0.5,0.0,0.21/
&DEVC ID='V_R50_Z030', QUANTITY='VELOCITY', XYZ=0.5,0.0,0.31/
&DEVC ID='V_R50_Z040', QUANTITY='VELOCITY', XYZ=0.5,0.0,0.41/
&DEVC ID='V_R50_Z050', QUANTITY='VELOCITY', XYZ=0.5,0.0,0.51/
&DEVC ID='V_R50_Z060', QUANTITY='VELOCITY', XYZ=0.5,0.0,0.61/
&DEVC ID='V_R50_Z070', QUANTITY='VELOCITY', XYZ=0.5,0.0,0.71/
&DEVC ID='V_R50_Z080', QUANTITY='VELOCITY', XYZ=0.5,0.0,0.81/
&DEVC ID='V_R50_Z090', QUANTITY='VELOCITY', XYZ=0.5,0.0,0.91/
&DEVC ID='V_R50_Z100', QUANTITY='VELOCITY', XYZ=0.5,0.0,1.01/
&DEVC ID='V_R50_Z110', QUANTITY='VELOCITY', XYZ=0.5,0.0,1.11/
&DEVC ID='V_R50_Z120', QUANTITY='VELOCITY', XYZ=0.5,0.0,1.21/
&DEVC ID='V_R50_Z130', QUANTITY='VELOCITY', XYZ=0.5,0.0,1.31/
&DEVC ID='V_R50_Z140', QUANTITY='VELOCITY', XYZ=0.5,0.0,1.41/
&DEVC ID='V_R50_Z150', QUANTITY='VELOCITY', XYZ=0.5,0.0,1.51/
&DEVC ID='V_R50_Z160', QUANTITY='VELOCITY', XYZ=0.5,0.0,1.61/
&DEVC ID='V_R50_Z170', QUANTITY='VELOCITY', XYZ=0.5,0.0,1.71/
&DEVC ID='V_R50_Z180', QUANTITY='VELOCITY', XYZ=0.5,0.0,1.81/
&DEVC ID='V_R50_Z190', QUANTITY='VELOCITY', XYZ=0.5,0.0,1.91/
&DEVC ID='V_R50_Z200', QUANTITY='VELOCITY', XYZ=0.5,0.0,2.01/
&DEVC ID='V_R50_Z210', QUANTITY='VELOCITY', XYZ=0.5,0.0,2.11/

&PROP ID='TC', BEAD_DIAMETER=0.0001533 /
&DEVC XB= 0.001,0.001,0.001,0.001,0.005,2.105, QUANTITY='THERMOCOUPLE',
ID='db_153_T_CL', PROP_ID='TC', POINTS=211, CONVERSION_ADDEND=273.15, UNITS='K',
COORD_FACTOR=100., XYZ_UNITS='cm', Z_ID='z' /
&DEVC XB= 0.001,0.001,0.001,0.001,0.005,2.105, QUANTITY='THERMOCOUPLE',

ID='db_153_T_CL_RMS', PROP_ID='TC', POINTS=211, TEMPORAL_STATISTIC='RMS', UNITS='K', HIDE_COORDINATES=.TRUE. /

&DEVC XB=-0.095,0.495,0.001,0.001,0.200,0.200, QUANTITY='THERMOCOUPLE', ID='db_153_T_20', PROP_ID='TC', POINTS=60 , CONVERSION_ADDEND=273.15, UNITS='K', COORD_FACTOR=100., XYZ_UNITS='cm', X_ID='r' /
&DEVC XB=-0.095,0.495,0.001,0.001,0.200,0.200, QUANTITY='THERMOCOUPLE', ID='db_153_T_20_RMS', PROP_ID='TC', POINTS=60 , TEMPORAL_STATISTIC='RMS', UNITS='K', HIDE_COORDINATES=.TRUE. /
&DEVC XB=-0.095,0.495,0.001,0.001,0.600,0.600, QUANTITY='THERMOCOUPLE', ID='db_153_T_60', PROP_ID='TC', POINTS=60 , CONVERSION_ADDEND=273.15, UNITS='K', HIDE_COORDINATES=.TRUE. /
&DEVC XB=-0.095,0.495,0.001,0.001,0.600,0.600, QUANTITY='THERMOCOUPLE', ID='db_153_T_60_RMS', PROP_ID='TC', POINTS=60 , TEMPORAL_STATISTIC='RMS', UNITS='K', HIDE_COORDINATES=.TRUE. /
&DEVC XB=-0.095,0.495,0.001,0.001,1.000,1.000, QUANTITY='THERMOCOUPLE', ID='db_153_T_100', PROP_ID='TC', POINTS=60 , CONVERSION_ADDEND=273.15, UNITS='K', HIDE_COORDINATES=.TRUE. /
&DEVC XB=-0.095,0.495,0.001,0.001,1.000,1.000, QUANTITY='THERMOCOUPLE', ID='db_153_T_100_RMS', PROP_ID='TC', POINTS=60 , TEMPORAL_STATISTIC='RMS', UNITS='K', HIDE_COORDINATES=.TRUE. /
&DEVC XB=-0.095,0.495,0.001,0.001,1.400,1.400, QUANTITY='THERMOCOUPLE', ID='db_153_T_140', PROP_ID='TC', POINTS=60 , CONVERSION_ADDEND=273.15, UNITS='K', HIDE_COORDINATES=.TRUE. /
&DEVC XB=-0.095,0.495,0.001,0.001,1.400,1.400, QUANTITY='THERMOCOUPLE', ID='db_153_T_140_RMS', PROP_ID='TC', POINTS=60 , TEMPORAL_STATISTIC='RMS', UNITS='K', HIDE_COORDINATES=.TRUE. /
&DEVC XB=-0.095,0.495,0.001,0.001,1.800,1.800, QUANTITY='THERMOCOUPLE', ID='db_153_T_180', PROP_ID='TC', POINTS=60 , CONVERSION_ADDEND=273.15, UNITS='K', HIDE_COORDINATES=.TRUE. /
&DEVC XB=-0.095,0.495,0.001,0.001,1.800,1.800, QUANTITY='THERMOCOUPLE', ID='db_153_T_180_RMS', PROP_ID='TC', POINTS=60 , TEMPORAL_STATISTIC='RMS', UNITS='K', HIDE_COORDINATES=.TRUE. /